OUTFLOWS IN HIGH MASS STAR-FORMING REGIONS

Thesis by

Mary Anne Barsony

In Partial Fulfillment of the Requirements

for the Degree of

Doctor of Philosophy

California Institute of Technology

Pasadena, California

1989

(Submitted September 23, 1988)

DEDICATION

To the memory of my grandmother

Ella Stern Braunauer

b. August 7, 1901 Budapest, Hungary

d. February 8, 1988 San Francisco

who had the intelligence, curiosity, and tenacity it takes to be a great scientist,

but was denied the opportunity.

ACKNOWLEDGEMENTS

Pursuing the Ph.D. has proved to be at least as much a test of will and self-confidence, as of intellect. No one can complete a project such as this without strong moral and personal support. It is in this spirit that I am most grateful to my advisor, Prof. Nick Scoville, who is a member of the rare few in his position who are color and gender blind when it comes to doing science. Thank you, Nick, for being the example you are to follow. I would also like to thank you for your support in the form of the Graduate Research Assistantship, paid travel expenses to observatories and conferences, and the payment of the astronomical graphic arts, Xerox, and computer costs I have incurred.

I would like to thank Prof. Blandford for suggesting this thesis topic as a fruitful one for further investigation, Drs. Dana Backman, John Bally, Bel Campbell, Mark Claussen, Pat Crane, Geoff Marcy, Jeff Kenney, Colin Masson, Lee Mundy, Bev Oke, Anneila Sargent, James Schombert, Sue Terebey, Juan Uson, and George Wallerstein for teaching me how to use the different instruments, how to reduce the data, and how to think about the results. I am still in awe of the skills, knowledge, and wit of Helen Knudsen, the librarian of the Caltech astronomy library, who knows at a moment's notice where to locate the most arcane reference.

I would like to thank the entire graduate physics class that entered in that fateful year of 1982. Although not all of us made it through, we will all keep in touch. I will always be grateful to Donna Driscoll, our graduate physics secretary, who helped me navigate through the intricacies of interdepartmental bureaucracy. A separate thank you goes to Jim McCarthy, my officemate and fellow astronomy graduate student.

Finally, I would like to thank my friends Heidi Aspaturian, proto-Dr. Lynne Deutsch (you're almost there Lynne), Dr. Holly Eissler, proto-Dr. Erica Gellin, and Dr. Adèle Tutter for their example and encouragement.

ABSTRACT

In the last decade, observations of star-forming regions in the millimeter wavelength range have led to the discovery of supersonic molecular outflows from embedded infrared sources, a heretofore unsuspected, but now generally accepted, phase in the star formation process. In order to better understand the outflow phenomenon in high mass (*i.e.*, high luminosity) pre-main sequence stars, the three sources S87, LkHα101, and S106 were chosen for closer study. Observations from the recently completed Owens Valley Radio Observatory's millimeter wave interferometer afford us the highest spatial-resolution, molecular line (CS J=2$\rightarrow$1 and ^{13}CO J=1$\rightarrow$0) maps of these sources to date. The OVRO maps were combined with data from the 14 m FCRAO millimeter wave radio telescope, the VLA, IRAS, and the Palomar 5 m and 1.5 m optical telescopes.

A synthesis of the data reveals that although all three pre-main sequence objects are the sources of powerful, ionized stellar winds, only one, S87/IRS1, currently drives a bipolar molecular outflow. The inferred mass loss rates in the winds of S87/IRS1, LkHα101, and S106 IR are 1.8×10^{-5}, 1.7×10^{-6}, 1.1×10^{-5} $M_\odot$ yr^{-1}, with corresponding wind velocities of 160, 350, and 200 km s^{-1}. In all cases the wind velocities are lower, and the mass loss rates higher, than for main sequence stars of the same spectral types. Radiation pressure is inadequate to drive these winds, which can be anisotropic in their velocity fields.

The existence of massive, large-scale ($r \approx 10^{16}$ cm) disks, necessary for numerous proposed molecular outflow models, can now be ruled out. Only one of the many proposed molecular outflow models is consistent with the new observations (Königl 1982).

Although the observed winds can disperse a good portion of the cloud cores they inhabit, they cannot completely destroy these cores. Consequently, outflows from pre-

main sequence stars alone cannot account for the dispersal of molecular clouds, as some investigators have suggested.

Two glaring and intriguing problems remain to be solved in this field: the origin of the supersonic turbulence observed throughout a molecular cloud, and the driving mechanism of the powerful, ionized winds found in the high-mass, pre-main sequence stars.

Table of Contents

List of Tables

List of Figures

I. INTRODUCTION

The discovery of high-velocity, molecular outflows emanating from newly forming stars is perhaps the most spectacular result of millimeter-wave astronomy to date. Since the detection of the first outflow in Orion (Kwan and Scoville 1976; Zuckerman, Kuiper, and Rodriguez-Kuiper 1976), over one hundred molecular outflow sources have now been catalogued (Lada 1985), with the known list of outflow sources still growing (Levreault 1985; Margulis and Lada 1986; Heyer *et al.* 1987).

Molecular outflows were first recognized by the extremely broad wings (10–150 km s^{-1}) found in some CO (J = 1→0) emission line profiles toward embedded infrared sources in molecular clouds. Although molecular hydrogen is the major constituent of molecular clouds, it has no observable millimeter emission lines (Herzberg 1950). The next most abundant molecule, CO (Dickman 1979), is very stable with a dissociation energy of 11.1 eV, and is the molecule of choice for millimeter wave astronomy.

The presence of highly supersonic CO line wings, in itself, is not sufficient to designate a source as an outflow, since molecular clouds in general have linewidths (FWHM) on the order of 1–3 km s^{-1}, while the thermal velocities corresponding the cloud kinetic temperatures of 10–20 K are 0.35–0.5 km s^{-1}. The defining characteristic of an outflow source is that the highest observed velocities exceed the gravitational escape velocity. An estimate of the escape velocity may be made by deriving the molecular cloud mass interior to the radius at which the high-velocity gas is observed. Gas masses are determined from column density maps (see Equns. A(1)–A(6) of Scoville *et al.* 1986).

The first systematic search for molecular outflows resulted in a catalog of 48 objects (Bally and Lada 1983). Of these, 17 were classified as "high" velocity sources ($\Delta v \geq 30$ km s^{-1} at $T_R^* = 0.1$ K), 19 as "intermediate" velocity sources (10 km $s^{-1} \leq \Delta v \leq$ 30 km s^{-1}), and the rest as sources with "narrow" linewidths. The flow masses in these

sources range from 0.3–100 $M_\odot$, and their spatial extents from 0.1–3 pc. In many cases, the red- and blue-shifted CO emission map peaks do not coincide spatially. These are the "bipolar" molecular outflows. Although bipolar, they are not well collimated and are *not* jets. In fact, the molecular outflows are better described as swept-up shells of gas (Moriarty-Schieven *et al.* 1987; Levreault 1987).

Since the discovery of an outflow phase in the star formation process was unexpected, a number of theories to account for the observed molecular outflows have been proposed (Königl 1982; Draine 1983; Torbett 1984; Pudritz and Norman 1983, 1986; Uchida and Shibata 1985).

In the first model (Königl, 1982) the outflow is assumed to originate in a spherically symmetric stellar wind, which expands into a surrounding flattened mass distribution. The wind creates an interstellar bubble, which elongates in the direction of steepest, external density gradient. For density distributions of the form $\rho \propto r^{-n}$, $0 \leq n \leq 2$, the boundary of the bubble could become unstable to the formation of nozzles that channel the flow into two oppositely directed, supersonic jets. After the jets are formed, they are confined and collimated by the pressure of the medium through which they propagate. As long as the bubble or jets are confined to the molecular cloud, they push ahead of them dense layers of shocked and swept-up ambient material. These layers move at much lower velocities than the bubble (or jets) and make up the CO lobe emission.

The presence of a stellar wind is not required by the following outflow model (Draine 1983). As a starting point, this model assumes that the embedded protostar is rigidly rotating at nearly break-up speed and supports a kilogauss surface magnetic field, which is linked to the surrounding cloud's much larger-scale magnetic field. The star's rotational kinetic energy is converted to magnetic energy, because the magnetic field lines are assumed to be continuous between the pre-main sequence star and its ambient cloud. The

resulting magnetic pressure drives an expanding shock wave into the cloud. The major difference between this model and the previously described one (Königl 1982), is that the outflow source here is a "magnetic bubble" instead of a powerful stellar wind.

The next model (Torbett 1984) presumes that outflows are bipolar from the outset, instead of originating in a spherically symmetric flow that is subsequently channeled into a bipolar configuration. This model requires the existence of an accretion disk, whose vertical density profile is determined by the condition of hydrostatic equilibrium. In general, there will be a velocity difference between the innermost disk orbit and the stellar surface. As matter spirals into the central star through the disk, the kinetic energy corresponding to this velocity difference is presumed to be dissipated in a "boundary layer," which is assumed to be a single strong shock. When infalling matter through the disk hits the boundary layer shock, it heats up. The resulting thermal pressure drives matter off the disk surfaces, resulting in an intrinsically bipolar flow.

Yet another model requires a disk to explain the outflow mechanism (Pudritz and Norman 1983, 1986). The rotational energy of a massive disk ($M \approx 100\ M_\odot$) roughly 10^{16} cm in extent and with a rotational speed of about 10 km s^{-1} is postulated to be the energy source of the molecular outflows. In addition, the disk is assumed to contain a magnetic field parallel to its rotation axis and joined to the galactic field, as well as a low-density envelope, supported by ambipolar diffusion. An embedded protostar is assumed to increase the ionization fraction of its immediate surroundings so that ambipolar diffusion is increased, and the disk envelope is thereby accelerated. The magnetic-field configuration acting on the rotating, accelerated particles is supposed to result in a centrifugally driven wind previously described in the context of extragalactic radio jets (Blandford and Payne 1982).

The last model of the list above also assumes a magnetized accretion disk as the origin

of molecular outflows (Uchida and Shibata 1985). The disk's average density is taken as 10^7 cm^{-3} and its magnetic field strength as 3 mG. The origin of the disk magnetic field is from flux freezing of the interstellar magnetic field. The ideal MHD equations are then solved in cylindrical coordinates, assuming axial symmetry. The disk itself is assumed to be contracting, and therefore not in hydrostatic equilibrium. Initial conditions are assumed to be a uniform magnetic field parallel to the disk's rotation axis, a disk velocity field that is non-zero only in the azimuthal direction and scales as $r^{-1/2}$, and ad hoc density and pressure distributions, which assume the existence of a high temperature corona (T_{corona}/T_{disk} =400) of the same scale height as the disk. Evolution of this system was calculated numerically and resulted in a flow pattern of material outwards along the walls of a hollow cylindrical shell. A bipolar flow pattern along two hollow cylindrical shells follows from the symmetry of the problem.

The primary motivation for the work presented in this thesis is to understand the circumstances under which the molecular outflow phenomenon occurs. The order of magnitude improvement in the angular resolution available at millimeter wavelengths, achieved in the past three years with the advent of millimeter-wave interferometry, has made significant progress in this undertaking possible. Three of the "intermediate" velocity sources, S87, LkHα101, and S106, were mapped during 1985–1987 with the Owens Valley Radio Observatory's (OVRO) millimeter interferometer, which consists of three 10.4 m diameter elements. The resulting observations of each source were combined with data from the Infrared Astronomical Satellite (IRAS), the 14 m Five College Radio Astronomy (FCRAO) radio telescope, the Very Large Array (VLA), and optical imaging and spectroscopy from the Palomar 5 m and 1.5 m telescopes to construct a picture of the physical conditions unique to each source.

Chapter II is devoted to the study of S87, Chapter III to LkHα101, and Chapter IV to

S106. Each of these chapters consists of an introduction, a description of the observations, physical parameters that can be deduced directly from the observations, and a synthesis of the results into a consistent source model. Chapter V, on outflows from high-mass, pre-main sequence stars, contains the major conclusions to be drawn from the previous three chapters, followed by suggestions for future research.

When viewed in the context of the theoretical outflow models described above, the observational results presented in this thesis show that for high mass pre-main sequence stars, a powerful ionized stellar wind does indeed exist in every instance. Furthermore, high mass, extended ($r \approx 10^{16}$ cm) disks are not observed. Originally, spherically symmetric ionized winds can and do result in a bipolar morphology of the associated molecular outflow. Taken together, the data support the first outflow model outlined above (Königl 1982) while they directly contradict assumptions crucial to each of the other models.

REFERENCES

Bally, J. and Lada, C. 1983, *Ap. J.*, **265**, 824.

Blandford, R. and Payne 1982, *M.N.R.A.S.*, **199**, 883.

Dickman, R. L. 1979, *Ap. J. Suppl.*, **37**, 407.

Draine, B. T. 1983, *Ap. J.*, **270**, 519.

Herzberg, G. 1950, *Molecular Spectra and Molecular Structure* D. Van Nostrand Company, Inc., Princeton, New Jersey.

Heyer, M.; Snell, R. L.; Goldsmith, P. F.; Myers, P. C. 1987, *Ap. J.*, **321**, 370.

Königl, A. 1982, *Ap. J.*, **261**, 115.

Kwan, J. and Scoville, N. Z. 1976, *Ap. J. Letts.*, **210**, 39.

Lada, C. 1985, *Ann. Revs. Astr. Ap.*, **23**, 267.

Levreault, R. M. 1985, Ph. D. Thesis, University of Texas, Austin.

Levreault, R. M. 1987, *B.A.A.S*, **19**, 725.

Margulis, M. and Lada, C. 1986, *Ap. J. Letts.*, **309**, 87.

Moriarty-Schieven, G.; Snell, R. L.; Strom, S. E.; Schloerb, F. P.; Strom, K. M.; Grasdalen, G. L. 1987, *Ap. J.*, **319**, 742.

Pudritz, R. E. and Norman, C. A. 1983, *Ap. J.*, **274**, 677.

Pudritz, R. E. and Norman, C. A. 1986, *Ap. J.*, **301**, 571.

Scoville, N. Z.; Sargent, A. I.; Sanders, D. B.; Claussen, M. J.; Masson, C. R.; Lo, K. Y.; and Phillips, T. G. 1986, *Ap. J.*, **303**, 416.

Torbett, M. V. 1984, *Ap. J.*, **278**, 318.

Uchida, Y. and Shibata, K. 1985, *Publ. Astron. Soc. Japan*, **37**, 515.

Zuckerman, B.; Kuiper, T. B. H.; and Rodriguez-Kuiper, E. N. 1976, *Ap. J. Letts.*, **209**, 137.

II. S87

II. A. INTRODUCTION

Observational studies of star-forming regions may be classified into two categories: statistical studies of a large number of sources or detailed studies of one or a few sources. In either case, the wavelength range coverage in any one study has been limited. The aim of this work is to combine detailed observations of one particular site of star formation, S87, from many separate wavelengths. This approach emphasizes the large range of physical conditions that occur simultaneously in any active, star-forming region and that must all be fit into a unified, self-consistent model. The observations reported here will be used to clarify the origin of the supersonic velocities in the cold, molecular gas associated with S87.

S87 is the site of a plethora of phenomena associated with star formation. Although first discovered as an optical HII region (Sharpless 1959), S87 is a bright source of infrared, radio continuum, and molecular line emission. It is also the site of highly variable H_2O maser emission (Blair *et al.* 1980, Bally 1981, Henkel *et al.* 1986). The far-infrared emission from S87 was detected by the AFGL survey (Price and Walker 1976), in which it is designated CRL 2454. IRAS observations of S87 show it to be a strong, far-infrared source at all observed wavelengths. Its energy distribution cannot be fit by a single blackbody, even when corrected for wavelength-dependent opacity, indicating a wide range of temperatures along the line of sight to the source. A search of the region for near-infrared sources led to the discovery of an extended ($20'' \times 30''$) component called IRS1 (Bally 1981), which is spatially coincident, within the measurement errors, with the emission peaks in the far-infrared, radio continuum, and molecular lines. Previous radio continuum observations of S87 at 6 cm allow one to infer a Lyman continuum flux of 3.0×10^{47} photons s^{-1}, corresponding to an embedded B0 ZAMS star (Felli and Harten 1981). More

recent, high-spatial resolution (0.5″ at 6 cm) radio continuum observations show S87 to contain a compact radio core, surrounded by an extended, fan-shaped structure to its south (Bally and Predmore 1983). The distance to S87 is 2.1 kpc, as determined from the galactic rotation curve given by Clemens (Clemens 1985), the source V_{LSR} = 22 km s^{-1}, and l^{II} = 61°. Single-dish mapping of S87 in CO (J=1→0) at 2.6 mm reveals that the optical HII region coincides spatially with the peak CO emission from a 3.6 pc diameter molecular cloud of roughly 7000 $M_\odot$, of which the inner 2′ core contains 500–1000 $M_\odot$ of gas (Bally 1981). S87 is listed as an "intermediate" velocity width source (ΔV_{FWHM} = 5 km s^{-1}) in a catalog of sources that were searched for high-velocity molecular gas (Bally and Lada 1983). These authors state that for sources such as S87, it is difficult to decide whether the observed line width reflects localized energetic activity, rotation, or turbulent gravitationally bound motion in the ambient molecular cloud. In a recent review article on cold outflows, however, S87 is listed as a "high-velocity, molecular outflow source" (Lada 1985).

The present observations, which can be used to distinguish among the above-mentioned possibilities, are described in § II. B. Section II. C contains the results from which model-independent physical parameters for S87 are derived. A source model, consistent with all the observational data, is developed in § II. D. Finally, a brief summary of the results is presented in § II. E.

II. B. OBSERVATIONS

1) Radio Continuum

S87 was observed with the Very Large Array [1] in all its standard configurations (A,B,C, and D) at 2, 6, and 18 cm. The "matched" array design feature of the VLA was

[1] NRAO is operated by Associated Universities, Inc., under contract with the National Science Foundation.

fully utilized (Thompson *et al.* 1980), resulting in radio maps of identical resolution at several different frequencies. Integration times were chosen to give identical noise levels in all the images. The primary flux calibrator was 3C286, for which the adopted fluxes were 3.45 Jy at 2 cm, 7.41 Jy at 6 cm, and 14.51 Jy at 18cm. Suitable restrictions were applied during the course of amplitude calibration to compensate for the extended structure of 3C286 (see *The VLA Calibrator Handbook 1986*). On-source observations were alternated with those of the phase calibrator, 1923+210, every twenty minutes. The pointing center coordinates for S87 were $\alpha_{1950} = 19^h\ 44^m\ 13.68^s$, $\delta_{1950} = 24°\ 28'\ 05.10''$ (Bally and Predmore 1983). All other relevant observational parameters are listed in Table II.1. The Astronomical Image Processing System (AIPS) software routine "MX" was used for image construction and beam deconvolution.

2) IRAS

The IRAS survey data were coadded for fifty-one individual passes over the S87 region. The point source filtered FLUX grids (*IPAC User's Guide 1986*) were the starting point for determining the flux of S87 in each of the four IRAS bands. FLUX grid output values for S87 were corrected for detector non-linearities, errors due to coadd processing, and sampling and position uncertainties. No color correction was applied, since the energy distribution of S87 in the IRAS bands is neither a blackbody nor a power law. The Coadd Intensity Grids were used for determination of the flux from the extended emission, after suitable background level subtraction was performed. Azimuthally averaged profiles of the intensity distribution at each IRAS band were constructed by fitting ellipses to the data in logarithmic steps of the radial coordinate.

3) Optical

A high-resolution spectrum of the optical nebulosity associated with S87 was obtained on the night of 15 November 1987 at the Coudé focus of the Hale 5-meter telescope. The

reflection grating used was ruled at 600 grooves/mm with a blaze angle of 13°00′, yielding a dispersion of 0.281 Å/15 μm pixel in first order at the 36-inch focal length "camera" position. At the central wavelength of 6650 Å, the wavelength coverage was 200 Å. A 3 mm thick GG495 pre-filter was used to block out light from higher orders. The detector was a TI 800 × 800 CCD (Gunn, Harris, and Oke 1987). The slit width was 0.4″ on the sky, allowing 25 km s^{-1} velocity resolution. The 30″ long slit was kept in a north-south orientation on the sky with the aid of a dove-prism image rotator. The telescope pointing position was determined by offset from a nearby SAO star, and was checked every fifteen minutes during the exposure. On-source integration time was 2-1/2 hours.

The data were erase-level subtracted, flat-fielded, and transformed to a flux scale, using HD19445 as the flux standard (Oke and Gunn 1983). The wavelength scale was determined using a Th-Ar comparison arc (courtesy Dr. Geoff Marcy).

4) Molecular Lines

a) FCRAO[2]

S87 was observed in ^{13}CO in April and in CO (J = 1→ 0) in June of 1986 with the Five College Radio Astronomy Observatory (FCRAO) 14 m antenna. The HPBW was 45″ at these frequencies. Representative system temperatures were 450 K at ^{13}CO and 840 K at CO. Spectra were obtained by position-switching to a region devoid of emission, ($\alpha_{1950} = 19^h44^m13.7^s$, $\delta_{1950} = 24°34'04''$). The observed 2′ field was centered on the VLA peak coordinates and overlapped the OVRO primary beam. This area was subdivided into a 9 × 9 element grid, with 15 arc-second offsets between adjacent grid points. The entire field was scanned six times, with 15 seconds integration time per point per pass.

[2] The Five College Radio Astronomy Observatory is supported by the National Science Foundation and the Commonwealth of Massachusetts and is operated by permission of the Metropolitan District Commission.

The data were calibrated by inserting an ambient temperature load in the beam. The raw data were corrected for atmospheric and forward scattering losses (η_{fss} in the terminology of Kutner and Ulich 1981). The source was assumed to uniformly fill the beam, so no correction was made for source coupling efficiency. A 256 × 100kHz filterbank was used, resulting in 0.27 km s^{-1} velocity resolution.

b) OVRO

Millimeter-wave observations were made with the 3-element interferometer of the Owens Valley Radio Observatory, operated by the California Institute of Technology, during the 1985-86 and 1986-87 observing seasons. Maps were made of both the CS (J=2→1) and ^{13}CO (J=1→0) emission lines. The synthesized beam FWHM was 11″ × 5″ for the CS observations, and 6.8″ × 6.5″ for the ^{13}CO. The amplitude calibrator, W3(OH), was taken to be 4.0 Jy. Systematic uncertainties in the amplitude calibration are 20%. The phase calibrator, 2021+317, was observed every twenty minutes, and positional errors are estimated to be 20% of the synthesized beam. The source V_{LSR} was 22 km s^{-1}. Relevant observational parameters are listed in Table II.2. The AIPS software package was used to produce final maps with the "MX" routine.

II. C. RESULTS

1) Radio Continuum

An optical r band RCA CCD image of S87, taken on 24 July 1987 in photometric conditions at the Palomar 1.5 m telescope, is shown in Figure II.1a (courtesy of Dr. James Schombert). The image extent is 123″ square. The sky background in this frame is 21.3 r magnitudes/arcsec^2, while the outer contour of the grey-scale image of S87 is at 24.0 r magnitudes/arcsec^2. The average surface brightness of the nebula is 22.5 r magnitudes/arcsec^2, while the peak surface brightness is between 20.0 and 20.2 r magnitudes/arcsec^2. The black objects in the frame are stars. The knots, marked A and

B in the figure, had previously been identified as two lobes of a bipolar nebula (Cohen *via* Bally 1987). The lowest resolution, largest field of view radio continuum image of S87, is shown in Figure II.1b, superposed on the optical contours. The radio emission region is more deeply buried inside the cloud core than the optical. Note the distinct lack of an optical counterpart to the radio continuum peak. This implies that $A_V = 35$ mag to S87/IRS1.

The radio morphology at the scale of Figure II.1 is identical in the 2 cm D array, the 6 cm C array, and the 18 cm B array maps. The emission at each frequency is dominated by the core source from which the extended, low-intensity emission lobe originates. Physical parameters of this lobe, derived from the VLA data, are listed in Table II.3. The lobe contains ≈ 1 $M_\odot$ of low density ($n_e \approx 700$ cm^{-3}) ionized gas, assuming no clumping of the gas, and its spectral index is consistent with optically thin Bremsstrahlung.

Figure II.2 shows the 2 cm and 6 cm morphologies at three times better resolution. The core source still dominates the total flux in each map. At this resolution, the extended emission lobe is mostly resolved out. The compact core and emergent, fan-shaped extended emission in this figure have been previously observed with the VLA in A array (Bally and Predmore 1983). Figure II.3 shows the highest-resolution data, in which the core is resolved. At 2 cm, the core is well fit by a Gaussian of FWHM $0.73'' \times 0.67''$, corresponding to linear dimensions of 1500 × 1400 AU, at a position angle of 19°. The derived, average electron density in this core is 8×10^4 cm^{-3}, corresponding to 1.08×10^{-3} $M_\odot$ of ionized gas. The core fluxes, as measured at different times and frequencies with the VLA, are given in Table II.4. There is a hint of source variability at the 10–20% level on time scales of months. The core spectral index ($S_\nu \propto \nu^\alpha$) lies in the range $-0.21\pm0.2 \leq \alpha \leq +0.22\pm0.2$ between 6 cm and 2 cm and $\alpha = +0.40\pm0.2$ between 6 cm and 20 cm. The quoted uncertainties assume a 10% flux uncertainty at each frequency.

For optically thin emission, the Lyman continuum flux required to keep the entire region (core + envelope) ionized is 1.9×10^{47} photons s^{-1}, consistent with that expected from a B0 ZAMS star (Panagia 1973). The bolometric luminosity of such a star is 2.5×10^4 $L_\odot$, to be compared with the observed luminosity of 3.5×10^4 $L_\odot$ (see §II. C. *2*).

2) IRAS

The fluxes of S87/IRS1 in the four IRAS bands, as determined from the Coadd FLUX grids, are 44 Jy at 12 μm, 395 Jy at 25 μm, 3100 Jy at 60 μm, and 5000 Jy at 100 μm. The corresponding fluxes from the extended component, exclusive of the central source, are 213 Jy at 12 μm, 455 Jy at 25 μm, 1900 Jy at 60 μm, and 4250 Jy at 100 μm. Figure II.4 represents the IRAS emission from the S87 molecular cloud.

The radial intensity distributions of these IRAS maps are plotted in Figure II.5. Note from this figure how well the large-scale, surface brightness distributions fit the r^{-3} law represented by the solid line in the upper right-hand corner. Factoring out the r^{-2} falloff of flux from the central source, we are left with the conclusion that the dust *surface* density must fall off as r^{-1}, or, equivalently, that the dust density per unit volume must scale as r^{-2}!

The spectral energy distribution of S87 is plotted in Figure II.6. Integration under this curve over the range 1 μm $\leq \lambda \leq$ 2.6 mm yields a total luminosity of 3.5×10^4 $L_\odot$ for the S87 region, at 2.1 kpc distance. Although this derived luminosity for S87/IRS1 includes a contribution from IRS2, since both sources fall within the IRAS beam, the contribution of IRS2 to the total luminosity is negligible, since IRS1 has a steeply rising near-infrared continuum, whereas that of IRS2 is nearly flat (Bally 1981).

3) Optical

The Coudé spectrum of S87, integrated along a 30″ long north-south slit, centered at the position of S87/IRS1, is presented in Figure II.7. Night-sky neon lines, marked NS,

are apparent in this figure. Unfortunately, both the nebular HeI (6678 Å) and [SII] (6717 Å) lines are contaminated, the latter rendering a density determination impossible.

The Hα line, shown in Figure II.8, is uncontaminated. Note that the entire line is blue-shifted with respect to the cloud-rest velocity, leaving no doubt as to its association with the S87 molecular cloud. The red-shifted part of the Hα line profile, representing ionized gas moving into the cloud, is so obscured as to be undetectable. Assuming that the Hα line is, in fact, symmetric about the cloud rest velocity, its FWZI width must be 320 km s^{-1}. Since the Hα emitting gas is spatially coincident with the VLA emission (see Figure II.1), the observed VLA lobe is clearly associated with the molecular cloud.

4)Molecular Lines

a) FCRAO

Figure II.9 consists of four panels, for ease of comparison of the S87 single-dish data. Figure II.9a shows contours of *peak* CO brightness temperature. Note how the temperature falls monotonically from its 34 K maximum near the VLA peak position at map center. Figure II.9b shows contours of the ^{13}CO column density in a 2′ × 2′ field centered on S87/IRS1. This map was derived by combining the CO and ^{13}CO data (*viz.*, Milman 1977; Scoville *et al.* 1986). Using Equation (A6) of the latter yields a mass of gas of 700 $M_\odot$ in the entire FCRAO field, with [H_2/CO] = 5.6 × 10^3 (Dickman 1979). This mass corresponds to a 3 km s^{-1} escape velocity at the map edge. The molecular gas mass in S87/IRS1 within an OVRO primary beam is 123 $M_\odot$, corresponding to a 2 km s^{-1} escape velocity at 0.26 pc from the VLA peak. The observed radial velocities are ± 4 km s^{-1} (FWZI) about line center, which is at V_{LSR} = 22 km s^{-1}. The red- (V_{LSR} = 18→20 km s^{-1}) and blue-shifted (V_{LSR} = 24→26 km s^{-1}) line emission is shown in Figure II.9c. Note the spatial overlapping of the blue- and red-shifted gas. This observation will be used in developing the geometrical model of S87 in § II.D. The FCRAO blue- and red-

shifted emission peaks do not lie on the line connecting the OVRO blue- and red-shifted emission peaks. The highest-velocity, red-shifted FCRAO emission peak is north of this line, while the highest-velocity, blue-shifted FCRAO emission peak is to its south. If we model the molecular gas kinematics as originating from two radially expanding cones centered on S87/IRS1 (see § II. D), then the above observations show the ambient cloud gas deflecting the molecular outflow. The last panel, Figure II.9d, shows the large-scale, ionized gas emission from S87 for comparison (VLA 2 cm D array).

Figure II.10 shows CO and ^{13}CO line profiles at positions along a line defined by the OVRO CS peak positions. Although the red-shifted gas dominates in the northeast, and the blue-shifted gas dominates in the southwest, *note that there is both blue- and red-shifted gas present at each position.* The model of the gas kinematics developed in § II. D will make use of this observation, as well.

b) OVRO

The millimeter interferometer measured a 3σ peak flux of 41 mJy/beam in the 110 GHz continuum at the VLA core position. The 6 cm flux in an area equivalent to the OVRO beam is 50 mJy. Assuming that the emission is from an optically thin HII region ($S_\nu \propto \nu^{-0.1}$), the expected 110GHz flux is 37 mJy. The ^{13}CO line contamination in the 250 MHz continuum channel of the interferometer is 22 mJy/beam at this position. Thus, all of the observed millimeter continuum flux is easily accounted for as either free-free or line emission.

Figure II.11 shows an overlay of the CS (J=2→1) emission superimposed on the VLA 6 cm continuum map. The northern lobe is red-shifted by $\approx$ 3 km s^{-1} relative to the southern lobe. The strongest optical emission coincides spatially with the blue-shifted molecular gas.

The ^{13}CO maps, covering a 4.4 km s^{-1} velocity range, are presented in Figure II.12. Most of the observed emission (Figures II.12b and II.12c) is at the line core, although the high-velocity molecular emission does start to show in the first and last few high-velocity resolution channels (Figures II.12a and II.12d). Note the clear spatial separation of the blue- and red-shifted emission regions. It is important to note the excellent spatial correlation between the high-velocity ^{13}CO and the CS emission lobes, since it is the case that many sources exhibit quite different morphologies when observed in the emission of different molecules (*e.g.*, Plambeck *et al.* 1982; Wright *et al.* 1983; Vogel *et al.* 1984; Vogel *et al.* 1985; Plambeck and Wright 1987). The blue- and red-shifted emission peaks in ^{13}CO and CS coincide. This coincidence of spatial structure in the two molecular species means that we are seeing gas dynamics in the source, not just chemistry, abundance, or excitation effects.

To further elucidate the velocity structure in these lobes, the ^{13}CO line shapes are plotted in Figure II.13, at three positions. Any negative brightness temperatures, which exceed the noise level in this figure, are due to poor sampling of the data in the UV plane. Absorption is ruled out because the equivalent brightness temperature of the continuum emission is below the 1 K level, whereas the greatest observed, negative brightness temperature is as large as -10 K. In Figure II.13, OVRO line profiles are the solid lines, whilst the FCRAO line profiles are dashed. Figures II.13a, II.13b, and II.13c show the ^{13}CO line shapes at the OVRO blue-shifted peak CS emission position, the VLA peak position, and the OVRO red-shifted peak CS emission position, respectively. Note the OVRO ^{13}CO line profile of Figure II.13a is still rising at the most extreme, blue-shifted velocity. Similarly, the red-shifted OVRO ^{13}CO line profile is rising at the most extreme, red-shifted velocity. Clearly, there is higher velocity red- and blue-shifted gas than could be observed with the available 4.4 km s^{-1} bandwidth. This is confirmed by the observed

velocity extent of the FCRAO line profiles. The mass estimates derived from these data are therefore lower limits. Comparison of the single-dish and OVRO line shapes of Figure II.13 immediately shows that there is extended red-shifted gas at the OVRO blue-peak position, and extended blue-shifted gas at the OVRO red-peak position. We will make use of this important observation in the source model developed in § II. D.

The mass in molecular gas inferred from the OVRO data is 19 $M_\odot$ in the red wing (23.3→24.1 km s^{-1} velocity range) and 23 $M_\odot$ in the blue wing (19.7 → 20.3 km s^{-1} range). Note that the OVRO mass estimates are strict lower limits, insofar as some of the observed emission was found to be optically thick. Integration of *all* the observed ^{13}CO emission in the OVRO field yields a mass of 109 $M_\odot$. This mass is to be compared with the 123 $M_\odot$ value detected by FCRAO within an OVRO primary beam area. Thus, escape velocity at the OVRO peak positions is 4 km s^{-1}, allowing for a 20 $M_\odot$ embedded star, in addition to the molecular gas mass. The mass determinations were made using equations A(3), A(5), and A(6) of Scoville *et al.* 1986, assuming that $\tau < 1$, $H_2/CO = 5.6 \times 10^3$, $^{13}CO/CO = 1/89$, a mean molecular weight, $\mu_0 = 1.36$, and $T_{ex} = 30$ K. The chosen value of T_{ex} is based on the observed brightness temperature in the single-dish data.

Figure II.14 shows the ^{13}CO gas kinematics. V_{LSR} at the peak of each emission spectrum is plotted as a function of projected distance from the VLA core position. For kinematical analysis of the molecular line data, we will adopt $V_{LSR} = 23$ km s^{-1}, which is more consistent with the spectra of Figure II.10 than the previously used value of 22 km s^{-1}. The highest-velocity data points in Figure II.14 are from the single-dish data, and are represented by the open diamonds. Filled-in diamonds represent the OVRO data. Figure II.14 shows that the gas reaches a (*projected*) terminal velocity of 3 km s^{-1} on large scales. The straight line fit has a slope of 18 km s^{-1}/pc, which implies an expansion time scale of

5.4×10^4 years for an outflow. The dashed curve of Figure II.14 depicts the locus of points expected for marginally bound gas motion about a 21 $M_\odot$ central mass, chosen to fit the most OVRO data points possible. Curves depicting any gravitationally bound motions, be they infall or rotation about a centrally condensed mass, would have *qualitatively* the same shape as the dashed curve of Figure II.14. However, if the gas density at these small scales (5″) were to follow the r^{-2} law deduced for the dust distribution at much larger scales (1′), then the included mass at a given radius, M(r), would scale linearly with r, for centrifugally supported, gravitationally bound motion. If this were the case, the observed velocities would be independent of radius, contrary to the data of Figure II.14.

II. D. INTERPRETATION AND DISCUSSION

1) Origin of Supersonic CO J=1→0 Linewidth

The possible scenarios that could account for the suprathermal molecular linewidths in S87 are: the superposition of many sources travelling at different velocities along the line of sight, infall, rotation, or outflow. Examination of each of these possibilities leads to the conclusion that the observations are best explained by molecular-gas outflow into two oppositely directed lobes.

The spatial distribution of the red and blue wing emission of Figures II.9c, 11, 12a, and 12d, all show coherent spatial structure, unlike that expected from the superposition of many cloudlets with uncorrelated velocities. Furthermore, the observed CO and ^{13}CO line profiles (*e.g.*, Figure II.10) disagree with those predicted by microturbulent cloud models (Leung and Liszt 1976; Kwan 1978). Finally, the OVRO interferometer detected only two cloud condensations at velocities significantly different from line center (Figure II.11). Thus, the combined spatial *and* velocity structure observed in S87 cannot be accounted for by a microturbulent cloud model alone.

Infall is ruled out by the observed velocity law of Figure II.14, which shows radial

velocity to be an *increasing* function of distance from cloud center, contrary to what is expected for motion resulting from gravitational collapse. If we assume that the observed spatial and velocity structure of the molecular gas is due to rotation of a coherent gas structure, then we would expect to see only red-shifted gas on one side of the rotation axis, and only blue-shifted gas on the other, contrary to what is observed (see Figures II.9c and II.13).

The observed kinematics suggests that the highest velocities appear at the greatest distances from S87/IRS1, as would be expected for an explosive, free, expansion. Gas outflow, therefore, is left as the viable explanation for the combined spatial and velocity structure of the molecular gas.

A cartoon representation of the S87 outflow is shown in Figure II.15 (adapted from Cabrit and Bertout 1986). Figure II.15a shows the outflow geometry, in which the arrow is pointing toward the observer, and the inclination angle is indicated by the letter *i*. Figure II.15b depicts the expected structure of the CO (J = 1 → 0) emission from Figure II.15a for $n_{H_2} = 10^4$ cm^{-3}, $T_K = 10$ K, inclination angle = 50°, cone opening angle = 60°, ratio of maximum/minimum cone radius = 10, v(r) ∝ r, and Sobolev optical depth $(\frac{8\pi^3}{3h}\mu^2 n_{CO}\frac{r}{v(r)}) = 100$. It is particularly illuminating to compare the single-dish and OVRO maps of S87 with Figure II.15b. Several key observations, referred to earlier, are readily explained by modelling S87 as a biconical outflow with a wide opening angle viewed at large inclination. These are: the overlap of the red and blue wings in the single dish map of Figure II.9c, the low, observed radial velocities, and the fact that compact OVRO red-shifted emission is embedded in extended, blue-shifted gas, and compact OVRO blue-shifted emission is embedded in spatially extended, red-shifted gas. Note that *any* viable model of this source must account for these seemingly unrelated observations.

2) Outflow Characteristics and Driving Mechanism

Only a small fraction (5%) of the cloud core gas mass reaches escape velocity. The mass of gas in the 19→20 km s^{-1} velocity interval is 11 $M_\odot$, while that in the range $25<V_{LSR}<26$ km s^{-1} is 23 $M_\odot$. For gas moving at 3 km s^{-1} from line center, this amounts to 102 $M_\odot$ km s^{-1} of momentum in the high-velocity gas alone, with a corresponding kinetic energy of 9×10^{45} ergs. The slope of the linear fit of Figure II.14 gives a timescale of 5.4×10^4 years for the outflow, yielding momentum- and energy-supply rates of 1.2×10^{28} gm cm s^{-2} and 5.4×10^{33} erg s^{-1}, respectively, for the molecular gas in the above velocity intervals. If the ionized gas is to provide the required momentum to accelerate the molecular gas, then the tenuous (700 cm^{-3}) ionized gas apparent in the radio and optical images of Figure II.1 must lie mostly behind the large-scale, blue-shifted molecular gas and in front of the corresponding red-shifted molecular gas. Furthermore, the ionized gas detected by the VLA must be moving into the S87 cloud away from us, while the optically visible, ionized gas is moving out of the cloud towards us. The Hα line profile of Figure II.8 strongly supports this geometrical model, since this spectrum was obtained along a 30″ long N-S slit centered on the VLA peak position. Nearly the entire Hα line in S87 is blue-shifted with respect to the cloud's rest velocity, which is at $V_{LSR} = 23$ km s^{-1}. If we assume that the Hα line to be symmetric about the cloud rest velocity, then the Hα line's FWZI is 320 km s^{-1}, suggesting an ionized wind velocity of 160 km s^{-1}, not accounting for projection effects.

The time evolution of a stellar wind interacting with its surroundings passes through four recognizable stages (Castor, McCray, and Weaver 1975): an initial phase of free expansion at the wind velocity lasting a few centuries; an adiabatic expansion phase lasting a few thousand years; a "snowplow" phase in which swept-up gas forms a shell; and the shell dissipation stage. The S87 stellar wind must be in its "snowplow" phase, given the molecular outflow time scale of 5.4×10^4 years. At this stage, the spatial

structure of the gas, progressing outwards from the source, consists of four zones (Cox 1972): a) the stellar wind, b) the shocked stellar wind, c) the swept-up shell, and d) the ambient cloud. It is the shocked stellar wind of region b) that imparts momentum to the surrounding molecular gas. The equation of motion of the swept-up shell gas (assuming an isotropic, homogeneous density distribution) is (Avedisova 1972):

$$R_s(t) = 3.61 \times 10^4 \left(\frac{\dot{M} V^2}{n_o} \right)^{1/5} t^{3/5} cm,$$

where R_s is the shell radius, $\dot{M}$ is the stellar mass loss rate, V is the wind velocity, n_o is the molecular gas density, t is the age of the system, and all units are *cgs*. If we assume that the entire solar mass of ionized gas detected by the VLA originated in the stellar wind, then the mass loss rate is 1.85×10^{-5} $M_\odot$ yr^{-1}. For a 160 km s^{-1} wind, surrounding molecular gas density of 8×10^4 cm^{-3}, and age of 5.4×10^4 years, the derived shell radius and velocity, 0.26 parsecs and 3 km s^{-1}, are in excellent agreement with the observed values.

While the shocked wind can provide the impetus to accelerate the surrounding molecular gas, the "channeling" of the flow into bipolar lobes in S87 still requires explanation. The bipolarity in S87 is a large-scale phenomenon, and must therefore result from the density structure of the ambient molecular cloud. This inference is supported by the column-density-distribution contour plot of Figure II.9b, which, when compared with the outflow axis of Figure II.9c, shows that the flow follows the direction of steepest column density gradient. Furthermore, the gas density enhancement that provides a barrier to gas flow to the northwest of the VLA peak is apparent from the VLA, optical, and OVRO ^{13}CO morphologies. How is a density gradient conducive to the formation of bipolar flow channels established? One promising explanation is that bipolarity follows from the dynamical interaction of the expanding stellar wind with a posited, ambient cloud, magnetic field (Königl 1982). According to this model, if the initial cloud density distribution is a

decreasing function of distance from the cloud core, the bubble's side walls move in, resulting in a "pinching" motion in the equatorial region, and the bubble's ends accelerate. These predictions at once account for two unrelated, previously inexplicable observations in the S87 outflow: that the densest parts of the flow lobes (the OVRO CS peaks) are closest to the shocked wind region (Figure II.11), and that the largest outflow velocities are found at the largest spatial scales (see Figure II.14).

3) Nature of the Embedded Outflow Source

The peculiar VLA morphology of S87 can be explained by postulating a 4 km s^{-1} relative motion, in the plane of the sky, between the compact component and its associated extended emission, assuming that the compact source was initially centrally located in the larger-scale lobe (see Figures II.1 and II.2). Such motion would not alter the outflow gas dynamics discussed above (Weaver *et al.* 1977).

As noted earlier, the bolometric luminosity of the region, as determined from Figure II.6, is 3.5×10^4 $L_\odot$, while that of a B0 ZAMS star, needed to provide photoionization equilibrium, is 2.5×10^4 $L_\odot$. However, the exciting source of S87 must be a *pre-main-sequence* object, given the short HII region expansion and molecular outflow time scales. The quoted B0 ZAMS luminosity would then be an *underestimate* of the true source luminosity (Ezer and Cameron 1967). The observed ionizing photon flux and luminosity can, therefore, be reconciled as arising from a single, embedded 20 $M_\odot$ pre-main-sequence object.

The idealization of the S87 ionizing photon flux as time-independent is called into question by the VLA core flux measurements (see Table II.4). Although the VLA core is spherically symmetric (Figure II.3), its spectral index is *not* that expected for a *steady*, isotropic stellar wind (Wright and Barlow 1975, Panagia and Felli 1975), yet optical spectroscopy reveals the presence of a stellar wind in the region.

II. E. SUMMARY

Observations of the S87 star-forming region have been made at optical, far-infrared, centimeter, and millimeter wavelengths with the goal of explaining the origin of the previously discovered supersonic molecular gas in this source. S87/IRS1 is a massive (≈ 20 $M_\odot$), pre-main-sequence object still embedded in its parent molecular cloud, but disrupting its surroundings through the action of its powerful stellar wind ($\dot{M} = 1.8 \times 10^{-5}$ $M_\odot$ yr $^{-1}$, $V_w = 160$ km s^{-1}). The shocked wind gas provides the required force to accelerate the surrounding molecular gas to supersonic velocities. An ordered, large-scale magnetic field is postulated to set up an initially anisotropic pressure distribution, which channels the flow into two oppositely directed lobes, and provides some further acceleration to the already supersonic molecular gas. Only a small mass fraction (5%) of the molecular gas actually reaches escape velocity.

TABLE 1

VLA Observational Parameters

Date	ν (GHz)	Bandwidth (MHz)	Array	No. of Antennae	Int. Time (Mins.)	Clean Beam FWHM (″)	Clean Beam P.A. (°)	Noise (mJy/beam)
1987 SEP 03	5	100	A	25	28	0.32 × 0.31	−40.6	0.10
1987 SEP 03	1.4	50	A	25	25	1.19 × 1.09	−58.4	0.10
1987 DEC 07	15	100	B	26	187	0.51 × 0.36	−75.7	0.07
1987 DEC 07	5	100	B	26	30	1.40 × 1.34	−50.9	0.10
1987 DEC 07	1.4	50	B	26	66	3.79 × 3.68	−40.59	0.22
1987 JAN 10	15	100	C	27	180	1.19 × 1.14	−60.45	0.10
1987 JAN 10	5	100	C	27	30	3.95 × 3.80	−63.80	0.20
1987 MAR 09	15	100	D	27	209	3.57 × 3.31	+4.30	0.13

TABLE 2

OVRO Observational Parameters

Molecule	Filterbank	Configuration			Date	LST Range
CS	32×1MHz	10E	10W	20N	1985 APR 21	22:37–00:09
		10E	10W	20N	1985 MAY 04	17:00–23:00
		30E	50W	00N	1985 MAY 08	14:00–20:30
		50E	50W	10W	1985 MAY 29	14:30–20:50
^{13}CO	32 × 50kHz	10E	10W	20N	1985 DEC 09	14:30-00:33
		20W	00N	30E	1985 DEC 28	15:20–00:27
		10W	65W	50W	1986 FEB 10	14:30–20:30
		30E	30W	20N	1986 MAR 15	14:30–17:00
		30E	30W	20N	1986 MAR 16	15:10–21:40
		30E	30W	20N	1986 MAR 23	15:15–22:30
		30E	60N	30W	1987 FEB 02	14:30–21:50

TABLE 3

S87 RADIO LOBE PARAMETERS

	2CM D ARRAY	6CM C ARRAY	20CM B ARRAY
Obs. Date	1987 MAR 09	1987 JAN 10	1987 DEC 07
Lobe Extent (arcsec^2)	1640	2042	3370
Integrated Flux[1] (mJy)	378	535	572
n_e (cm^{-3})	900	700	500
M_{lobe} ($M_\odot$)[2]	0.81	0.90	1.4

[1] Includes core source flux.

[2] Assumes fully ionized hydrogen gas.

TABLE 4

S87 Core Flux

Date	ν (GHz)	Array	Clean Beam FWHM (″)	Clean Beam P.A. (°)	Peak Flux (mJy/beam)	Core Flux† (mJy)
1987 SEP 03	1.4525	A	1.27 × 1.17	−56.34	7.48	15.2
1987 DEC 07	1.3825	B	3.79 × 3.68	−40.59	20.83	17.1
1987 SEP 03	4.885	A	0.37 × 0.36	−50.10	4.93	24.8
1987 DEC 07	4.885	B	1.40 × 1.34	−50.92	22.37	30.3
1987 JAN 10	4.885	C	4.17 × 4.01	−61.05	36.63	23.2
1987 DEC 07	14.965	B	0.51 × 0.36	−75.69	6.39	23.9
1987 JAN 10	14.965	C	1.24 × 1.22	−51.20	20.65	29.7
1987 MAR 09	14.965	D	3.60 × 3.32	+3.36	30.25	23.7

†Core fluxes were determined for the central 4″ × 4″ in each map.

REFERENCES

Avedisova, V. S. 1972, *Soviet Astr. – AJ*, **15**, 708.

Bally, J., 1981 Ph.D. Thesis, University of Massachusetts at Amherst.

Bally, J. and Lada, C. 1983, *Ap. J.*, **265**, 824.

Bally, J. and Predmore, R. 1983, *Ap. J.*, **265**, 778.

Blair, G. N.; Dinger, A.; Dickinson, D. F. 1980, *A. J.*, **85**, 161.

Cabrit, S. and Bertout, C. 1986, in *Protostars and Molecular Clouds, ed.* T. Montmerle and C. Bertout, Centre d'Etudes Nucléaires Saclay, pp. 43-56.

Castor, J.; McCray, R.; Weaver, R. 1975, *Ap. J.*, **300**, L107.

Clemens, D. P. 1985, *Ap. J.*, **259**, 422.

Cohen, M. *via* Bally, J. 1987, private communication.

Cox, D. P. 1972, *Ap. J.*, **178**, 159.

Dickman, R. L. 1979, *Ap. J. Suppl.*, **37**, 407.

Ezer, D. and Cameron, A. G. W. 1967, *Can. J. Phys.*, **45**, 3429.

Felli, M. and Harten, R. H. 1981, *Astr. Ap.*, **100**, 42.

Gunn, J. E.; Harris, F. J.; and Oke, J. B. 1987, *P.A.S.P.*, **99**, 616.

Henkel, C.; Haschick, A. D.; Güsten, R., 1986, *Astr. Ap.*, **165**, 197.

Königl, A. 1982, *Ap. J.*, **261**, 115.

Kutner, M. and Ulich, B. L. 1981, *Ap. J.*, **250**, 341.

Kwan, J. 1978, *Ap. J.*, **223**, 147.

Lada, C. 1985, *Ann. Revs. Astr. Ap.*, **23**, 267.

Leung, C. M. and Liszt, H. S. 1976, *Ap. J.*, **208**, 732.

Milman, A. S. 1977, *Ap. J.*, **211**, 128.

Mundy, L. G.; Scoville, N. Z.; Bååth, L. B.; Masson, C. R.; and Woody, D. P 1986, *Ap. J. Letts.*, **304**, L51.

Oke, J. B. and Gunn, J. E. 1983, *Ap. J.*, **266**, 713.

Panagia, N. 1973, *A. J.*, **78**, 929.

Panagia, N. and Felli, M. 1975, *Astron. Ap.*, **39**, 1.

Plambeck, R. L.; Wright, M. C. H.; Welch, W. J.; Bieging, J. H.; Baud, B.; Ho, P. T. P.; and Vogel, S. N. 1982, *Ap. J.*, **259**, 617.

Plambeck, R. L. and Wright, M. C. H. 1987, *Ap. J. Letts.*, **317**, L101.

Price, S. D. and Walker, R. G. 1976 *The AFGL Four-Color Infrared Sky Survey: Catalog of Observations at 4.2, 11.0, 19.8, and 27.4 μm.*

Scoville, N. Z.; Sargent, A. I.; Sanders, D. B.; Claussen, M. J.; Masson, C. R.; Lo, K. Y.; and Phillips, T. G. 1986, *Ap. J.*, **303**, 416.

Sharpless, S. 1959, *Ap. J. Suppl.*, **4**, 257.

Thompson, A. R.; Clark, B. G.; Wade, C. M.; Napier, P. J. 1980, *Ap. J. Suppl.*, **44**, 151.

Vogel, S. N.; Wright, M. C. H.; Plambeck, R. L.; and Welch, W. J. 1984, *Ap. J.*, **283**, 655.

Vogel, S. N.; Bieging, J. H.; Plambeck, R. L.; Welch, W. J.; and Wright, M. C. H. 1985, *Ap. J.*, **296**, 600.

Weaver, R.; McCray, R.; Castor, J.; Shapiro, P.; Moore, R. 1977, *Ap. J.*, **218**, 377.

Wright, A. E. and Barlow, M. J. 1975, *MNRAS*, **170**, 41.

Wright, M. C. H.; Plambeck, R. L.; Vogel, S. N.; Ho, P. T. P.; and Welch, W. J. 1983, *Ap. J. Letts.*, **267**, L41.

FIGURE CAPTIONS

Figure II.1a Gunn r band (λ = 6700 Å, $\Delta\lambda$ = 1000 Å) CCD frame of the S87 HII region (courtesy of Dr. James Schombert). North is up and east is to the left. The pixel size is 1.23″. The rectangular, black objects are stars. Two bright knots in the nebula, with peak brightnesses of 20.2 and 20.0 r magnitudes/arcsec^2, are marked A and B, respectively. Note the position of these features relative to the VLA contours of Figure II.1b. The lowest grey scale level is at 24.0 r magnitudes/arcsec^2. The sky was at 21.35 r magnitudes/arcsec^2.

Figure II.1b VLA 2cm D array contours of S87 overlaid on the Gunn r image of Figure II.1a. Contour levels are -1, 1, 1.4, 2, 2.8, 4, 5.6, 8, 11, 16, 22, 32, 44, 64, 89, 128, 178, and 256 times the rms noise level of 0.3 mJy/beam. Vertical lines are spaced every two seconds of time in right ascension; horizontal lines, every 15″ in declination. Note the lack of an optical counterpart to the VLA peak, indicating 35 magnitudes of visual extinction to the S87/IRS1.

Figure II.2a 5 GHz VLA B array image of S87. Contour levels are 1, 2, 3, 4, 5, 10, 15, 20, 30, 50, 70, and 100% of the peak flux of 22.37 mJy/beam.

Figure II.2b 15 GHz VLA C array image of S87. Contour levels are the same percentage of the 20.65 mJy/beam peak as in Figure II.2a.

Figure II.3a 5 GHz VLA A array map of the S87 core source. Contour levels are -2, 2, 4, 6, 12, 24, 48, and 96 times 0.79 mJy/beam. The peak flux is 4.93 mJy/beam. The beam

is shown in the lower right corner. The core source is resolved and appears isotropic.

Figure II.3b 15 GHz VLA B array map of the S87 core. Contour levels are the same as for Figure II.3a. The peak flux in this map is 6.39 mJy/beam. The beam appears in the lower, right-hand corner. Again, the core source is resolved.

Figure II.4 IRAS Survey Coadd Intensity maps of the S87 molecular cloud at 12 μm, 25 μm, 60 μm, and 100 μm. Contour level units are W m^{-2} sr^{-1}. Negative contour levels are indicated by dashed lines, and are due to overcorrection by the background level subtraction routine. Positive contour levels are at 3.0, 6.0, 9.0, 12.0, 15.0, 20.0, 28.3, 40.0, 56.6, 80.0, 113.1, 160.0, 226.3, 320.0, 452.5, 639.9, 905.0, 1279.8, 1810.0, 2559.6, 3619.9, 5119.2, 7239.6, 10238.2, 14478.8, and 20476.0. Peak contour levels are at 905.0, 5119.2, 20476.0, and 1279.8 W m^{-2} sr^{-1}, at 12 μm, 25 μm, 60 μm, and 100 μm, respectively.

Figure II.5 Azimuthally averaged radial intensity profiles of the IRAS maps of Figure II.4. Note the monotonic decrease in emission strength at all bands with increasing distance from S87/IRS1, indicating that IRS1 is the dominant heat source in this cloud. Error bars on selected data points represent the typical errors to be associated with each point. A plot of the intensity profile for an r^{-3} dependence is depicted by the solid line in the upper, right-hand corner. The agreement of the data with this slope indicates an r^{-2} dust volume density distribution, as discussed in the text.

Figure II.6 Energy distribution of S87/IRS 1. Open squares are from Bally 1981 (12″ aperture), open circles are IRAS points, open diamonds are submillimeter points (10″

and 17″ beams at 400 μm and 700 μm, respectively), from the Caltech Submillimeter Observatory, courtesy of J. Keene. The millimeter point (6.8″ × 6.5″ synthesized beam) is from the OVRO millimeter-wave array. Open triangles are the centimeter points from the VLA, integrated over the entire emission region associated with IRS 1, while the filled triangles are the VLA fluxes centered on IRS1, but integrated only over an OVRO beam area.

Figure II.7 Optical spectrum of the S87 nebula taken with the 30″ long, north-south slit passing through the VLA peak position at $\alpha_{1950} = 19^h44^1 3.7^s, \delta_{1950} = 24°28'05.1''$. Lines marked NS are night-sky neon emission. Unfortunately, the nebular 6717 Å[SII] line was contaminated by the night-sky emission, preempting a density determination from the [SII] 6717/6731 line ratio. Note the asymmetric shapes of the nebular lines, however.

Figure II.8 A blowup of the Hα line profile shows that all the observable emission in this line is blue-shifted with respect to the cloud's rest velocity, which is at V_{LSR} = 22 km s^{-1}, and that the S87 HII region must be associated with the molecular cloud. This line (along with the other nebular lines of Figure II.7) is asymmetric because the red-shifted, ionized wind component is obscured by the intervening cloud core.

Figure II.9a FCRAO map of peak CO antenna brightness temperature (T_{R_*}) in the S87 cloud core. The map peak is at 34 K, with contours decreasing by increments of 2 K from the peak. Map center coordinates (0,0) correspond to the VLA peak position of S87/IRS1 ($\alpha_{1950} = 19^h44^1 3.7^s, \delta_{1950} = 24°28'05.1''$. All offsets are in minutes of arc from this position.

Figure II.9b FCRAO map of the integrated ^{13}CO column density in the S87 field. The

peak contour level is at $N_{^{13}CO} = 8.64 \times 10^{16}$ cm^{-2}. Contour levels decrease from the peak value by increments of 1.23×10^{16} cm^{-2}. The coordinate system is the same as for Figure II.9a.

Figure II.9c Blue-shifted (18 → 20 km s^{-1}) and red-shifted (24 → 26 km s^{-1}) ^{13}CO emission in S87 mapped with the FCRAO 14 m antenna. Blue-shifted gas is indicated by the dashed contours, and red-shifted gas by the solid contours. Solid contour levels are 2, 4, 6, 8, 10, 12, and 14°K km s^{-1}. Dashed contour levels are 0.5, 1, 1.5, 2, 2.5, 3, and 3.5°K km s^{-1}. The coordinate system is as for Figure II.9a.

Figure II.9d VLA 2 cm D array map of S87, presented here for ease of comparison with the previous single dish millimeter line maps of this figure. Contour levels are at -1.0, 1.0, 1.4, 2.0, 2.8, 4.0, 5.6, 8.0, 11.0, 16.0, 22.0, 32.0, 44.0, and 64.0 times the 3σ rms noise level of 0.3 mJy/beam. The peak flux in this map is 31 mJy/beam. The coordinate system is as for Figure II.9a.

Figure II.10 CO (top panel) and ^{13}CO (bottom panel) line profiles from FCRAO at three positions in S87. The leftmost profiles are at a position offset one arcminute east and one arcminute north of the VLA peak, the center profiles are from the VLA peak position, and the rightmost profiles from a position offset one arcminute west and one arcminute south from the VLA peak. All vertical axis units are brightness temperature (T_R^*) in °K. Horizontal axis units are V_{LSR} in km s^{-1}.

Figure II.11 Overlay of OVRO (Owens Valley Radio Observatory) millimeter interferometer map of CS (J = 2→1) line emission on 6 cm VLA radio continuum map of S87. The

contour increment is 2 (Jy km s^{-1})/beam. The blue-peak value is 13.2 (Jy km/s)/beam, while the red-peak value is 10.1 (Jy km/s)/beam.

Figure II.12a OVRO map of red-shifted ^{13}CO emission in S87 covering the range 23.3 km $s^{-1} \leq V_{LSR} \leq$ 24.1 km s^{-1}. Contours are at 10% intervals of 6.77 (Jy km/s)/beam.

Figure II.12b OVRO map of ^{13}CO emission in S87 covering the velocity range 22.1 km $s^{-1} \leq V_{LSR} \leq$ 23.3 km s^{-1}. Contour levels are 10% of 8.28 (Jy km/s)/beam.

Figure II.12c OVRO map of ^{13}CO emission in S87 covering the velocity range 20.6 km $s^{-1} \leq V_{LSR} \leq$ 21.7 km s^{-1}. Contour levels are 10% of 6.45 (Jy km/s)/beam.

Figure II.12d OVRO map of the blue-shifted ^{13}CO emission in S87 covering the velocity range 19.7 km $s^{-1} \leq V_{LSR} \leq$ 20.3 km s^{-1}. Contour levels are 10% of 4.8 (Jy km/s)/beam.

Figure II.13a Interferometer and single-dish line profiles of the ^{13}CO (J=1→0) emission at the position of the CS blue-shifted emission peak ($\alpha_{1950} = 19^h\ 44^m\ 12.9^s$, $\delta_{1950} = 24°\ 27'\ 53.1''$.)

Figure II.13b Interferometer and single-dish line profiles of the ^{13}CO (J=1→0) emission at the VLA peak position ($\alpha_{1950} = 19^h\ 44^m\ 13.7^s$, $\delta_{1950} = 24°\ 28'\ 05.1''$.)

Figure II.13c Interferometer and single-dish line profiles of the ^{13}CO (J = 1→0) emission at the position of the red-shifted CS emission peak ($\alpha_{1950} = 19^h\ 44^m\ 14.1^s$, $\delta_{1950} = 24°\ 28'\ 12.2''$.)

Negative values are due to missing, zero-spacing flux. Single-dish data are indicated by the dashed lines; interferometer data, by the solid lines. Note that the interferometer

recovers all the single-dish flux from compact structures in the source, but is insensitive to flux from large-scale features, which are detected by the single-dish measurements. Thus, this figure provides striking evidence for large-scale, red-shifted gas at the position of the compact, blue-shifted peak and for large-scale, blue-shifted gas at the position of the compact, red-shifted peak.

Figure II.14 V(r) diagram of ^{13}CO emission. Solid diamonds are data points from the OVRO interferometer; open diamonds represent FCRAO data. The vertical axis is the V_{LSR} value of the peak emission at the given position. The horizontal axis is the projected distance of the peak emission from the VLA core position, which would have coordinates (0pc, 23 km s^{-1}) in this figure. The dashed curve represents the locus of points that gravitationally bound gas would follow for an assumed 21 $M_\odot$ central mass. Any infall or centrifugally balanced, gravitationally bound rotational motions would not differ qualitatively from the dashed curve, if a central mass dominated the gas dynamics. Other possibilities are discussed in the text. The slope of the straight line fit yields a dynamical time scale of 5.4 $\times$ 10^4 years for the S87 outflow.

Figure II.15a Cartoon representation of the geometry of the S87 molecular outflow (adopted from Cabrit and Bertout 1986). The arrow points toward the observer. In this model, the inclination angle i is smaller than the cone opening angle. The regions of the cone marked by dashed lines would appear as red-shifted gas to the observer, while those parts of the cone indicated by solid lines would appear blue-shifted.

Figure II.15b Synthetic contour map of blue-shifted (solid lines) and red-shifted (dashed lines) CO J = 1 $\rightarrow$ 0 integrated intensity for the geometry of Figure II.15a. Note the compact, blue-shifted emission embedded in large-scale, red-shifted emission, and compact,

red-shifted emission superposed on large-scale, blue-shifted emission – in agreement with the data for S87 presented in Figure II.13.

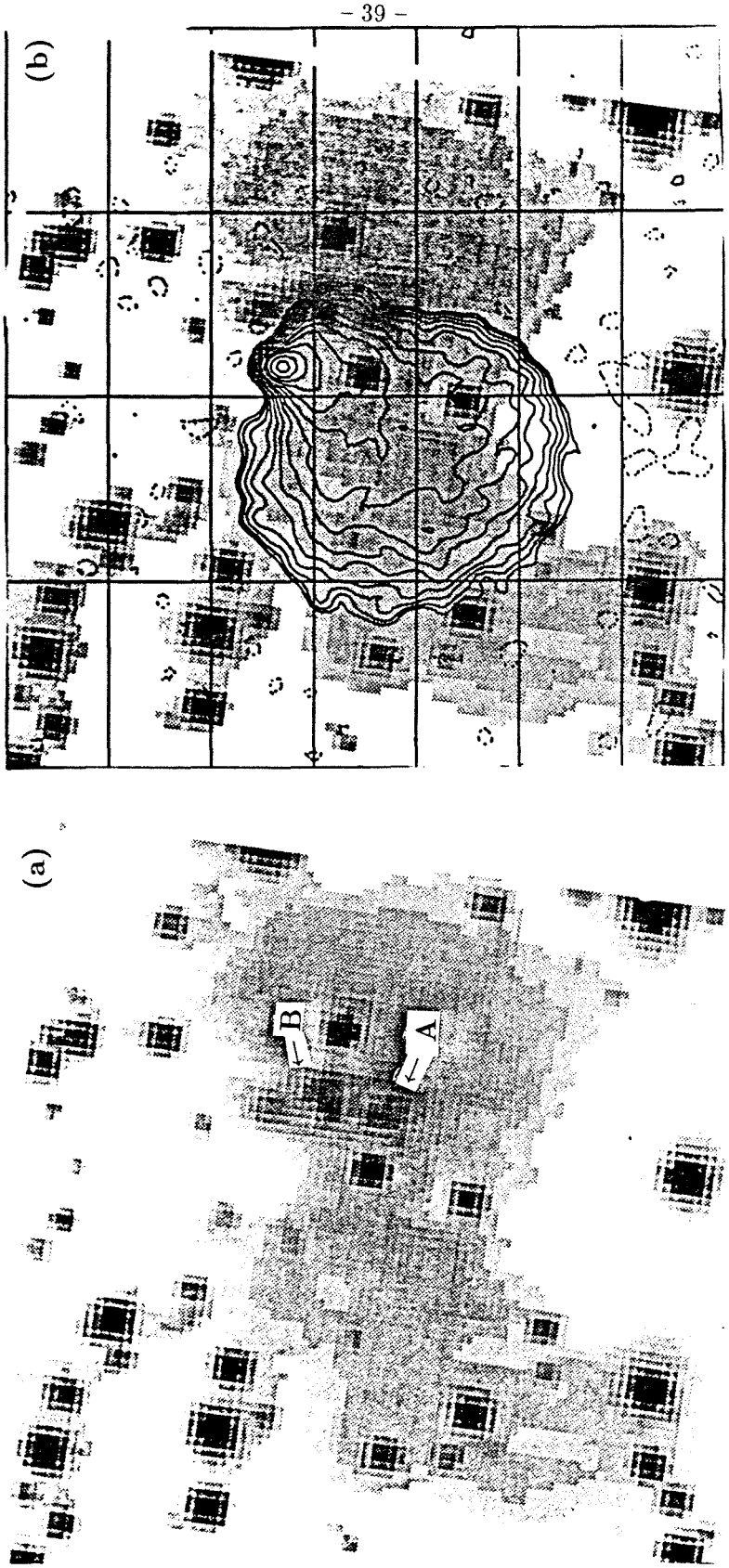

Figure II.1

Figure II.2

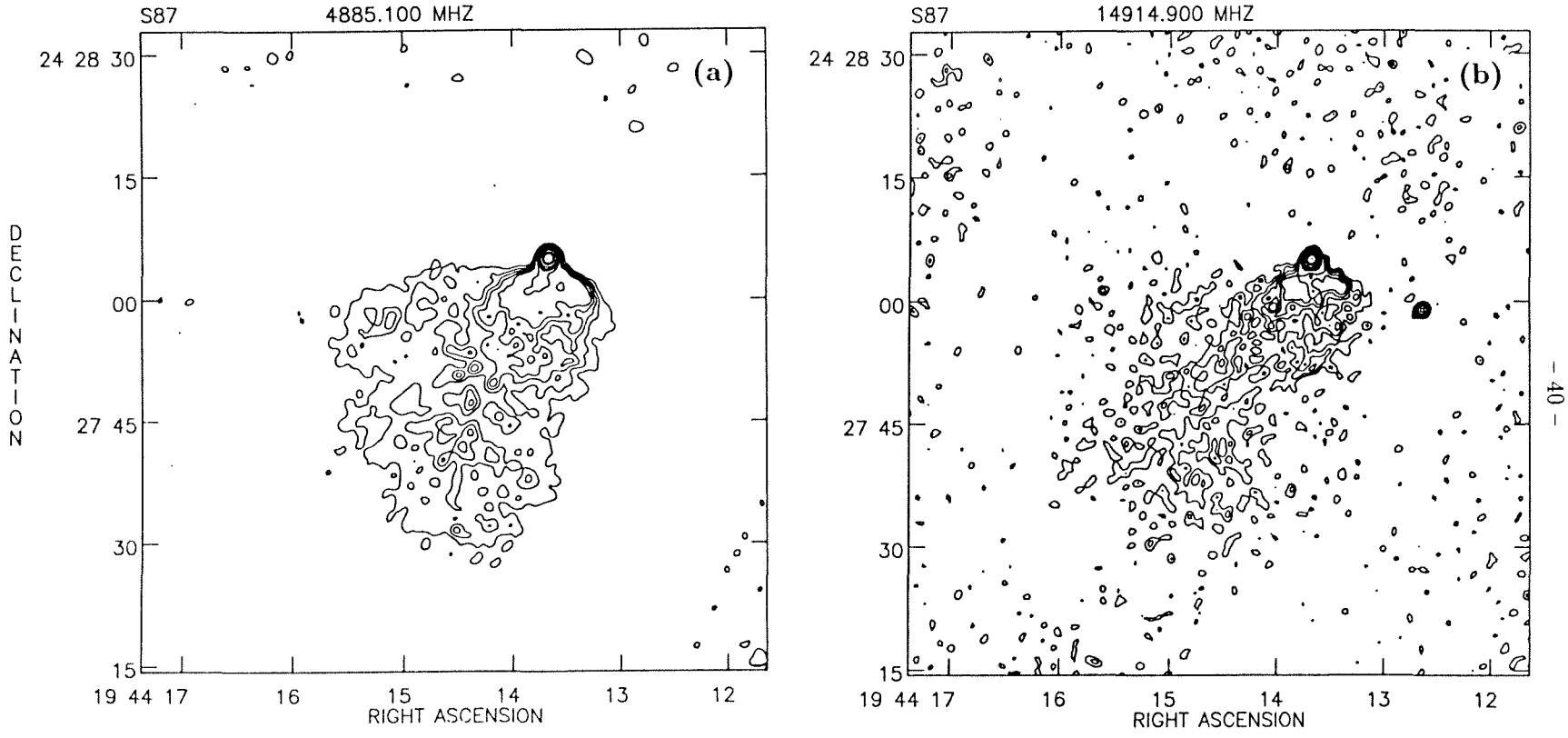
S87
4885.100 MHZ
(a)
24 28 30
15
00
27 45
30
15
DECLINATION
19 44 17
16
15
14
13
12
RIGHT ASCENSION
S87
14914.900 MHZ
(b)
24 28 30
15
00
27 45
30
15
19 44 17
16
15
14
13
12
RIGHT ASCENSION

Figure II.3

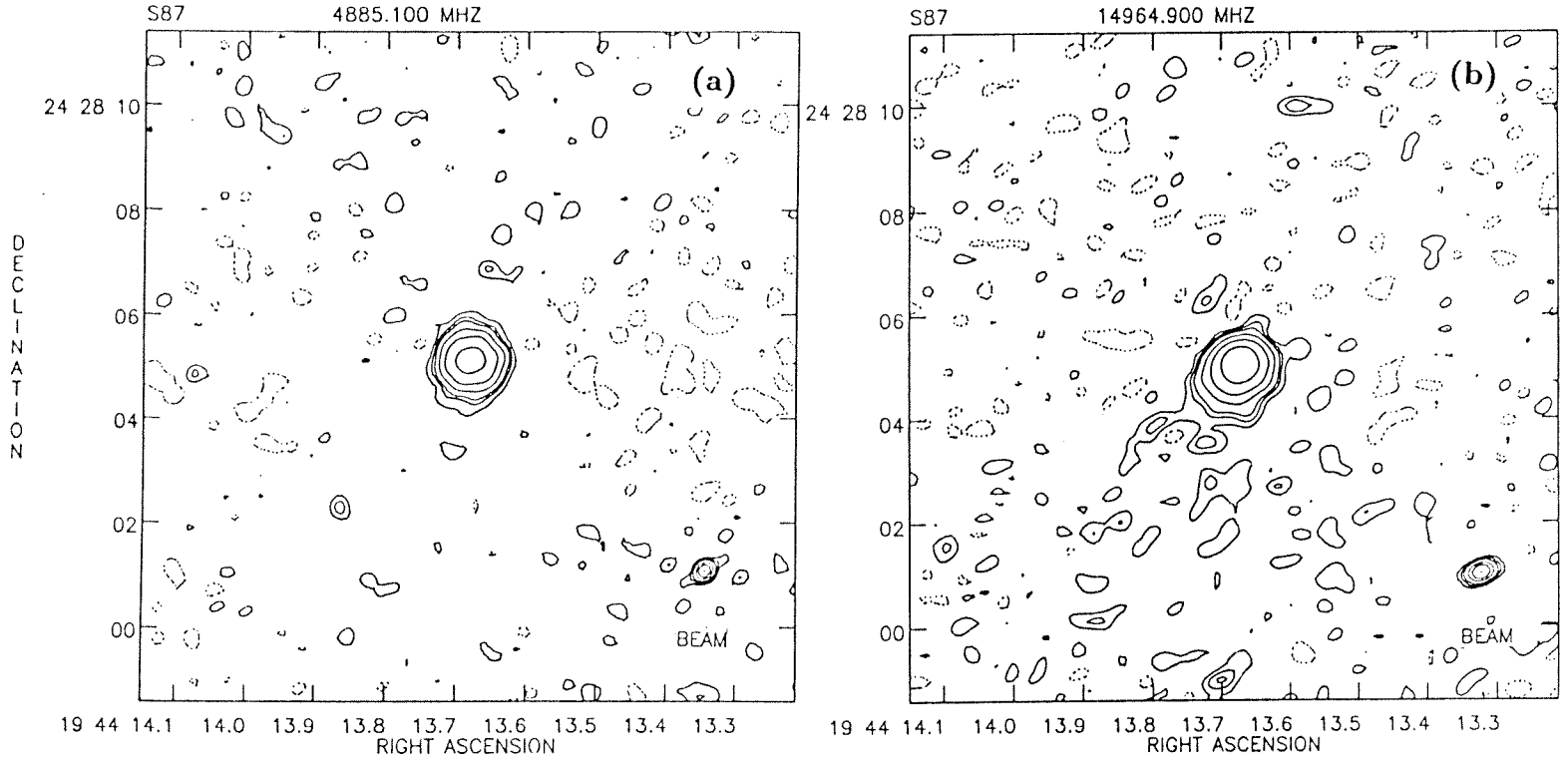
S87
4885.100 MHZ
(a)
24 28 10
08
06
04
02
00
DECLINATION
BEAM
19 44 14.1 14.0 13.9 13.8 13.7 13.6 13.5 13.4 13.3
RIGHT ASCENSION
S87
14964.900 MHZ
(b)
24 28 10
08
06
04
02
00
BEAM
19 44 14.1 14.0 13.9 13.8 13.7 13.6 13.5 13.4 13.3
RIGHT ASCENSION

S87

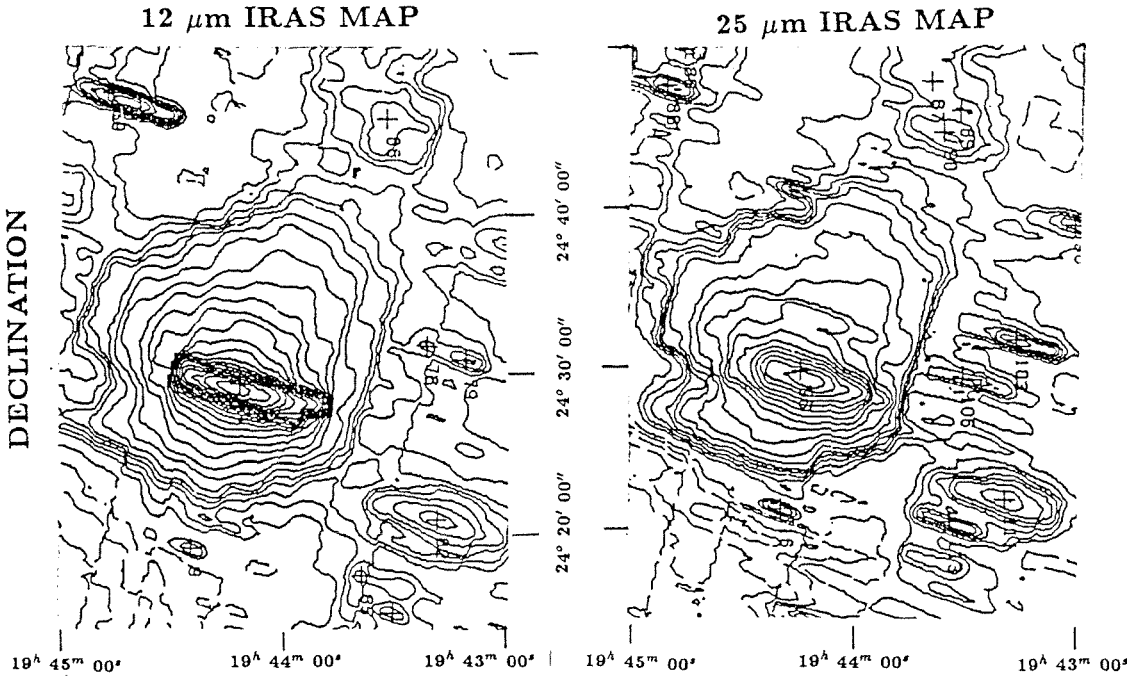

Figure II.4

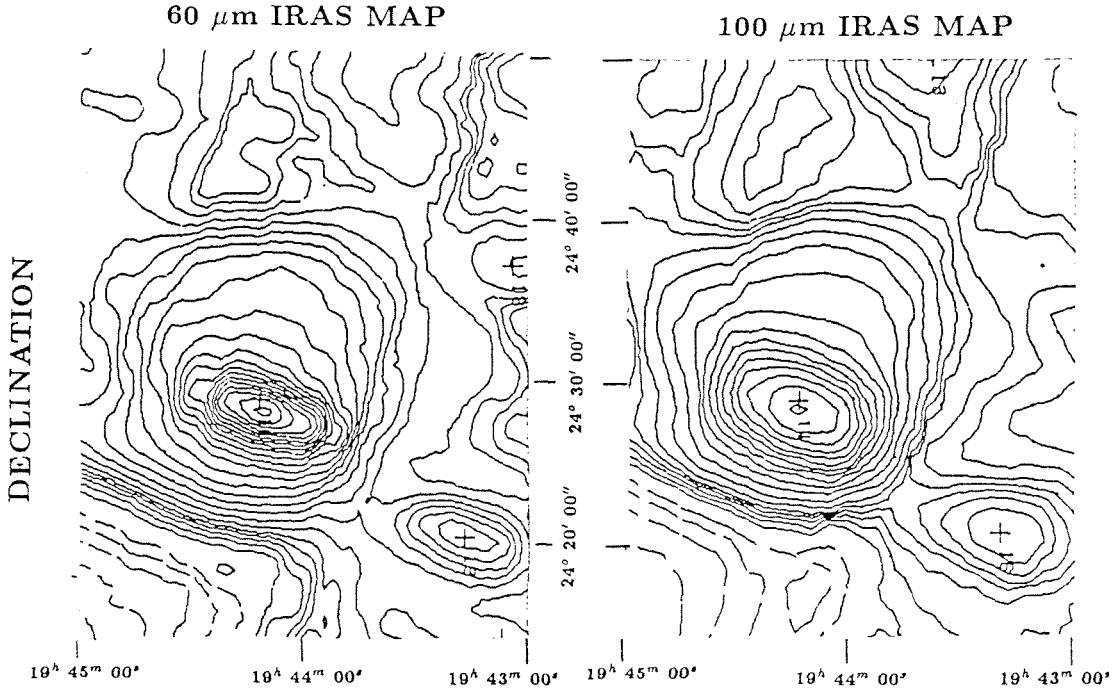

Figure II.5 RADIAL PROFILE OF DUST EMISSION INTENSITY

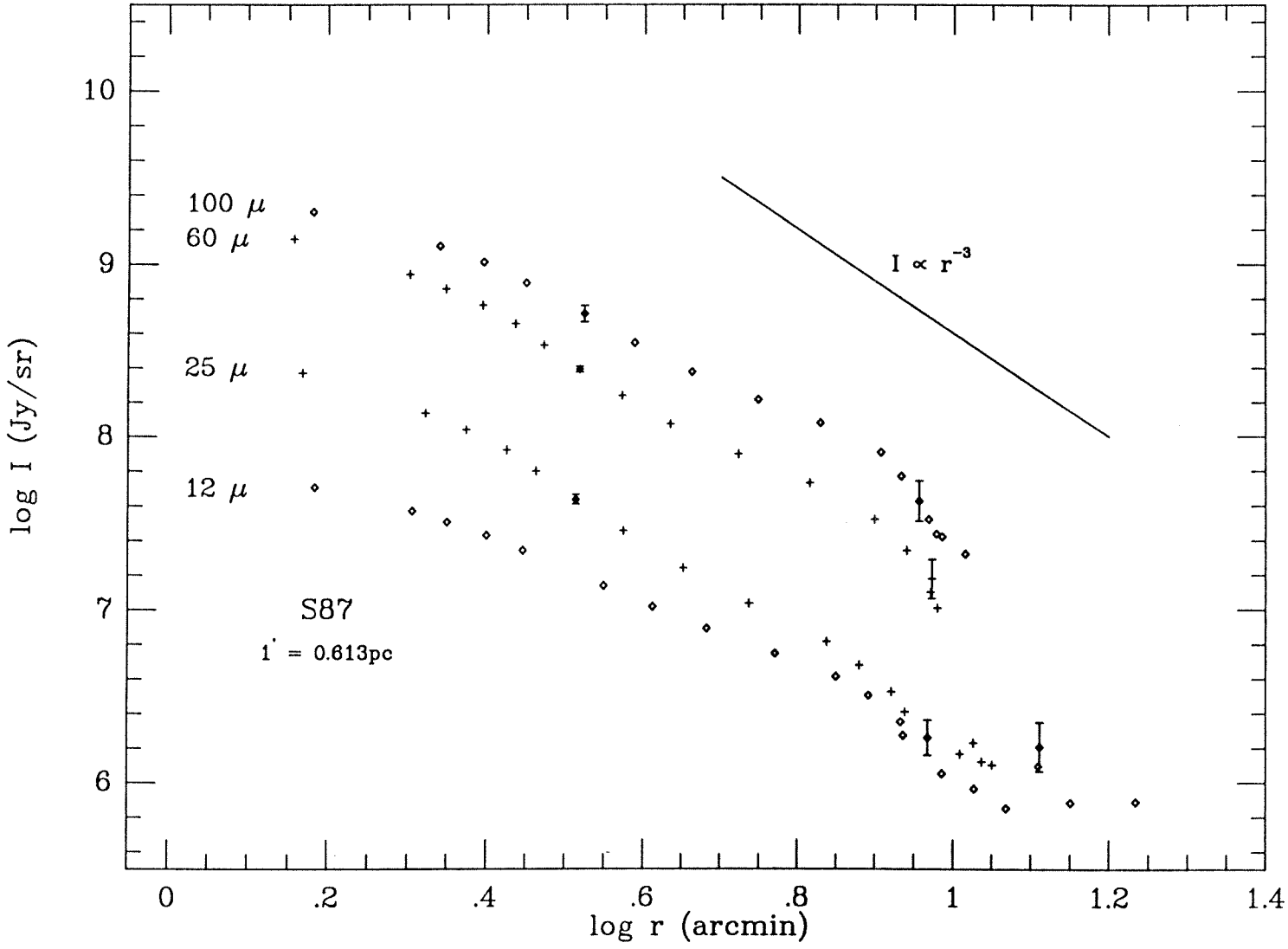

Figure II.6

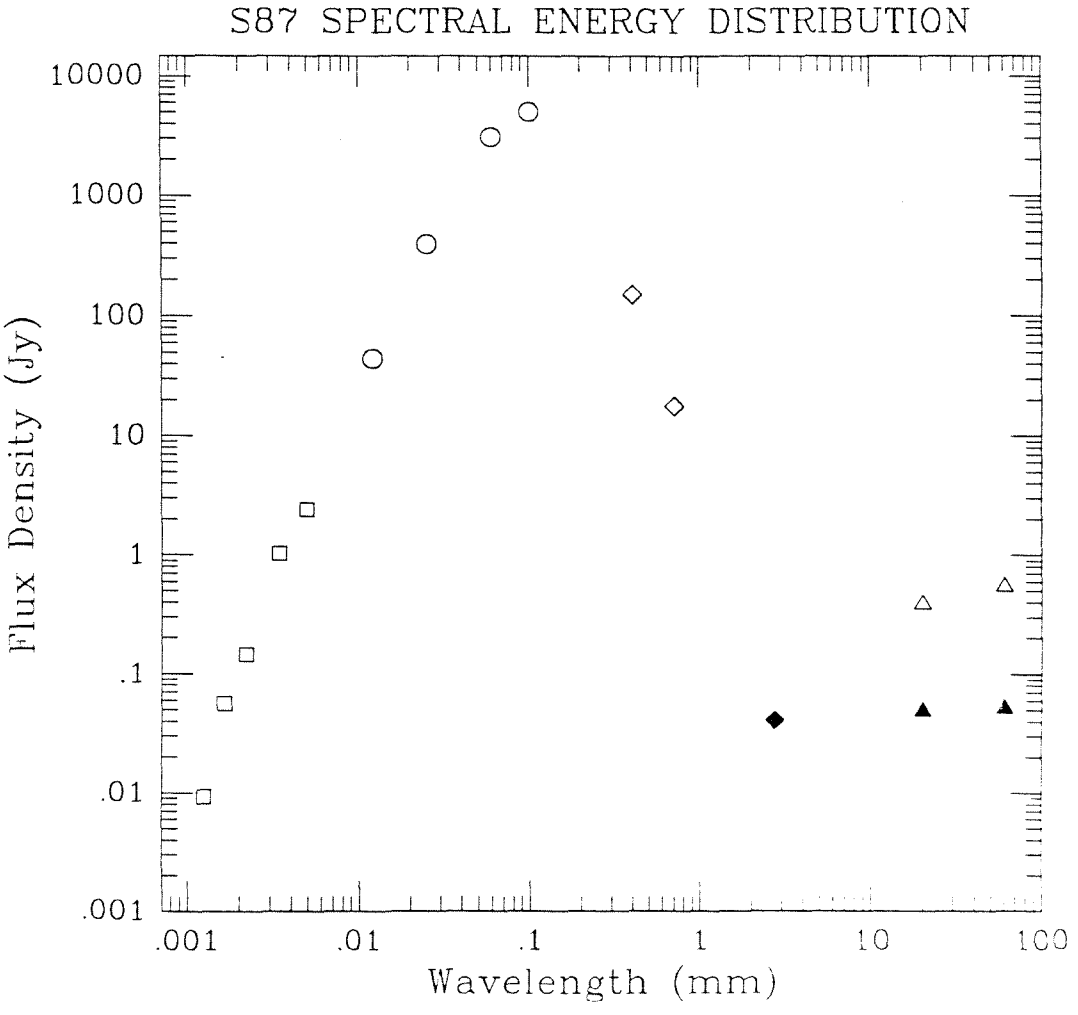
S87 SPECTRAL ENERGY DISTRIBUTION
Flux Density (Jy)
10000
1000
100
10
1
.1
.01
.001
.001
.01
.1
1
10
100
Wavelength (mm)

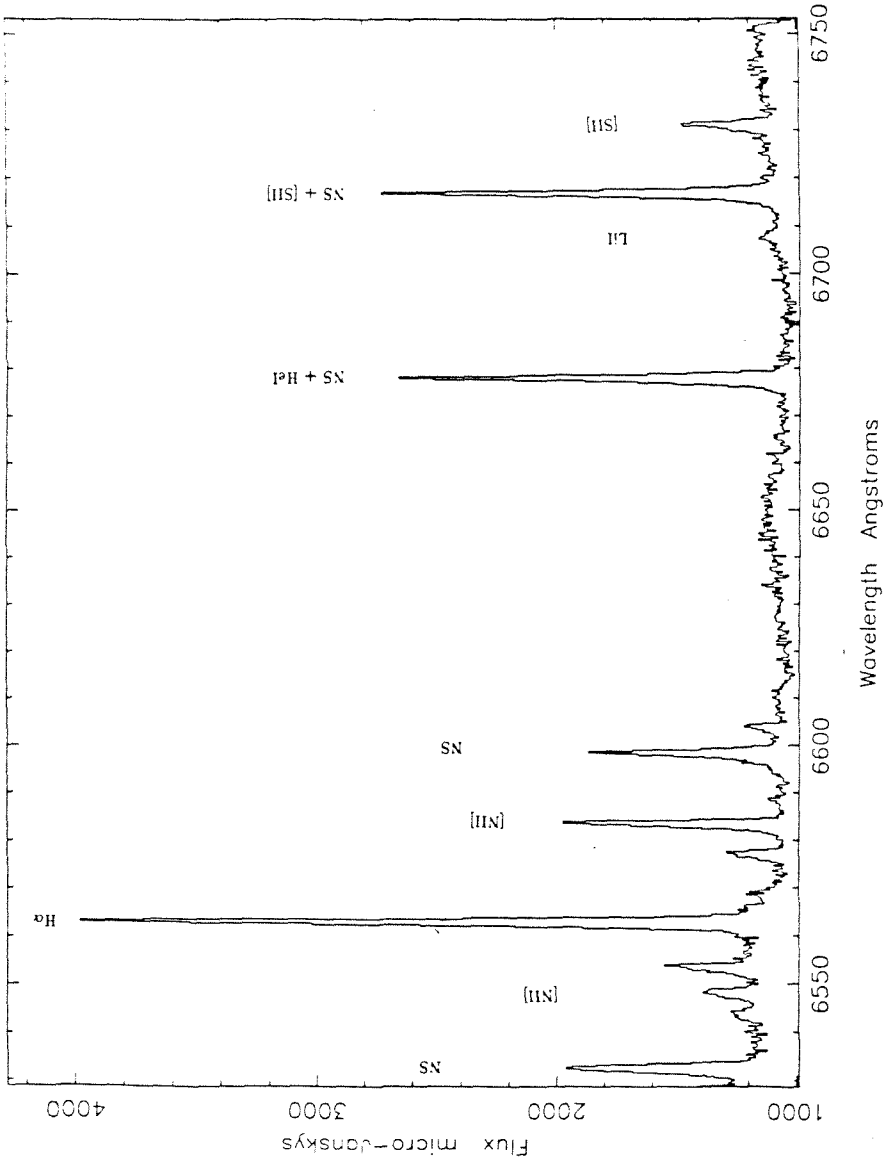

Figure II.7

S87

Figure II.8

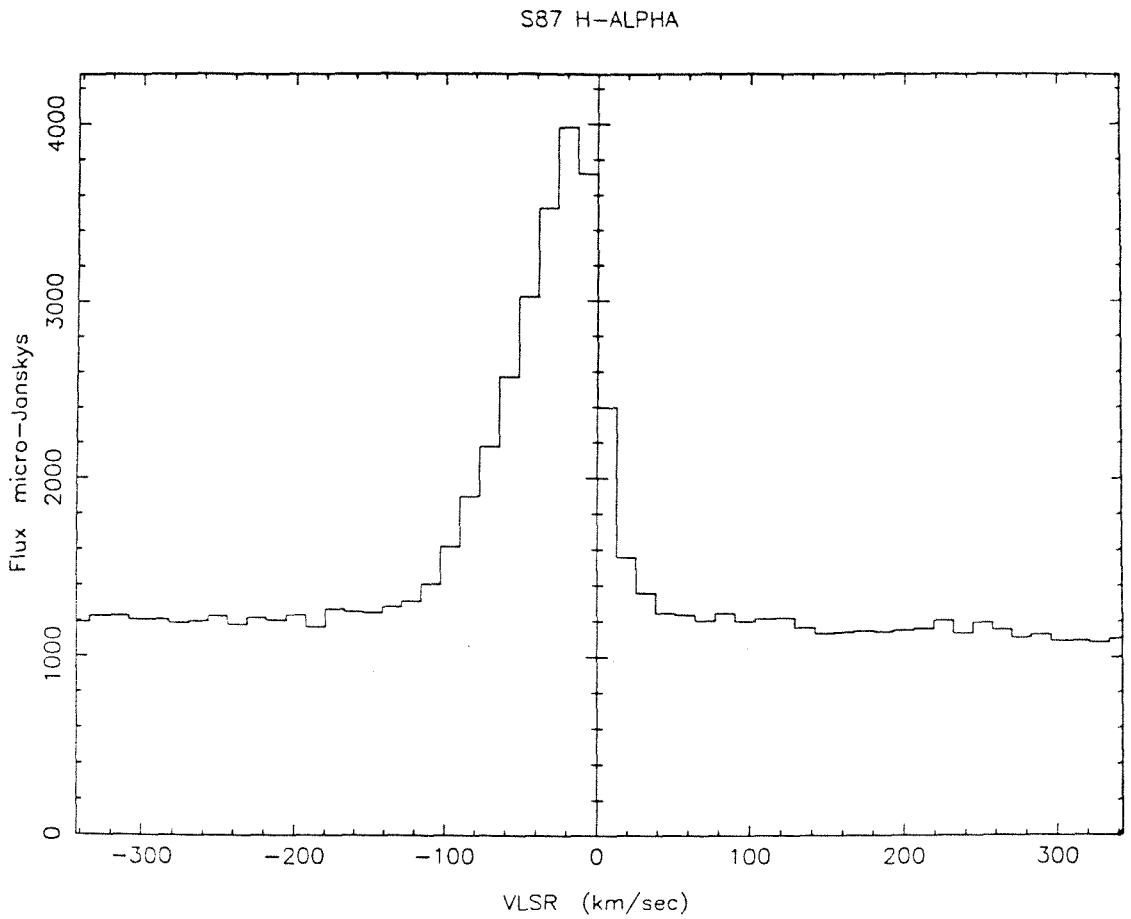
S87 H–ALPHA
Flux micro–Janskys
0
1000
2000
3000
4000
–300
–200
–100
0
100
200
300
VLSR (km/sec)

Figure II.9

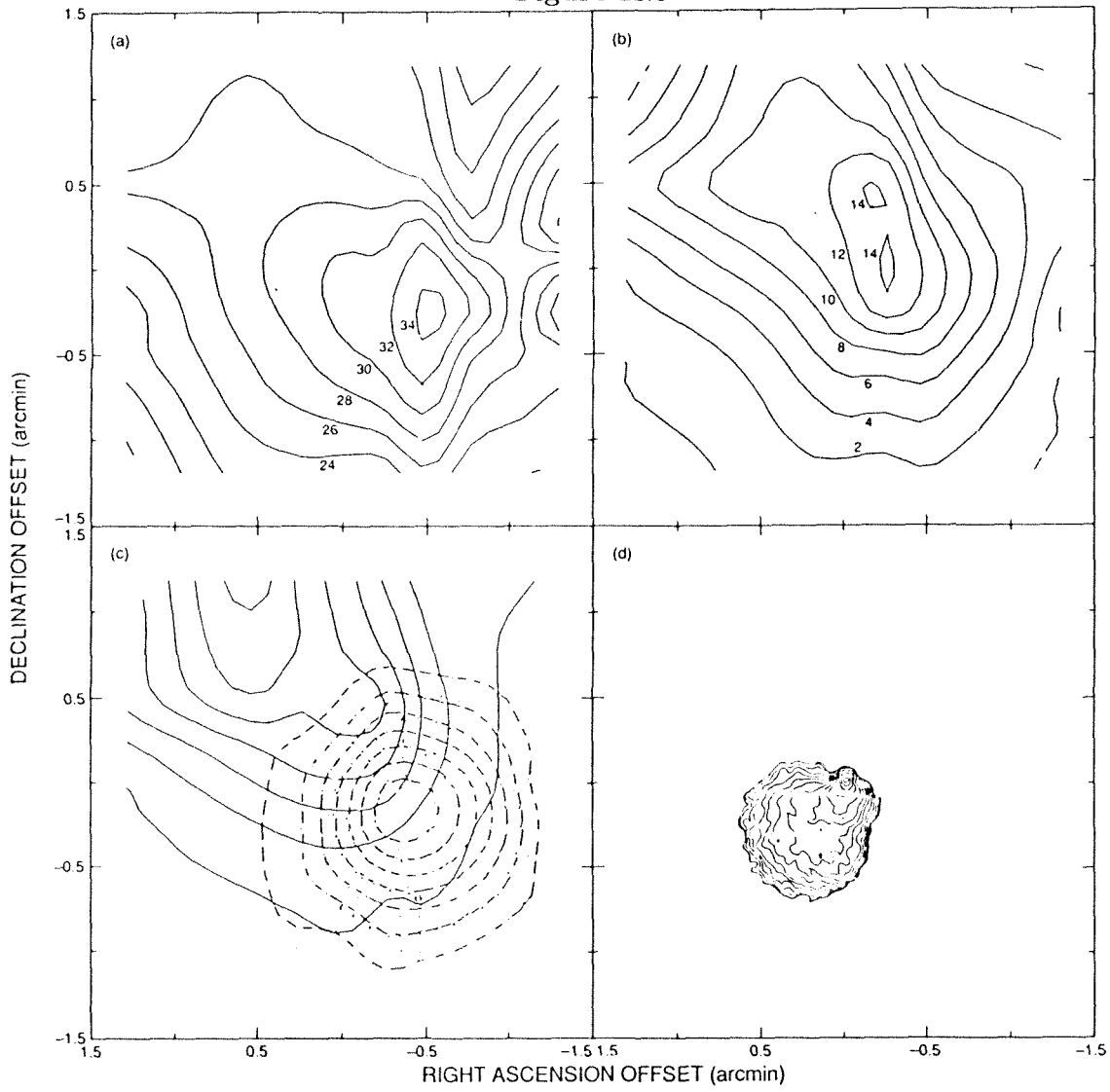
(a)
(b)
(c)
(d)
34
32
30
28
26
24
14
12
14
10
8
6
4
2
1.5
0.5
−0.5
−1.5
DECLINATION OFFSET (arcmin)
RIGHT ASCENSION OFFSET (arcmin)

Figure II.10

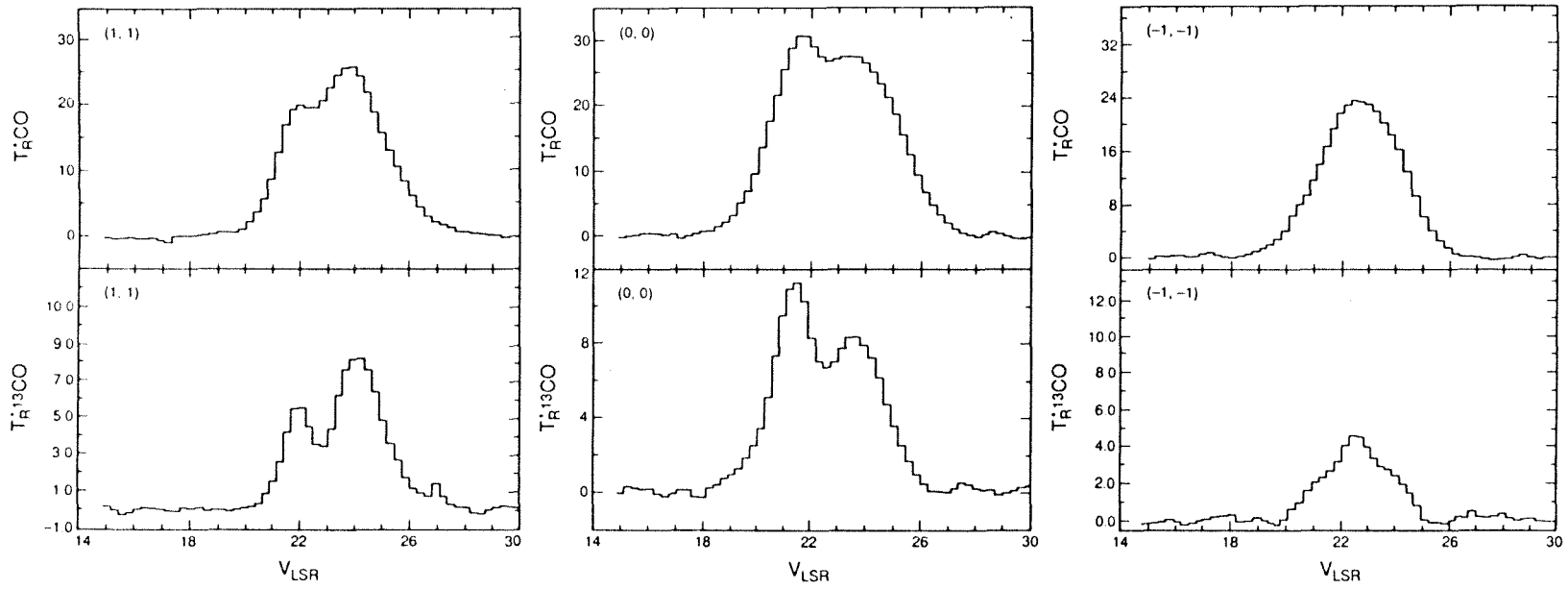

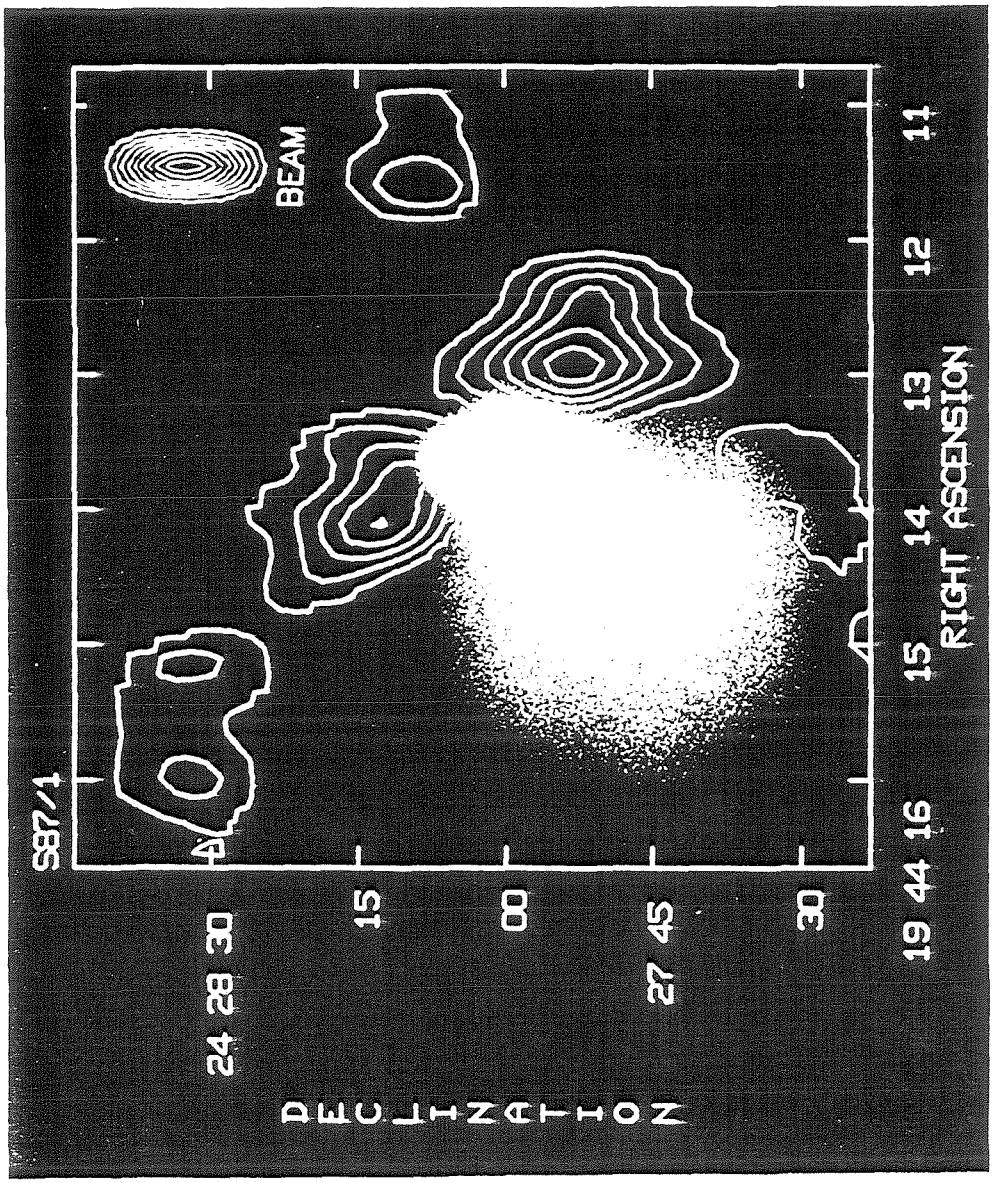
SS71
BEAM
DECLINATION
24 28 30
15
00
27 45
30
19 44 16
15
14
13
12
11
RIGHT ASCENSION

Figure II.11

Figure II.12

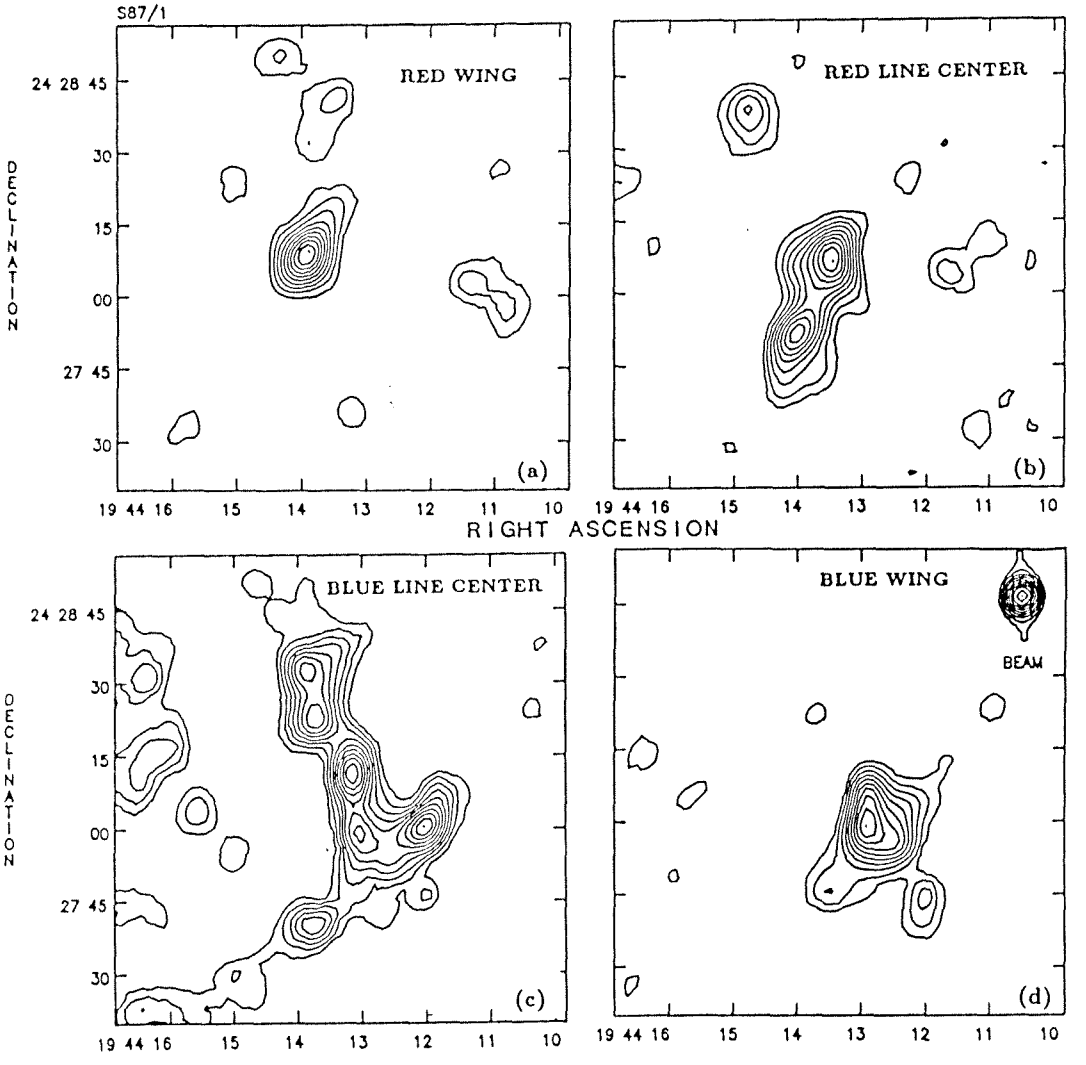
S87/1
RED WING
RED LINE CENTER
BLUE LINE CENTER
BLUE WING
BEAM
(a)
(b)
(c)
(d)
DECLINATION
RIGHT ASCENSION
24 28 45
30
15
00
27 45
30
19 44 16
15
14
13
12
11
10

Figure II.13

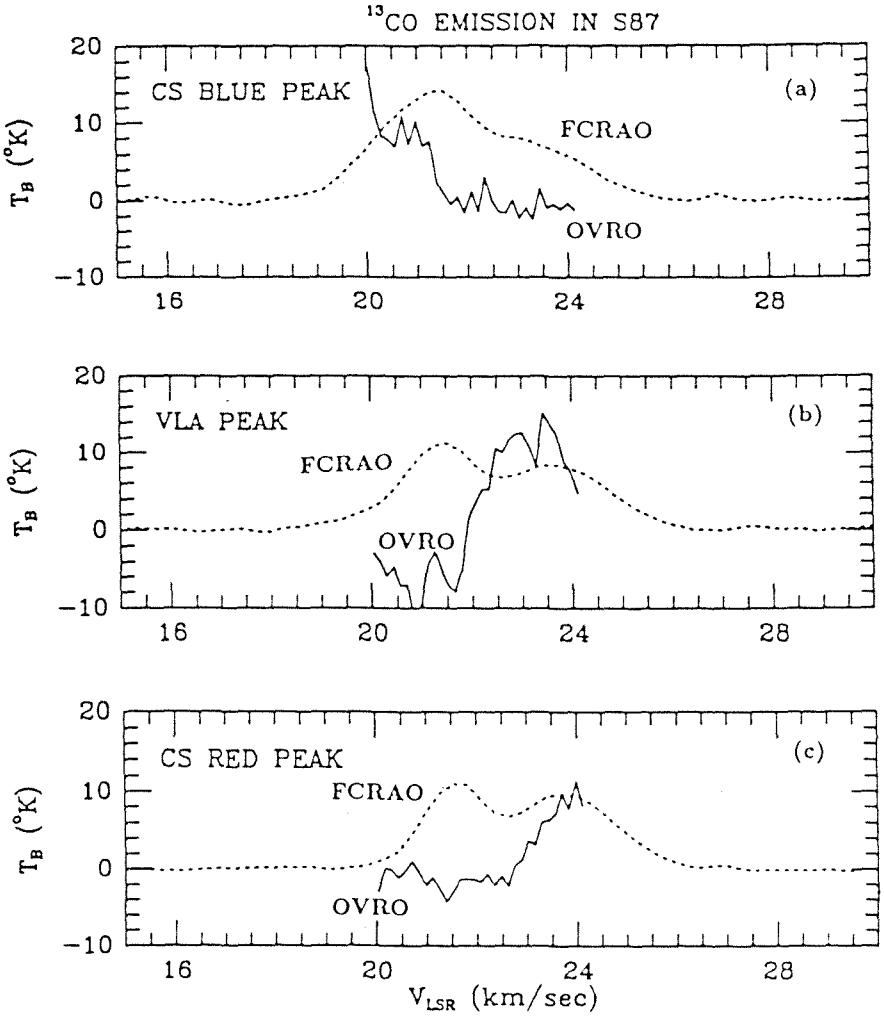
^{13}CO EMISSION IN S87
CS BLUE PEAK
(a)
FCRAO
OVRO
VLA PEAK
(b)
FCRAO
OVRO
CS RED PEAK
(c)
FCRAO
OVRO
T_B (°K)
20
10
0
−10
16
20
24
28
V_{LSR} (km/sec)

Figure II.14

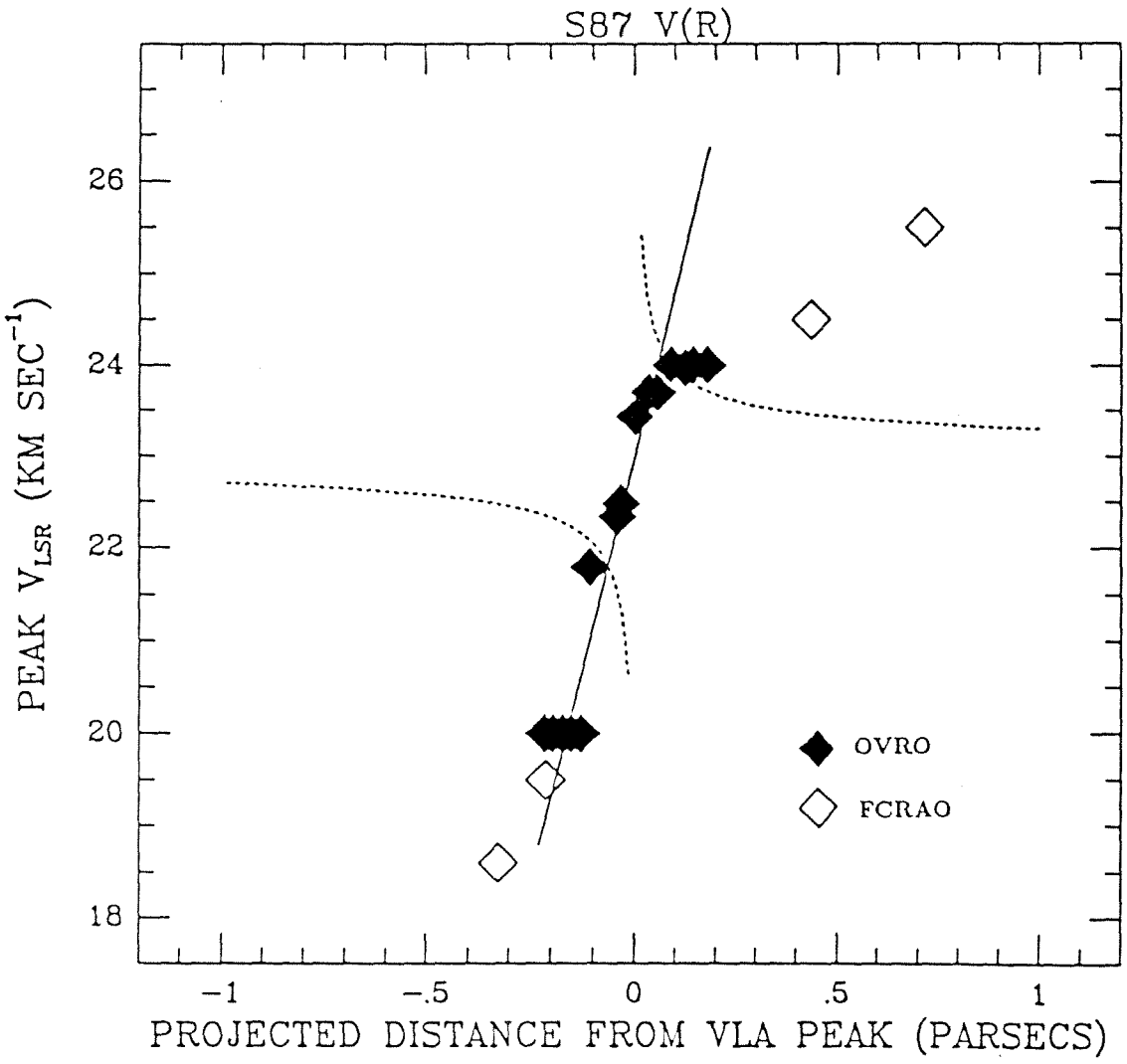
S87 V(R)
PEAK V_{LSR} (KM SEC^{-1})
26
24
22
20
18
−1
−.5
0
.5
1
PROJECTED DISTANCE FROM VLA PEAK (PARSECS)
OVRO
FCRAO

Figure II.15

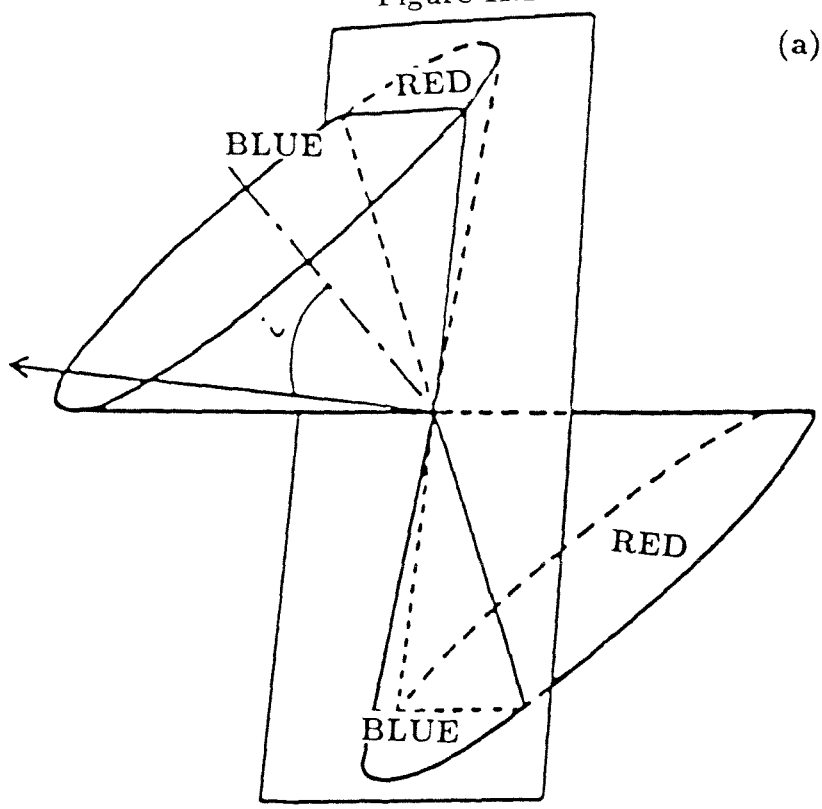

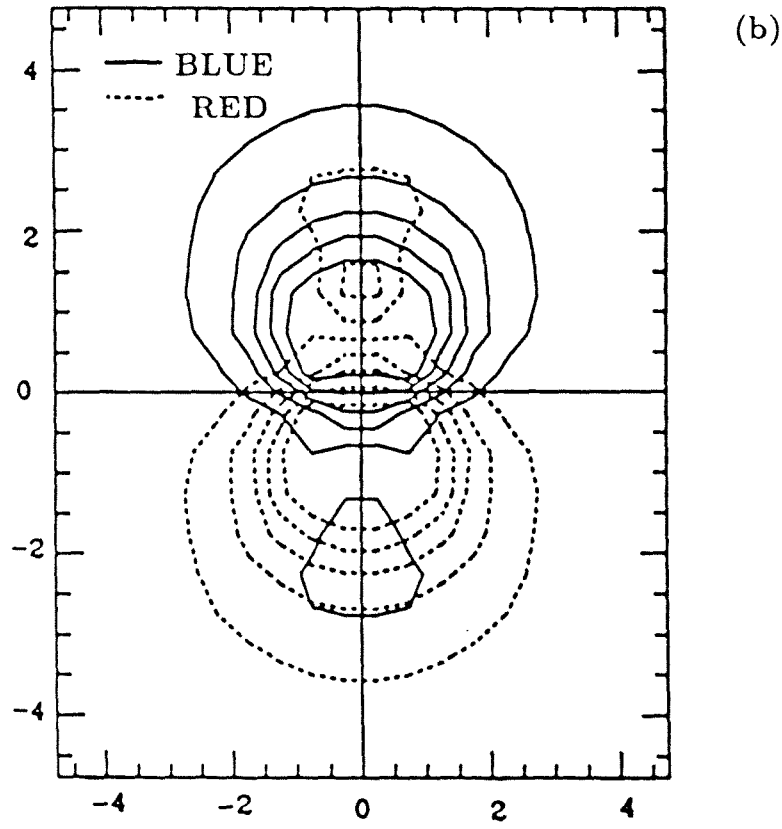

III. LkHα101

III. A. INTRODUCTION

It is a well-known, observational fact of millimeter-wave astronomy that molecular cloud linewidths are highly supersonic. Among the suggestions for explaining the surprisingly large linewidths are cloud collapse, turbulent motions, rotation, or outflowing gas. Claims of large-scale cloud rotation have been shown to be premature upon subsequent closer inspection of the same clouds at higher spatial resolution. Similarly, there is no unequivocal example of a molecular cloud currently collapsing. Recent surveys of small regions of molecular clouds, centered on active, star-forming regions, have led to the discovery of supersonic molecular outflows. LkHα101 is one of the pre-main-sequence objects searched for signs of a molecular outflow. However, the results for LkHα101 turned out to be ambiguous, such that no *clear* case for a molecular outflow could be made in this source (Bally and Lada 1983). The unprecedentedly high spatial resolution recently made available with the advent of millimeter-wave interferometry has provided the impetus to examine this source further.

At a distance of 800 pc, LkHα101 is a massive, luminous (1.1×10^4 $L_\odot$), pre-main-sequence star, a member of the class of "Herbig Be stars." The three defining characteristics of this class are: spectral type earlier than A, location in a region of high obscuration, and association with bright nebulosity (Herbig 1960). LkHα101 lies in a molecular cloud, and is seen through 9 magnitudes of visual extinction. It excites an associated reflection nebula, NGC 1579, and HII region, S222 (Herbig 1956). The directions of the optical polarization vectors in the reflection nebula, NGC 1579, indicate that LkHα101 is the only significant source of illumination, despite the presence of several nearby embedded T Tauri stars (Redman *et al.* 1986; Becker and White 1988).

The visual extinction in this area is greater than 1 magnitude over a region almost one

degree across and several degrees in declination. Large-scale CO mapping of this region reveals emission at all observed positions over a $23' \times 24'$ area. Molecular line emission over an area coextensive with the visual extinction is inferred (Christie *et al.* 1982) and IRAS data reveal the extent of 100 μm emission in the region to be $33'$ east-west by $40'$ north-south. HI mapping over a $31' \times 31'$ area indicates the presence of approximately 85 $M_\odot$ of atomic hydrogen with an absorption component near 1 km s^{-1} V_{LSR}, which may be due to an HI shell on the near side of the associated dark cloud. The HI column density distribution can be explained by an equilibrium dissociation model in which H_2 is formed on grains and is dissociated by the UV radiation field of LkHα 101. In order to explain the asymmetry of the HI column density distribution, LkHα 101 must be locally embedded in gas of high density in which there is an opening permitting dissociating photons to escape further on the low-density side. The atomic and molecular gas have not mixed, since the 21 cm linewidths are consistently twice as wide as the molecular linewidths in the same directions (Dewdney and Roger 1982). Thus, in the HI region, the molecular gas must exist as clumps or cloudlets (see below).

The near-infrared spectrum of LkHα101 contains bright hydrogen- and helium-emission lines, as well as emission lines of MgII and [FeII]. Two distinct emitting regions (both smaller than $3.75''$ in size) contribute to the observed spectra (Simon and Cassar 1984): i) a lower-density ($n_e < 10^6$ cm^{-3}), outer circumstellar envelope from which the narrow ($\Delta v = 40$ km s^{-1}) Brackett line and [FeII] emission originate, and ii) a high-density ($n_e > 10^6$ cm^{-3}), inner region responsible for the MgII emission and the broad (> 300 km s^{-1}), low-intensity HeI and Brγ line components. These authors note that if LkHα101 were completely surrounded by an ionization-bounded circumstellar envelope, no Lyman continuum photons could escape to ionize the outlying HII region. Based on the radio and hydrogen Brackett and Paschen line emissions of the core component ($< 1''$ diame-

ter), the excitation conditions in the ionized gas core are markedly different from those in the surrounding HII region ($\approx 1'$ in extent). To account for the observed ionization of the core by Lyman continuum photoionizations alone would require 100 times greater luminosity in the UV than could be provided by the embedded B0.5 ZAMS star (Harris 1976; Thompson *et al.* 1976). Therefore, other ionization mechanisms, such as ionization by collisions or by Balmer continuum photons, are at work. In fact, the OI line intensities in this source imply that Hα is optically thick (Thompson *et al.* 1976). Thus, the simultaneous presence of a circumstellar envelope that is ionized by collisions or by Balmer continuum photons *and* an HII region that is ionized by the same star is "*prima facie evidence for anisotropic flows near the central star.*" (Simon and Cassar 1984).

According to a recent spectroscopic study, virtually all Herbig Be stars (such as LkHα101) show Hα in emission, with velocity extents greater than 150 km s^{-1} FWHM (Finkenzeller and Mundt 1984). The Hα emission, in conjunction with detectable radio emission, is interpreted as originating from powerful stellar winds in these stars. Radio continuum observations of LkHα101 have been made at both high- and low-spatial resolution with the VLA. These data indicate a mass loss rate in LkHα101 of 4×10^{-5} M$_\odot$ yr^{-1} in a relatively cool, (8000 K), partially ionized, stellar wind (Cohen, Bieging, and Schwartz 1982, Becker and White 1988).

High-velocity wings and line broadening of the ^{12}CO (J=1$\rightarrow$0) line in LkHα101 were first reported over a decade ago (Knapp *et al.* 1976). Even then, the explanation offered for the line wings was the presence of "random expansion motions about a newly formed HII region" associated with the exciting Be star. In a survey for high-velocity CO line wings carried out with the 7 meter Bell Laboratories antenna, LkHα101 is listed among the "intermediate velocity sources" (10 km s^{-1} $< \Delta$v $<$ 30 km s^{-1} at $T_A^* = 100$mK) (Bally and Lada 1983). The authors point out that their data on these sources is inconclusive with

reference to deciding whether the observed linewidths reflect localized energetic activity, rotation, or turbulent, gravitationally bound motion in the ambient molecular cloud. It is the aim of this work to understand the gas dynamics of LkHα101 in the context of the molecular outflow phase of pre-main-sequence stellar evolution. The observations are described in § III. B. Results are presented in § III. C., the discussion in § III. D., and the conclusions in § III. E.

III. B. OBSERVATIONS

1) Optical

a) Palomar 1.5 meter CCD Camera and Filter System

Broadband images of LkHα101 and the surrounding region were taken on the Palomar 1.5 m telescope (f/8.8) on 16 November 1987. The transparency was good, with 1.5″ seeing and 20.8 mag arcsec^{-2} sky brightness at 6500 Å. The detector was an RCA CCD with 320 × 512 pixels. Device characteristics were 6e$^-$/DN (data number) with 30e$^-$ read noise. The scale was 0.47 arcsec/pixel, resulting in a 2.5′ × 4.0′ field. There was no guiding during the exposures, resulting in some minor, but noticeable, elongation of stellar images in each frame.

For various historical reasons, the filter system at the Palomar 1.5 meter telescope consists of pseudo-Johnson B, Johnson V, Gunn r, and Gunn i, instead of a pure Johnson-Cousins or Kron-Cousins system. This filter set has effective wavelengths of 4200 Å, 5400 Å, 6700 Å, and 8000 Å. The B filter is unusual in that it is slightly narrower than a normal Johnson B (700 Å FWHM versus the standard 1000 Å). Consequently, using the Palomar 1.5 m B filter results in fewer counts per second, and the color term in the photometric constants is reduced, relative to the standard Johnson B filter. This is an awkward setup for any observing program, since two separate sequences of standards must be taken each night to calibrate the blue Johnson filters and the red Gunn filters. It is also difficult to

define the Gunn filters properly, since many of the standards from Kent (1985) are too bright ($m < 10$ mag) for the 1.5 meter and saturate the chip in the minimum allowed, one second exposure time. The standards must, therefore, be taken out of focus, leading to scattered light and overlapping image problems. Another problem for the Gunn system is the very small number of blue standards (B - $V < 0.5$ mag), particularly in the fall sky.

In order to eliminate the problems outlined above, a program was undertaken during the 1986-1987 observing season by Dr. James Schombert to transform Landolt (1983) standards onto the Gunn system. A good range of color was selected to develop the zero points and color terms; however, the zero points quoted below are based on the stars HD19445, HD140283, and Ross 484 (Bessell 1988). The derived transformations from Cousins to Gunn filters are:

$$r = R_c + 0.280 + 0.038(R_c - I_c)$$

$$i = I_c + 0.605 + 0.067(R_c - I_c).$$

The reader is cautioned that these transformations are only first-order approximations, sufficient for the data in this study.

The software package ARCHANGEL was used for reduction of the raw CCD data. The first step was erase-level subtraction, the erase level being determined from 50 lines of overscan taken after each frame was read out. For exposures longer than 5 minutes, it was also necessary to subtract a dark frame of equal duration to remove noise from a hot amplifier in the upper (north) half of the CCD. These dark frames were collected during the daylight hours, and consist of averages of 10 for each exposure time. Flat fields were obtained from dome-illuminated, short exposures taken at least five times during the night, and flattening was good to the 0.3% level. Masks were applied to flattened data to flag one bad column and two regions of depressed chip sensitivity. Regions for sky determination

were located interactively on a color-graphics display. Normally, these regions would have consisted of several boxes of 20 × 20 pixels distributed symmetrically around the object of interest. However, LkHα101 fills most of the CCD frame. From comparison with the Second Palomar Sky Survey IIIaF plates, a region at the far east end of the absorption lane running south of LkHα101 was selected for a histogram determination of the sky value in each frame. Judging from the fact that the density level on the Sky Survey plate of this region was identical with density levels well outside the emission nebula, the sky error can be only at the 1% level. This error is negligible for the LkHα101 data, since most of the nebula has much higher surface brightness. Finally, the frames were cleaned of cosmic rays, and data from the single bad column in the chip were interpolated between data values in neighboring columns.

b) BVri Photometry

As mentioned above, the CCD data were calibrated using the standards of Landolt (1983), transformed to the Gunn system. The reader may use the above transformations to reconvert the r and i values to the Cousins system; however, the photometry presented here will be for the filter system in which the data were acquired. All exposures were 600 seconds, and were taken with airmass values near 1.0. For stellar objects, the photometry was undertaken using 6″ circular apertures. However, there is a great amount of nebulosity surrounding each star. The choice of 6″ diameter is a compromise between minimizing the amount of light from gas and maximizing the light of the stellar image. Obviously, this constraint serves as the primary source of error for the stellar photometry. Surface photometry measurements for the central nebula were made within a box 1′ on a side, centered on the peak of the extended emission north of LkHα101. The value for the total luminosity of the nebula is derived from the sum of all the light within the CCD frame minus the contribution of the stellar images. Comparison with new Palomar Sky

Survey IIIaJ, IIIaF and IV-N plates reveals that only 5% of the total luminosity at optical wavelengths is in the low-surface brightness regions outside the CCD field.

c) Coudé Spectroscopy

Two sets of high-resolution optical spectra of the nebulosity associated with LkHα101 were obtained in the 6550 Å – 6750 Å band on the night of 15 November 1987. The observations were made at the Coudé focus of the Hale 5-meter telescope, with a TI 800 × 800 CCD detector (Gunn, Harris, and Oke 1987). The reflection grating used was ruled at 600 grooves/mm with a blaze angle of 13°00′, yielding a dispersion of 0.281 Å/15 μm pixel in first order at the 36-inch focal length "camera" position. Higher orders were filtered out by a 3 mm thick GG495 pre-filter. The slit length was 30″ on the sky and was held fixed first in a north-south, next in an east-west, position by a dove-prism image rotator. The slit width was 0.4″ on the sky, corresponding to 25 km s^{-1} velocity resolution on the chip. The object was acquired by offsetting from a nearby SAO star. The integration was halted, and the object was re-acquired every 15 minutes during the 3 hour integration for the north-south slit position, and the 2.5 hour integration for the east-west slit position.

The data were erase-level subtracted, flat-fielded, corrected for atmospheric extinction, and transformed to a flux scale using HD19445 as the flux standard (Oke and Gunn 1983). The wavelength scale was determined using a Th-Ar comparison arc (courtesy of Dr. Geoff Marcy).

1) IRAS

The IRAS survey data were coadded for twenty-five individual passes over the LkHα101 region. Fluxes for LkHα101 in the four IRAS bands were determined from the point source filtered FLUX grids (*IPAC User's Guide 1986*). FLUX grid values were corrected for detector non-linearities, errors that were due to coadd processing, and sampling and position

uncertainties. No color correction was applied. The Coadd Intensity Grids were used for determination of the flux from the extended IRAS emission, after suitable background level subtraction. An average radial profile of the emission intensity was constructed in each of the four IRAS bands by fitting ellipses to the data in logarithmic steps of the radial coordinate.

3) Molecular Lines

a) FCRAO

LkHα101 was observed on 9 June 1986 in the J = 1→0 transition of CO and ^{13}CO with the Five College Radio Astronomy Observatory (FCRAO) 14 m antenna. The HPBW was 45″ at these frequencies. The velocity resolution was 0.27 km s^{-1}. Representative system temperatures were 485 K at ^{13}CO and 753 K at CO. Spectra were obtained by position-switching to $\alpha_{1950} = 04^h\ 29^m\ 30^s$, $\delta_{1950} = 35°\ 30'\ 00''$, a region devoid of emission. The map center coordinates, $\alpha_{1950} = 04^h\ 26^m\ 57.23^s$, $\delta_{1950} = 35°\ 09'\ 54.9''$, coincide with the VLA position of LkHα101. All offsets marked in the FCRAO maps are in minutes of arc from this reference position. Maps of the molecular emission were obtained on a 9 × 9 element grid, sampled every 15″. Total on-source integration time at each position was 90 seconds. Data calibration was achieved by inserting an ambient temperature load in the beam.

The SPA (Spectral Analysis) data reduction program (written by N. Scoville) was used to produce final maps and spectra of the molecular line emission in LkHα101. Raw data were corrected for atmospheric and forward-scattering losses ($\eta_{fss} = 0.72$), with no correction made for the source coupling efficiency, since the LkHα101 molecular cloud is larger than the beam. A constant baseline was fit to the line-free portions of the spectra, which were subsequently smoothed and rebinned to 1 km s^{-1} resolution.

b) OVRO

Observations of LkHα101 were made in the 110.271 GHz transition of the ^{13}CO molecule with the 3-element Owens Valley Radio Observatory interferometer during 1985-86. The synthesized beam was $8.7'' \times 6.3''$, p.a. $-1.0°$, and positional errors are estimated to be 20% of the beam size. A flux density of 4.0 Jy was adopted for W3(OH), the amplitude calibrator. The phase calibrator, 2021+317, was observed every twenty minutes. The available filterbank provided 0.136 km s^{-1} velocity resolution, with the central channel tuned to -1.5 km s^{-1} V_{LSR}. Bandpass calibration was achieved using the strong continuum source, 3C84. Further observational parameters are listed in Table III.1. The Astronomical Image Processing System (AIPS) was used to produce the deconvolved, source-brightness distributions.

III. C. RESULTS

1) Optical

a) BVri Photometry

The Gunn i CCD frame of LkHα101 is presented in Figure III.1. Only three stellar objects are visible in all four (B, V, r, and i) frames: star A, the northernmost object in Figure III.1, star B, in the northeast corner, and LkHα101 itself. All three have the appearance of being embedded in the neighboring gas and dust. Photometry of the stars marked A, B, and LkHα101 is presented in Table III.2, along with photometric values for the inner nebula (defined by a box $1'$ on a side), and the entire nebula. A comparison of the V and i frames is highly suggestive, in that there are 23 more stellar objects in the Gunn i bandpass than in the V. Furthermore, a total of 9 weak, compact radio sources in the $8' \times 10'$ field centered on LkHα101 have been reported in a recent VLA study. One of these sources is an extragalactic double. Optical spectroscopy of three of the remaining eight VLA sources shows that two are T Tauri stars and one a highly obscured B star (Becker and White 1988). Star B of Figure III.1 is one of these T Tauri stars. Intriguingly,

the star corresponding to Becker and White's VLA Source 1 has very red colors, judging by its appearance in the B, V, r, and i frames of the present work. Note that of the three stars, A, B, and LkHα101, which appear in all four bandpasses, LkHα101 and star B are both pre-main sequence objects. Star A has yet to be classified, along with the four remaining compact VLA sources, including VLA Source 1. Future spectroscopic work will be able to determine which of these unidentified sources are pre-main-sequence objects.

b) Structure and Color Mapping

Developing a useful way of presenting the complex structure of the extended emission surrounding LkHα101 is not a straightforward problem for two reasons: 1) The large dynamic range in intensity found within 2′ of the central region (over 3 orders of magnitude), and 2) the irregular shape of the nebula (which defeats regular contour fitting algorithms). Therefore, two complementary methods will be employed to present the same data: One is cross sectional analysis, the other, two-color mapping.

Figures III.2 and III.3 display two cross sections centered on LkHα101, taken north-south and east-west. Each shows a broad range in surface brightness (peaks of 18.3 r mag arcsec^{-2} and troughs of 23.5 r mag arcsec^{-2}). Although the surrounding nebula displays coarse symmetry and well-defined regions of absorption and emission, in fact, as can be seen in the cross sections, these regions exhibit an irregular distribution of intensity on small scales. Note that in both the north-south and the east-west cross sections, LkHα101 lies at the exact center of the boundary between bright emission regions and darker absorption lanes.

The second method of displaying nebular structure is differencing two images taken through different filters. For accurate, two-color mapping, a critical step is to register each frame to a common origin to insure that the pixel-by-pixel comparison is not distorted. For the data presented here, there were only three stellar images that appeared through

all four filters. These were analyzed for their centroids. Then, each set of centers was compared to the B frame set of images, and the corresponding transformations were calculated. Rotation and expansion terms were always negligible, so that only translations were required. The data in each frame were then rebinned into 3 arcsec pixels to increase the signal-to-noise before subtraction. The resulting image for the V and i frames is shown in Figure III.4. Visual inspection of this figure reveals a large amount of small-scale structure that is lost in normal intensity maps. In particular, the transition regions from absorption lanes to reflection nebulosity are strongly enhanced in this type of analysis. Exact values can be assigned by comparing the greyscale figures to the cross-section colors of Figures III.2 and III.3. Note that in general, the dark absorption features are redder than the high surface brightness regions because of the effects of extinction. The high surface brightness regions typically have $V - i$ colors from 0.5 to 1.0, whereas the dark lanes have much redder colors of 2.0 to 2.5. The reddest colors are found around the stars A, B, and LkHα101. Again, it is noted that LkHα101 lies on the boundary between blue and red regions as can be seen in the lower panels of Figures III.2 and III.3.

c) Coudé Spectroscopy

The Coudé spectra, integrated over the 30″ slit length, are presented in Figure III.5. Because of the presence of high cirrus and the lights of nearby communities, night-sky neon emission lines riddle the observed spectral region. These neon lines are marked NS (for night sky) in Figure III.5.

Figures III.6 and III.7 show the Coudé slit orientation superposed on the r image of LkHα101 and the variation of the Hα emission profiles with position along the slit. The line profile we see at different positions is produced by reflection off the dust grains surrounding the embedded Be star. The best-fit Gaussian to the Hα profile right at the position of LkHα101 gives the peak velocity as 21 km s^{-1} with a FWHM of 128 km s^{-1}.

This is to be compared with the Brackett α line from the same position, which has a peak velocity at -2 km s^{-1}, and a FWHM of 86 km s^{-1} (Persson *et al.* 1984). The difference in the peak velocities may be accounted for by differential extinction over the extent of the Hα line. Blue-shifted gas is scattered and absorbed more than the red-shifted gas; thus, we see relatively less emission from the blue side of the line than from the red. Therefore, scattering and absorption have the net effect of shifting the apparent line peak redward. The difference in linewidths must be due to the difference in sensitivity between the optical and infrared observations, the lower-level, highest-velocity emission going undetected in the infrared observations.

By comparing the observed Hα/Brα line ratio to that predicted for an optically thick, hot plasma, we derive an extinction of 8.7$\pm$0.2 mag at Hα along the line of sight to the Be star. This translates to an A_V of 8.9 for a $1/\lambda$ extinction law. We can also derive the visual extinction to LkHα101 from the molecular hydrogen column density, available from the FCRAO data. This latter determination yields $A_V = 9.0^{+0.3}_{-0.75}$, suggesting that nearly all of the molecular gas we see is in front of LkHα101, in agreement with previous models of the source (Dewdney and Roger 1982).

2) IRAS

From the point source filtered Coadd Survey Flux grids (pixel size 1′× 1′), fluxes in the four IRAS bands were: 356 Jy at 12 μm, 269 Jy at 25 μm, 2692 Jy at 60 μm, and 3904 Jy at 100 μm. Integration of *all* the extended IRAS emission, centered on LkHα101, from the Coadd Survey Intensity grids, yields fluxes of 1033 Jy at 12 μm, 1228 Jy at 25 μm, 10111 Jy at 60 μm, and 15608 at 100 μm, *including* the contribution of the central "point" source cited above.

The IRAS Coadd Survey Intensity maps of the LkHα101 region are presented in Figure III.8. The highest peak intensities in all four bands are located at the position of

LkHα101, showing it to be the dominant source of dust heating in this region. Figure III.9 shows the azimuthally averaged radial variation of the IRAS emission intensity maps of Figure III.8. The straight line above the data points in this figure represents an r^{-3} falloff of intensity with radius. Note, for the most part, how closely all four curves follow this law. This empirical relation can be simply explained. The radiation from the central source falls off as r^{-2}. The remaining r^{-1} dependence may be due to the dust *surface* density distribution, or a dust volume density distribution, which scales as r^{-2}.

The spectral energy distribution of LkHα101, from visual to millimeter wavelengths, is plotted in Figure III.10. The curve is double-peaked and is well fit by *three* component blackbodies. All three components are assumed to have dust opacity laws scaling as inverse wavelength for $\lambda < 250$ μm, and as λ^{-2} for $\lambda > 250$ μm. The three input parameters for each blackbody fit are the effective temperature, the 250μm opacity, and the source size. The best-fit parameters to the optical data are: T_{eff} = 1130 K, τ_{250} = 0.002, and a source diameter of 0.022″. The mid-infrared data are fit with T_{eff} = 600 K, τ_{250} = 0.2, and source diameter of 0.075″. Finally, the IRAS data fit a curve with T_{eff} = 50K, τ_{250} = 1.0, and a source diameter of 10″ extent. Integration under the curve of Figure III.10 yields a luminosity of 1.09×10^4 $L_\odot$, in good agreement with the previous determination of 1.2×10^4 $L_\odot$ (Harvey, Thronson, and Gatley 1979). The foregoing refers only to the immediate vicinity (within 4000 AU) of LkHα101. However, as noted in the introduction, infrared emission is detected by IRAS over a much larger area in this source (see Figure III.9). The spatial correlation of the HI and IRAS emission is excellent. The HI gas has an emission component with intensity 57 K, FWHM 7.4 km s^{-1}, and central velocity 1.5 km s^{-1} V_{LSR}, as well as an absorption component with a peak brightness temperature drop of 43 K, FWHM of 3.4 km s^{-1}, and 1.2 km s^{-1} central velocity. The derived spin temperature for the absorption component is 11 K (Dewdney and Roger 1982). The

lowest derived IRAS color temperature is 40 K. The molecular gas, if CO is thermalized, is at 15–20K. The dust is clearly hotter than the gas.

3) Molecular Lines

a) FCRAO

Contour maps of the integrated CO and ^{13}CO emission are presented in Figure III.11. Figure III.12 is a map of the column density of CO integrated over all velocities with significant emission superposed on the Gunn i CCD frame of the same region. The column densities were derived using Equation (A2) of Scoville *et al.* 1986. Note the correspondence between the dust lane and increasing gas column density in the southeast. The derived mass of molecular gas (using equation (A6) of Scoville *et al.* 1986) in the 2′ × 2′ field centered on LkHα101 is 112 $M_\odot$.

The line shapes as a function of position are plotted for CO in Figure III.13. Although the observed linewidths in LkHα10 are a factor of 10–20 greater than that expected from thermal broadening alone, no low-level, higher-velocity wings are seen at the 0.5 K rms level. Observations with the Bell Laboratories 7-meter telescope confirm the lack of high-velocity wings at the position of LkHα101 to the 0.1 K level (Bally 1982). Thus, there is no evidence in the single-dish data for large-scale, ordered, mass motion, such as would be expected from a molecular outflow source. In particular, there is a definite absence of any *bipolar* outflow. The line profiles in Figure III.13 have multiple components. The dip at 0 km sec^{-1} V_{LSR} may be due either to two separate clouds along the line of sight, or to cool, foreground material. The latter case is the more likely one, because of previous evidence for such material from HI data (Dewdney and Roger 1982).

b) OVRO

At the position of LkHα101, the interferometer detected only continuum emission. The integrated flux from this source is 185 mJy at 2.72 mm. The radio spectrum of

the unresolved core source in LkHα101 is presented in Figure III.14. The best linear fit depicted in this figure has a slope of 0.67, in excellent agreement with the $\nu^{0.6}$ dependence predicted for a stellar wind.

The ^{13}CO line emission reveals a more complicated source structure (see Figure III.15). We have marked the positions of five "cloudlets" surrounding the continuum source, which coincides with LkHα101. The total mass in these clumps, for T_{exc} = 20 K, is 23 $M_\odot$. The spectra of these condensations are shown in Figure III.16 (solid lines are FCRAO observations, dotted ones are from OVRO). Figure III.17 affords direct comparison of the FCRAO and OVRO maps of the region. Here we have direct evidence that the molecular gas distribution near LkHα101 consists of isolated small "cloudlets," as had previously been inferred from larger-scale HI and CO line shapes. Panel 1 of Figure III.16 shows that there is general large-scale, blue-shifted emission in the line of sight toward Cloudlet 1, since the interferometer does not detect emission in the $-3<V_{LSR}<0$ km sec^{-1} velocity range, whereas the single-dish observations do. The spectra of Panel 2 show the effects of beam smearing of Cloudlet 2 in the single-dish data, in which this gas clump is nearly undetected, whereas the interferometer is sensitive to it. Panels 4 and 5 show that both instruments were sensitive to the ridge of molecular emission, which coincides with the dark dust lane so prominent in the optical image of Figure III.1.

Comparison of the data of Figures III.16 and III.17 leads to the conclusion that the suprathermal molecular linewidths in this region are due to the superposition of many turbulent elements in one single-dish beam. Note that the linewidths decrease with the spatial scale of the observation: The interferometer linewidths are *always* narrower than the single dish linewidths at the same place on the sky. Turbulent gas motions over at least one factor of ten in spatial scale are inferred. This turbulent motion is corroborated by the small-scale, sharp variations in the nebular surface brightness apparent in the top

panels of Figures III.2 and III.3.

III. D. INTERPRETATION AND DISCUSSION

1) Large Scale (> 1′) Morphology and Gas Dynamics

a) Molecular Gas

It is clear from the foregoing that there is no *molecular* outflow associated with LkHα101. One might argue that LkHα101 could have been a molecular outflow source sometime in the past, having already cleared away most of the molecular gas in its immediate vicinity. However, no remnant expansion motions are seen in either the molecular gas or the atomic hydrogen velocity fields surrounding LkHα101, so any past molecular outflow could have lasted only a very short time. Figure III.18 shows the 5 GHz VLA map of LkHα101 superposed on the optical Gunn i CCD frame. The dynamical time scale of the extended VLA HII region in this figure is just 1.5×10^4 years.

A cartoon of the large-scale gas distribution around LkHα101 is depicted in Figures III.19a and IIII.19b (from Redman *et al.* 1986). The tickmarks in Figure III.19a indicate arcminute offsets from the star. Figure III.19c shows the VLA 5 GHz map of the region behind the "obscuring cloud" (Becker and White 1988). Note the suggestive spiral pattern in the outer portions of the ionized gas. In addition to the sources depicted in this figure, there is a larger-scale, cool (10 K) atomic *and* molecular "shell" or cold cloud between us and the LkHα101 cloud core, which manifests itself as the narrow self-absorption component at about 0 km s^{-1} V_{LSR} in the line profiles of Figure III.13, and in HI profiles (Dewdney and Roger 1986). With the higher resolution of the OVRO interferometer observations, the "obscuring cloud," depicted in Figures II.19a and b, breaks up into the five cloudlets of Figures III.15 and III.16. The column density in the "obscuring cloud" is highly variable, ranging from $N_{CO} < 10^{18}$ cm^{-2} to $N_{CO} = 6 \times 10^{18}$ cm^{-2} (see Figure III.12).

b) Far Infrared Emission

In view of such large-scale inhomogeneities in the gas distribution, it is interesting to note that one cannot characterize the dust and gas by a single kinetic temperature. While the molecular gas is at 10–15 K, a wide range of color temperatures may be inferred from the IRAS data of Figure III.9. Note, however, that LkHα101 is *the* chief energy source of the IRAS emission in the area, since its position coincides with the positions of the peak emission in all four IRAS bands. Using the 100 μm/60 μm flux ratio and assuming a λ^{-1} dust emissivity law, the IRAS "point" source color temperature is 42 K, and the extended emission color temperature, excluding this IRAS "point" source, is 40 K. Using the 60 μm/25 μm and 25 μm/12 μm flux ratios, derived dust temperatures are 58 K and 243 K, respectively, for the "point source," and 61 K and 193 K for the extended emission, excluding the "point source." These results show the coexistence of dust at many different "temperatures" in the same volume. That is, high- and low-temperature grains are *both* distributed over extended regions about LkHα101.

We are now left with the problem of explaining the origin of the emission in all four IRAS bands. The dust temperature for a grain in equilibrium with a stellar radiation field is given by (Sellgren, Werner, and Dinerstein 1983):

$$T_d = \left[\frac{Q_{UV} L_*}{16\pi\sigma r^2 Q_{IR}}\right]^{1/4},$$

where Q_{UV} and Q_{IR} are the Planck-averaged ultraviolet and infrared emissivities, σ is the Stefan-Boltzmann constant, L_* is the stellar luminosity, and r is the distance from the grain to the star. Values of Q_{UV}/Q_{IR} have been determined from observations of the NGC 7023 reflection nebula, and are in the range 2000 $\rightarrow$ 5000 (Whitcomb *et al.* 1981). Thus, we expect dust temperatures to be between 29–36 K 2 pc from LkHα101, a 10^4 $L_\odot$ star. For comparison, a 30 K blackbody, subtending a circular solid angle of 10′ radius,

would emit 2.6 μJy at 12 μm, 310 Jy at 25 μm, 1.63 $\times$ 10^6 Jy and 60 μm, and 8.77 $\times$ 10^6 Jy at 100 μm. The observed integrated fluxes from the emission regions shown in Figure III.2 (*including* the central "point" source) are 1033 Jy, 1228 Jy, 10111 Jy, and 15608 Jy at 12, 25, 60, and 100 μm, respectively. The point source fluxes alone are 356 Jy, 269 Jy, 2692 Jy, and 3904 Jy at these wavelengths. Therefore, close to 75% of the emission at each of these wavelengths originates from the extended region. The total luminosity of this extended region is 3.6 $\times$ 10^4 $L_\odot$.

Two questions arise from the IRAS data: 1) What is the source of the "excess" 12 μm and 25 μm emission ? and 2) How can there be so much cool dust (*i.e.*, 60 μm and 100 μm emission) close in to LkHα101? Without constructing an *extremely* detailed model that takes into account grain composition, grain size distribution, and radiative transfer effects, (and might *still* be wrong), we can state unequivocally that the mechanism(s) responsible for the IRAS emission must be due to photon-grain interactions. This conclusion follows immediately from the observed constancy of each color temperature with distance from the source. As with the photoelectric effect, the ejection of an electron, or infrared photon, in this case, depends not on the intensity of the surrounding radiation field, but rather upon the energy of the incident photon.

c) Optical Emission

From the optical picture of Figure III.1, note that LkHα101 lies exactly between the central nebula to the northwest and the dark absorption lane to the southeast. The position of LkHα101 is also midway, in luminosity gradient, between the peak and minimum surface-brightness values, a difference of 5 magnitudes (see Figures III.2 and III.3). We are looking at LkHα101 through a "hole in the clouds." Globally, in contrast to the symmetrical appearance of the overall nebula, the large-scale, optical surface brightness distribution in the LkHα101 region is not uniform. High surface brightness peaks and

filaments that wind around the nebula azimuthally are observed, pointing to a highly non-uniform density environment.

2) Small-scale Structure and Gas Dynamics

A small-scale source structure may be deduced from the model fit to the energy distribution of Figure III.10. The simplest resulting spatial distribution is an 18 AU diameter, inner region with $\tau_{6500} = 0.8$ and T = 1130 K, a 60 AU diameter, intermediate region with $\tau_{6500} = 80$ at T = 600 K, and an 8000 AU diameter, outer region with $\tau_{6500} = 400$ at T = 50 K. However, we know that the extinction to LkHα101 is $A_V = 8.7$ from two independent determinations: i) the ratio of Hα/Brα flux and ii) the ^{13}CO column density. Therefore, *any* consistent source model requires that material within 8000 au of the source be extremely anisotropic or clumpy.

A highly anisotropic distribution of matter near LkHα101 has been previously deduced by two independent lines of reasoning. From an analysis of the large-scale, HI column density distribution and the location of its peak, an equilibrium photodissociation model fits the data well "if the star is *locally* embedded in gas of high density with a conical opening towards the northwest" (Dewdney and Roger 1982). The radio continuum morphology of the emission nebula surrounding LkHα101 is quite complex. Nevertheless, a B0.V ZAMS star produces on the order of 1.6×10^{46} hydrogen-ionizing photons s^{-1}, resulting in a 22 AU Strömgren radius, if $n_e = 10^7$ cm^{-3}, or 8800 AU for $n_e = 10^3$ cm^{-3}. The radio continuum envelope observed by the VLA (see Figure III.18) exceeds this latter radius by a factor of three to four; therefore, there *must* be lines of sight along which ionizing photons can escape the inner core, necessitating the conclusion of a highly anisotropic or clumpy distribution of material near the star.

In the two-color map of Figures III.4, there is a distinct core region surrounding LkHα101. This region is $\approx$ 6000 AU in radius and is in the reddest portion of the

nebula ($V - i$ = 2.2–2.5 mag), compared with the dark lane's $V - i$ of 1.9 mag, and the central nebula's average $V - i$ of 0.9 mag. LkHα101 itself forms a blue hole at the center of this red core. The central pixel on which LkHα101 lies is 0.5 magnitudes bluer ($V - i$ = 1.7 mag) than the core color. Thus, if there is a spherical distribution of material immediately surrounding LkHα101, it cannot be completely opaque to blue photons. Another possibility is to assume a toroidal or disklike distribution of material surrounding LkHα101, in which case we must be looking at the system nearly pole-on.

The 6 cm VLA radio continuum map of the LkHα101 HII region is shown overlaid on the optical emission of the same region in Figure III.18. The radio spectral index of the core source is shown in Figure III.14. The best fit slope depicted in Figure III.14 is 0.67, in excellent agreement with the 0.6 slope predicted for an isotropic stellar wind (Panagia and Felli 1975; Wright and Barlow 1975). The mass loss rate is given by:

$$\dot{M} = 0.095 \mu v_\infty S_\nu^{3/4} D^{3/2} (g\nu)^{-1/2} \; M_\odot yr^{-1},$$

where $g(\nu, T_e)$ =10.6 + 1.90 log T_e − 1.26 log ν,

with ν in Hz, S_ν in Jy, D in kpc, μ =1.26, and v_∞ = 350 km s^{-1} (see below). The derived mass-loss rate for LkHα101 is 1.1 × 10^{-5} M$_\odot$ yr^{-1}. The characteristic inner radius of the radio-emitting region at a given frequency (*i.e.*, where τ = 1) is:

$$R(\nu) = 2.8 \times 10^{28} T_e^{-1/2} g^{1/3} \left(\frac{\dot{M}}{\mu v_\infty \nu} \right)^{2/3} cm.$$

This inner radius varies from 190 AU at 2.7 GHz to 16 AU at 110 GHz for T_e = 8300 K (Knapp *et al.* 1976; Becker and White 1988). The extended envelope of Figure III.18 contains about 0.1 M$_\odot$ of material at an average density of n_e = 100 cm^{-3} (Knapp, Kuiper, Knapp, and Brown 1976). If we assume that this entire extended HII region originated from the stellar wind, we may derive an age for the region: $\dot{M}/M$ = 9000 yr.

Next, let us consider what can be learned about the material immediately surrounding LkHα101 from the Hα line. Note that the optical nebula known as NGC 1579 shines by light from LkHα101, reflected from dust grains into our line of sight, so that the Hα profiles of Figures III.6 and III.7 give information about conditions in the close vicinity of the Herbig Be star. The observed FWHM of the Hα line toward LkHα101 is a factor of 10 (128 km s^{-1}) greater than the sound speed for a fully ionized, 8000 K HII region, while the line wings extend to $\pm$350 km s^{-1}, FWZI.

Stellar rotation can be ruled out immediately as the source of the Hα emission line profile, since rotationally broadened line profiles have a broad, characteristic shape unlike the observed line's sharp peak with extended wings (Rosseland 1936). Since there is strong evidence from the radio data for the presence of a powerful, ionized stellar wind in LkHα101, the Hα line wings may be attributed to this wind as well. However, we must still account for the relatively narrow widths of the Brα, Brγ, and H92α lines in the same source. The widths (FWHM) of these lines are 86 km s^{-1}, 40 km s^{-1}, and 17.5 km s^{-1}, respectively, although the Brackett γ profile does exhibit a broad (300 km s^{-1} wide), low-intensity component (Thompson *et al.* 1976; Persson *et al.* 1984; Simon and Cassar 1984; and Knapp *et al.* 1976). Simon and Cassar's value for the FWHM of the Brα line (40 km s^{-1}) disagrees with the value quoted by Persson *et al.* 1984.

The discrepancy amongst the derived hydrogen linewidths becomes less meaningful upon careful examination of the data. Note that the successful detection of low intensity, broad line wings depends upon many contributing factors, including the relative strengths of the continuum and line emission in the observed spectral region, the length, spectral resolution, and sensitivity of the observations, and upon large optical depth in the line wings. Since optical depth increases with decreasing wavelength, the longer the wavelength of observation, the smaller the line wing optical depth, or, equivalently, the

smaller the line wing emission strength. Since the continuum emission in LkHα101 is sharply rising from the optical to the near-infrared (*viz.* Figure III.10), broad, low intensity line wings become progressively harder to detect with increasing wavelength. The observed hydrogen lines, listed in decreasing order of peak signal to noise, are Hα, Brγ, Brα, and H92α, with the H92α line being a 1σ detection. It must also be mentioned in this context, that the near-infrared portion of the spectrum is riddled with terrestrial absorption lines, which can preempt detection of broad, low-intensity line features, and which must be corrected for. Such corrections were not made to the Brackett line data. In summary, all the available hydrogen line data are consistent with LkHα101 being the source of a stellar wind of 350 km s^{-1} terminal velocity.

The small-scale ($< 1'$) structure of LkHα101 is depicted in Figure III.20, incorporating all the available observations. Note the surprising variety and number of regions characterized by their different physical conditions. Of special interest is the previously reported "central hole" in the VLA emission, which coincides with the relatively blue pixel at the position of LkHα101 in the V–i picture of Figure III.4. Taken together, these data provide corroborating evidence for the presence of a stellar wind emanating from LkHα101. The far-infrared energy distribution of Figure III.10 provides evidence for an extremely opaque, swept-up dust shell. Beyond this dust shell lies the ring of molecular gas "cloudlets" resolved by the OVRO interferometer. Clearly, much of the molecular gas, which must have been present in the immediate vicinity of LkHα101 during its formation, has by now been ionized and swept away. The remaining molecular clumps, detected by OVRO, must lie along lines of sight protected from the ionizing flux of LkHα101 by the intervening dust. The OVRO cloudlets do overlap regions of low-density, ionized gas in projection. The coexistence of ionized and molecular gas at equal radial distances from LkHα101 provides further evidence for an extremely anisotropic, clumpy distribution of

material in the immediate environs of this young stellar object.

III. E. SUMMARY

If every massive, pre-main sequence star passes through a molecular outflow phase, then LkHα101 is a fossil outflow, since all the molecular gas in its vicinity has been swept away. Although LkHα101 is *not* the source of a *molecular* outflow, it is still the source of a powerful ($\dot{M}$=1.1$\times$ 10^{-5} $M_{\odot}$, FWZI = $\pm$ 350 km s^{-1}) *ionized* stellar wind. The physical conditions within the range 9 AU < r < 36000 AU of LkHα101 were derived by combining data from IRAS, the VLA, the OVRO interferometer, and optical imaging studies. The ionized wind in LkHα101 is surrounded by a swept-up, filamentary dust shell, which simultaneously shields the few remaining molecular gas cloudlets, and allows the escape of enough ionizing photons to produce the larger, low-density VLA envelope.

TABLE III.1

OVRO Observational Parameters

Configuration			Date	LST Range
10E	10W	20N	1985 DEC 12	23:16–12:20
20W	00N	30E	1985 DEC 22	23:14–07:09
10W	65W	50W	1986 FEB 06	04:20–09:30
10W	65W	50W	1986 FEB 11	23:30–05:10
30E	30W	40N	1986 MAR 31	00:42–08:07

Table III.2 Optical Photometry

Object	B	$B-V$	$V-r$	$r-i$	D
Star A	16.61	1.43	0.57	0.86	6″
Star B	15.26	1.34	0.48	0.61	6″
LkHα101	17.66	1.99	1.48	0.91	6″
Central Nebula	12.34	0.85	0.57	0.33	1′
Full Nebula	10.05	0.73	0.36	0.52	–

REFERENCES

Altenhoff, W. J.; Braes, L. L.; Olnon, F. M.; Wendker, H. J. 1976, *Astron. Ap.*, **46**, 11.

Bally, J. 1982 in *Regions of Recent Star Formation, ed.* Roger, R. S. and Dewdney, P. E., D. Reidel Publishing Company, Boston, Massachusetts, p. 348.

Bally, J. and Lada, C. 1983, *Ap. J.*, **265**, 824.

Becker, R. H. and White, R. L. 1988, *Ap. J.*, **324**, 893.

Bessell, M. S. 1988, private communication.

Brown, R. L.; Broderick, J. J.; Knapp, G. R. 1975, *M.N.R.A.S.*, **175**, 87P.

Cohen, M.; Bieging, J. H.; Schwartz, P. R. 1982, *Ap. J.*, **253**, 707.

Christie, R. A.; McCutcheon, W. H.; Chan, C. P. 1982 in *Regions of Recent Star Formation, ed.* Roger, R. S. and Dewdney, P. E. D. Reidel Publishing Company, Boston, Massachusets, pp. 343–348.

Dewdney, P. E. and Roger, R. S. 1982, *Ap. J.*, **255**, 564.

Dewdney, P. E. and Roger, R. S. 1986, *Ap. J.*, **307**, 275.

Finkenzeller, U. and Mundt, R. 1984, *Astron. Astrophys. Suppl. Ser.*, **55**, 109.

Gunn, J. E.; Harris, F.; and Oke, J. B. 1987, *P.A.S.P.*, **99**, 616.

Harris, S. 1976, *M.N.R.A.S.*, **174**, 601.

Harvey, P. M.; Thronson, H. A.; Gatley, I. 1979, *Ap. J.*, **231**, 115.

Herbig, G. H. 1956, *P.A.S.P.*, **68**, 353.

Herbig, G. H. 1960, *Ap. J. Suppl. Ser.*, **4**, 337.

Kent, S. M. 1985, *P.A.S.P.*, **97**, 165.

Knapp, G. R.; Kuiper, T. B. H.; Knapp, S. L.; Brown, R. L. 1976, *Ap. J.*, **206**, 443.

Landolt, A. U. 1983, *A.J.*, **88**, 439.

McGregor, P. J.; Persson, S. E.; Cohen, J. G. 1984, *Ap. J.*, **286**, 609.

Oke, J. B. and Gunn, J. E. 1983, *Ap. J.*, **266**, 713.

Panagia, N. and Felli, M. 1975, *Astron. Ap.*, **39**, 1.

Persson, S. E.; Geballe, T. R.; McGregor, P. J.; Edwards, S.; Lonsdale, C. J. 1984, *Ap. J.*, **286**, 289.

Redman, R. O.; Kuiper, T. B. H.; Lorre, J. J.; Gunn, J. E. 1986, *Ap. J.*, **303**, 300.

Rosseland, S. 1936, *Theoretical Astrophysics*, Clarendon Press, Oxford, pp. 202–210.

Schwartz, P. R. and Spencer, J. H. 1977, *M.N.R.A.S.*, **180**, 297.

Scoville, N. Z.; Sargent, A. I.; Sanders, D. B.; Claussen, M. J.; Masson, C. R.; Lo, K. Y.; Phillips, T. G. 1986, *Ap. J.*, **303**, 416.

Sellgren, K.; Werner, M. W.; Dinerstein, H. L. 1983, *Ap. J. Letts.*, **271**, L17.

Simon, M. and Cassar, L. 1984, *Ap. J.*, **283**, 179.

Simon, T.; Simon, M.; Joyce, R. R. 1979, *Ap. J.*, **230**, 127.

Spencer, J. H. and Schwartz, P. R. 1974, *Ap. J. Letts.*, **188**, L105.

Thompson, R. I.; Erickson, E. F.; Witteborn, F. C.; Strecker, D. W. 1976, *Ap. J. Letts.*, **210**, L31.

Whitcomb, S. E.; Gatley, I.; Hildebrand, R. H.; Keene, J.; Sellgren, K.; Werner, M. W. 1981, *Ap. J.*, **246**, 416.

Wright, A. E. and Barlow, M. J. 1975, *M.N.R.A.S.*, **170**, 41.

FIGURE CAPTIONS

Figure III.1 Gunn i (λ_o = 8000 Å, $\Delta\lambda$ = 850 Å) CCD frame of the immediate environs of LkHα101. At 0.47″/pixel, the image scale is 2.5′ × 4.0′. Only the stars marked A, B, and LkHα101 appear in all the observed bandpasses (B, V, r, and i). Star B is a T Tauri star, whilst the star marked VLA #1 is a strong candidate for a pre-main-sequence star (see text).

Figure III.2a North-south surface brightness profile along a line through LkHα101 (λ_o = 6700 Å, $\Delta\lambda$ = 1000 Å). The dark absorption lane to the south and the bright nebula to the north, as well as LkHα101, are all marked. The 30″ long slit, along which the Coudé spectra of Figures III.5a and III.6 were taken, is indicated. Note the central location of LkHα101 between the dark lane and the bright nebula.

Figure III.2b North-south V−i profile along a line passing through LkHα101. Note the sharp drop right at the position of LkHα101, indicating its blue color relative to its surroundings. This figure illustrates dramatically how much bluer the bright nebula is, compared with the dark dust lane.

Figure III.3a East-west surface-brightness profile along a line through LkHα101 (λ_o = 6700 Å, $\Delta\lambda$ = 1000 Å). The position of LkHα101 is marked, as is the Coudé slit position of the spectra of Figures III.5b and III.7.

Figure III.3b East-west V−i profile along a line passing through LkHα101. Again, note the sharp drop in V−i color at the position of LkHα101, confirming its blue color relative

to its immediate surroundings, as in Figure III.2b.

Figure III.4 V–i map of the LkHα101 region. North is up; east is to the left. Each pixel is 1.4″ × 1.4″ square. Darker tones indicate redder color. Note the relatively blue color of the pixel containing LkHα101, standing out from its much redder surroundings. The red dust lane to the southwest appears mottled because of its very low, V frame, pixel values. The white (relatively blue) region immediately to the north of LkHα101 corresponds to the bright nebula.

Figure III.5a Coudé spectrum taken through a 30″ long slit running along a north-south direction, centered on LkHα101. Night-sky neon lines are marked NS. The question marks indicate the locations of unidentified lines.

Figure III.5b As for Figure III.5a, except that the slit was positioned along a line running east-west.

Figure III.6 Variation of the Hα line profile as a function of slit position along a north-south line centered on LkHα101.

Figure III.7 Variation of the Hα line profile as a function of position along a slit oriented in an east-west direction and centered on the position of LkHα101.

Figure III.8 IRAS Survey Coadd Intensity maps of the LkHα101 molecular cloud at 12 μm, 25 μm, 60 μm, and 100 μm. Contour level units are W m^{-2} sr^{-1}. Negative contours

are indicated by dashed lines, and are due to overcorrection by the background level subtraction software. Positive contour levels are at 3.0, 6.0, 9.0, 12.0, 15.0, 20.0, 28.3, 40.0, 56.6, 80.0, 113.1, 160.0, 226.3, 320.0, 452.5, 639.9, 905.0, 1279.8, 1810.0, 2559.6, 3619.9, 5119.2, 7239.6, 10238.2, 14478.8, and 20476.0. Peak contour levels in each of the 12 μm, 25 μm, 60 μm, and 100 μm bands are at 2559.6, 3619.9, 10238.2, and 1810.0 W m^{-2} sr^{-1}, respectively.

Figure III.9 IRAS radial intensity distribution derived from fitting ellipses to the contours of Figure III.8 in logarithmic steps of the radial coordinate (arcminutes). Note the monotonic decrease in emission strength at all bands with increasing distance from LkHα101, which shows LkHα101 to be the dominant heating source in the cloud. Error bars on selected data points are representative for all the data. The intensity profile falling off as r^{-3} is indicated in the upper, right-hand corner for comparison with the observations. Note the good agreement between the data and the slope of this line, indicating the r^{-2} dust volume density distribution discussed in the text.

Figure III.10 The Spectral Energy Distribution of LkHα101

The filled squares are from McGregor, Persson, and Cohen 1984. The near and mid-infrared data are from Simon and Cassar 1984 and Simon, Simon, and Joyce 1979. The filled triangles are IRAS points, and the 2.7 mm flux is from the present work. The solid curve is the best fit to the data, and is the superposition of three component blackbodies, as described in the text.

Figure III.11a FCRAO map of the integrated CO emission in a 1.5′ × 1.5′ field centered on LkHα101 ($\alpha_{1950} = 04^h\ 29^m\ 30^s$, $\delta_{1950} = 35°\ 09'\ 54.9''$). Offsets are marked in minutes

of arc from this position. Contour levels are at 10, 15, 20, 25, 30, 35, and 40 K km s^{-1}.

Figure III.11b FCRAO map of the integrated ^{13}CO emission for the same field as in Figure III.11a. Contour levels are at 4, 5, 6, 7, 8, 9, 10, 11, and 12 K km s^{-1}.

Figure III.12 A map of the CO column density for the same field as in the previous figure, overlaid on the Gunn i image of the region. Contour level units are 10^{18} cm^{-2}. Levels are marked at 1, 2, 3, 4, and 5 times this value. Note the excellent correspondence between the obscuring dust lane and the CO column density contours.

Figure III.13 This figure shows the variation of CO line profile with position in the LkHα101 field as observed with the FCRAO 14 m radio telescope. The vertical axes are in units of T_R^* in 5 K units. The horizontal axes are in units of km s^{-1} V_{LSR}, the tick marks indicating 5 km s^{-1} intervals. Note the consistent, self-absorption feature at 0 km s^{-1}, indicating the foreground, cool shell material previously detected in HI 21 cm line observations. From this figure, the marked lack of organized motion, such as would be expected for a bipolar outflow source, is clear.

Figure III.14 The radio spectrum of LkHα101 from 2.7 to 110 GHz

The 2.7 GHz data points are from Spencer and Schwartz 1974 and Brown, Broderick, and Knapp 1975; the 4.9 GHz data are from Altenhoff *et al.* 1976 and Cohen, Bieging, and Schwartz 1982. The 8.1 GHz points are from Brown, Broderick, and Knapp 1975 and Spencer and Schwartz 1974. The 90 GHz point is from Schwartz and Spencer 1977, and the 110 GHz point from OVRO (this work). The straight-line fit has a slope of 0.67,

indicating $S_\nu \propto \nu^{0.67}$. This slope corresponds to what is predicted for a constant velocity, isotropic, ionized stellar wind.

Figure III.15 This figure is an overlay of the ^{13}CO emission detected by the OVRO interferometer overlaid on the corresponding Gunn i image of the field containing LkHα101. Note that the central source is *not* line emission, but 110 GHz continuum emission. All the other OVRO contours represent line emission, which breaks up into the "cloudlets" numbered 1 through 5. Note the clear anti-correlation between the ^{13}CO emission and the brightest part of the nebulosity.

Figure III.16 This figure shows the FCRAO and OVRO ^{13}CO line profiles of the cloudlets pictured in the previous figure. The numbers in the upper, right-hand corners correspond to the numbers assigned these condensations in Figure III.15. The OVRO points may be distinguished by their smaller velocity coverage with respect to the FCRAO data. The position of each spectrum is indicated in the upper, left-hand corner of each panel.

Figure III.17 The integrated OVRO ^{13}CO emission, with the 110 GHz continuum source at the position of LkHα101, is superposed on the map of integrated ^{13}CO emission as observed with the FCRAO single-dish. When comparing the two maps, note that the OVRO data cover only the central $1' \times 1'$ region.

Figure III.18 VLA 5 GHz map of LkHα101 overlaid on the Gunn i CCD frame (Becker and White 1988). From this figure, we can see that the VLA HII region is behind the

intervening obscuring cloud.

Figure III.19a Schematic representation of the large scale ($> 1'$) morphology of the gas and dust in the vicinity of LkHα101 (adapted from Redman *et al.* 1986).

Figure III.19b Side view of Figure III.19a.

Figure III.19c VLA image of the HII region behind the "obscuring cloud" depicted in Figures III.19a and b (from Becker and White 1988).

Figure III.20 Schematic representation of the small-scale structure of LkHα101 (9–36000 AU), deduced from a combination of infrared, optical, radio continuum, and millimeter line data.

Figure III.1 LkHα101 i

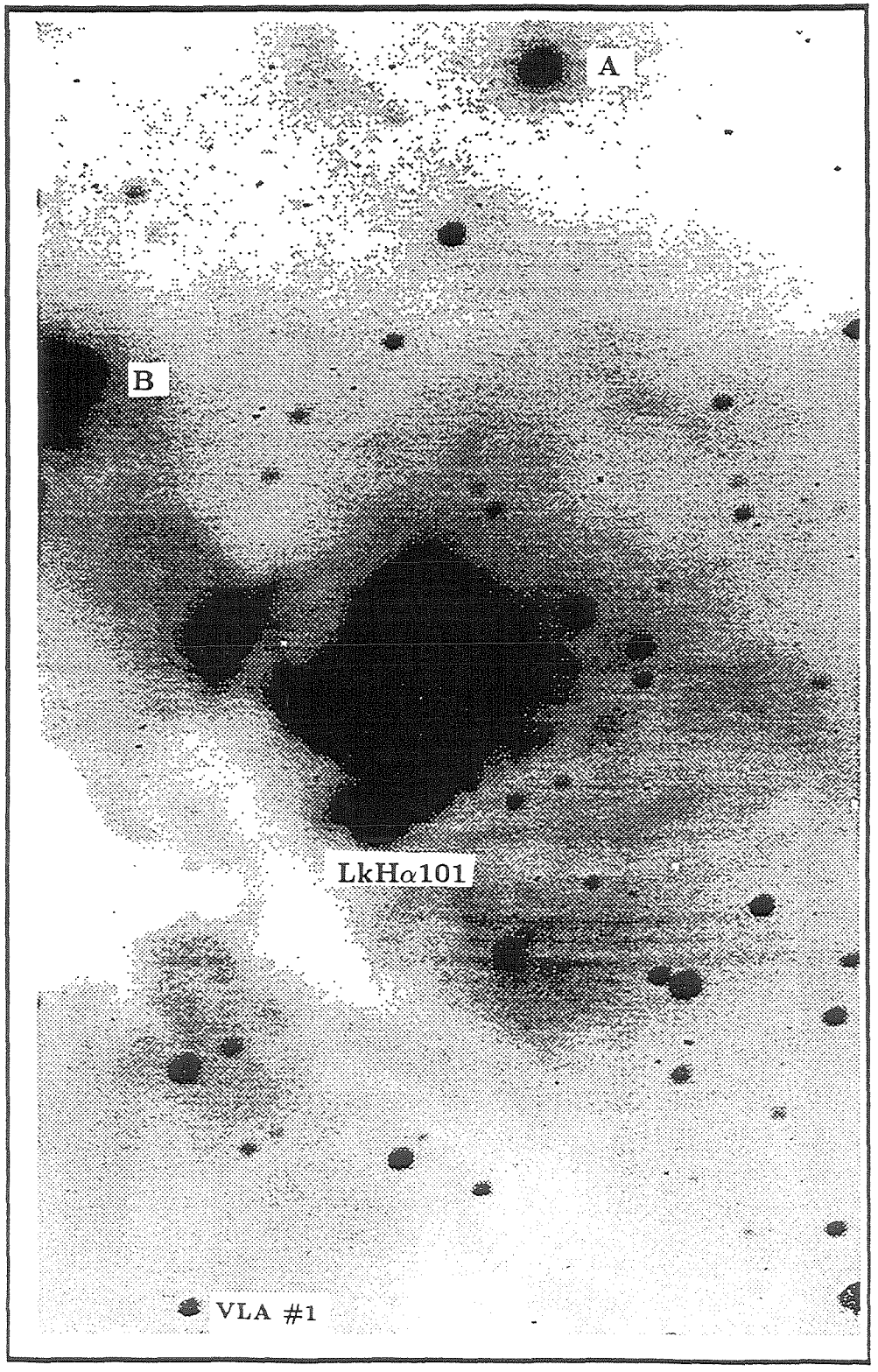

Figure III.2

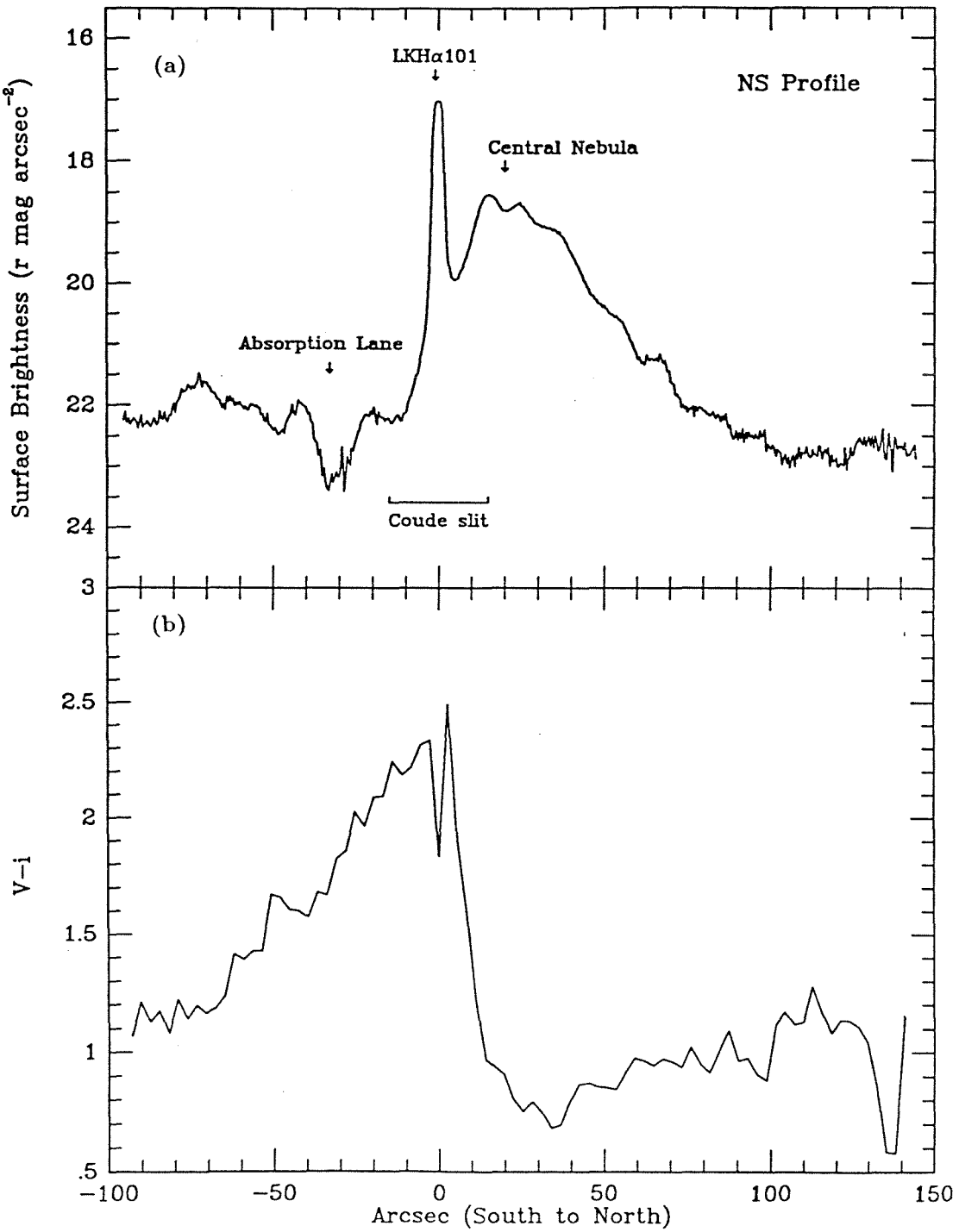
(a)
LKHα101
NS Profile
Central Nebula
Absorption Lane
Coude slit
Surface Brightness (r mag arcsec^{-2})
16
18
20
22
24
(b)
V−i
2.5
2
1.5
1
.5
−100
−50
0
50
100
150
Arcsec (South to North)

Figure III.3

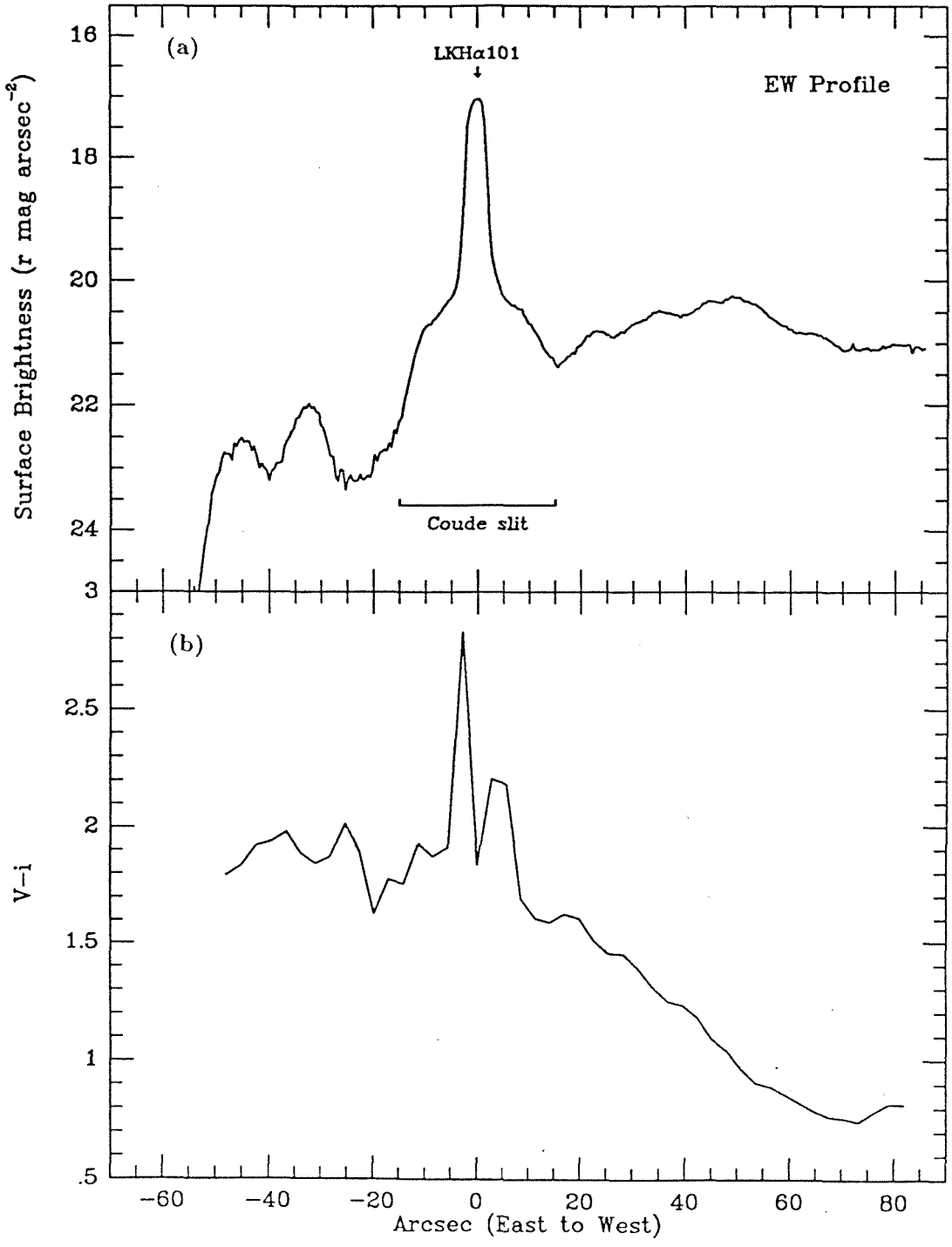
(a)
LKHα101
EW Profile
Surface Brightness (r mag arcsec^{-2})
16
18
20
22
24
3
Coude slit
(b)
V-i
2.5
2
1.5
1
.5
-60
-40
-20
0
20
40
60
80
Arcsec (East to West)

LKHa101 V-i

Figure III.4

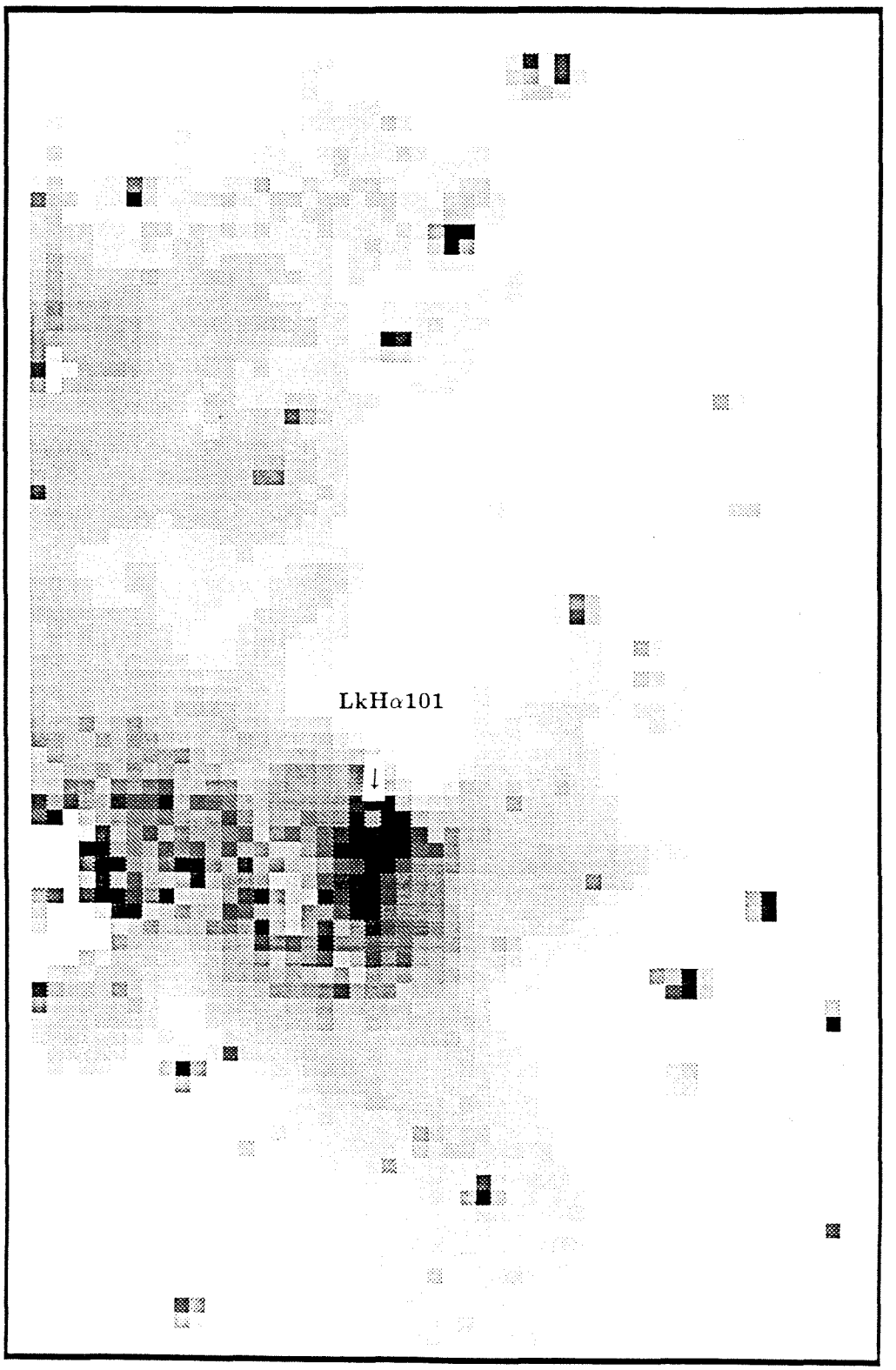

Figure III.5

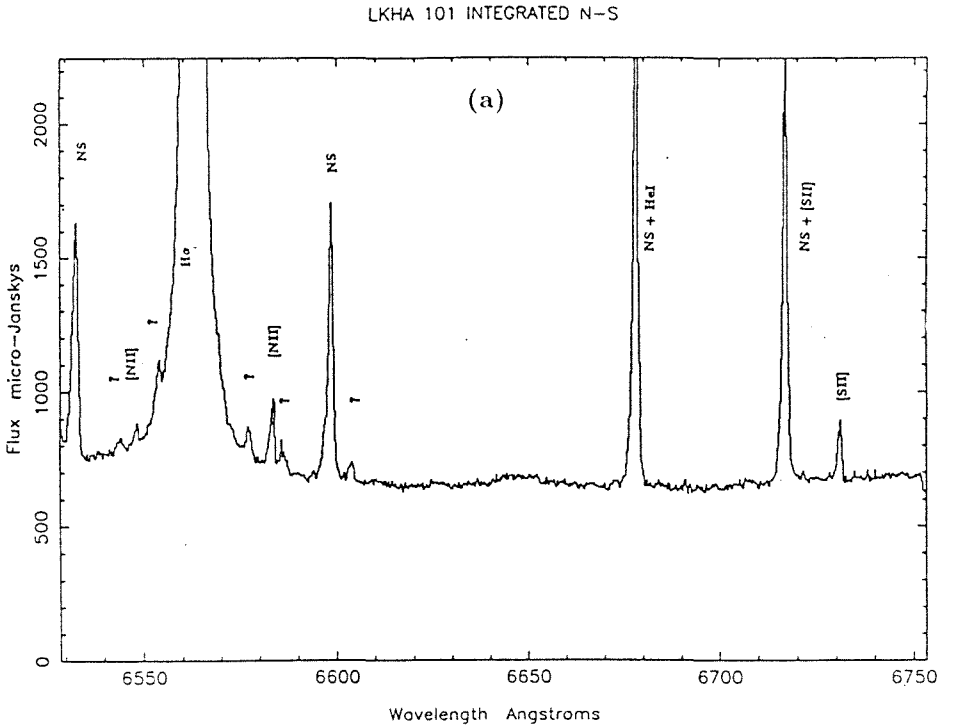
LKHA 101 INTEGRATED N-S
(a)
Flux micro-Janskys
Wavelength Angstroms
NS
[NII]
Hα
NS + HeI
NS + [SII]
[SII]
LKHA 101 INTEGRATED E-W
(b)
Flux micro-Janskys
Wavelength Angstroms
NS
[NII]
Hα
NS + HeI
NS + [SII]
[SII]

LkHα101 Figure III.6

VARIATION OF Hα LINE PROFILES ALONG NORTH-SOUTH SLIT

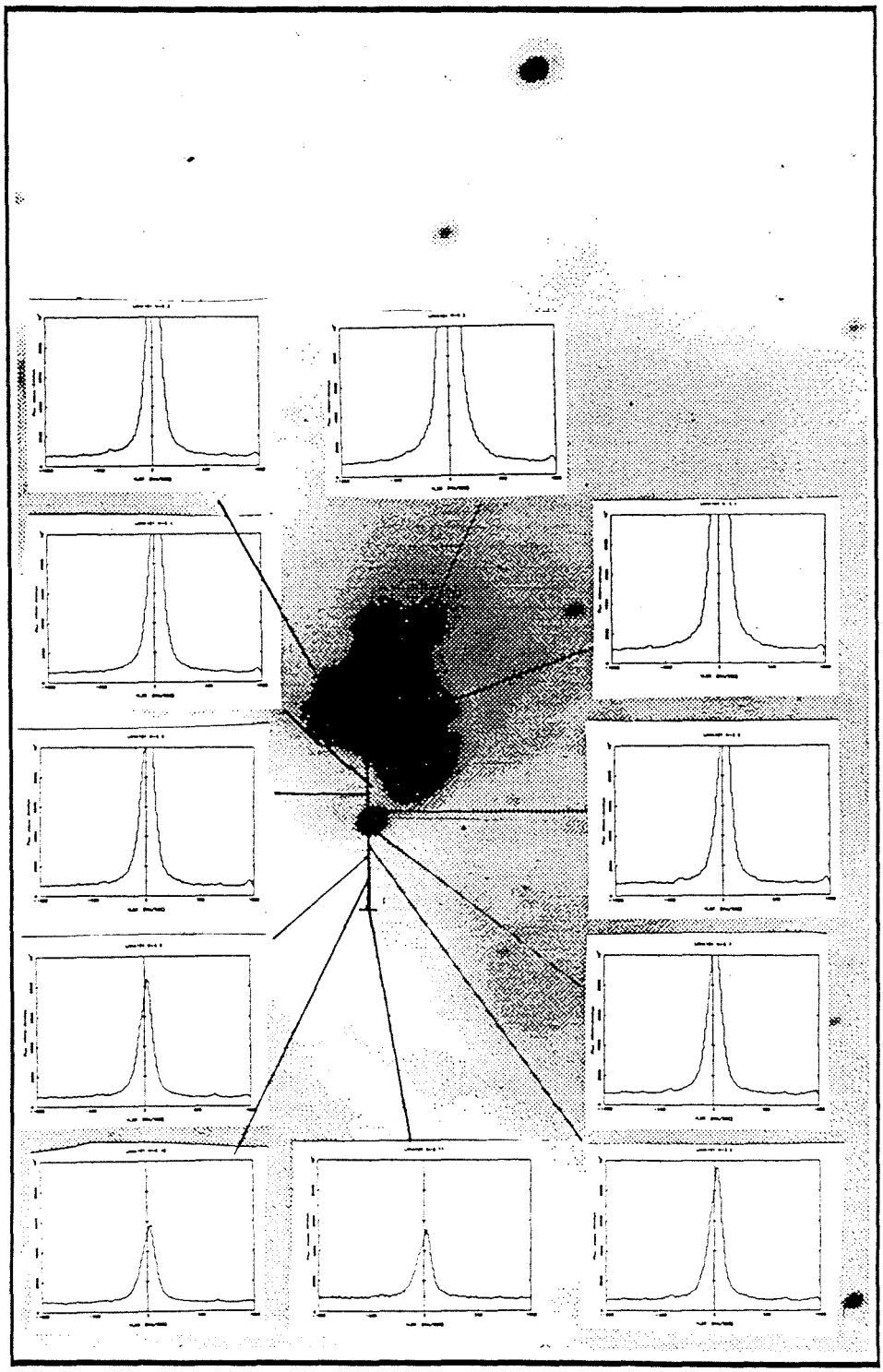

LkHα101 Figure III.7

VARIATION OF Hα LINE PROFILES ALONG EAST-WEST SLIT

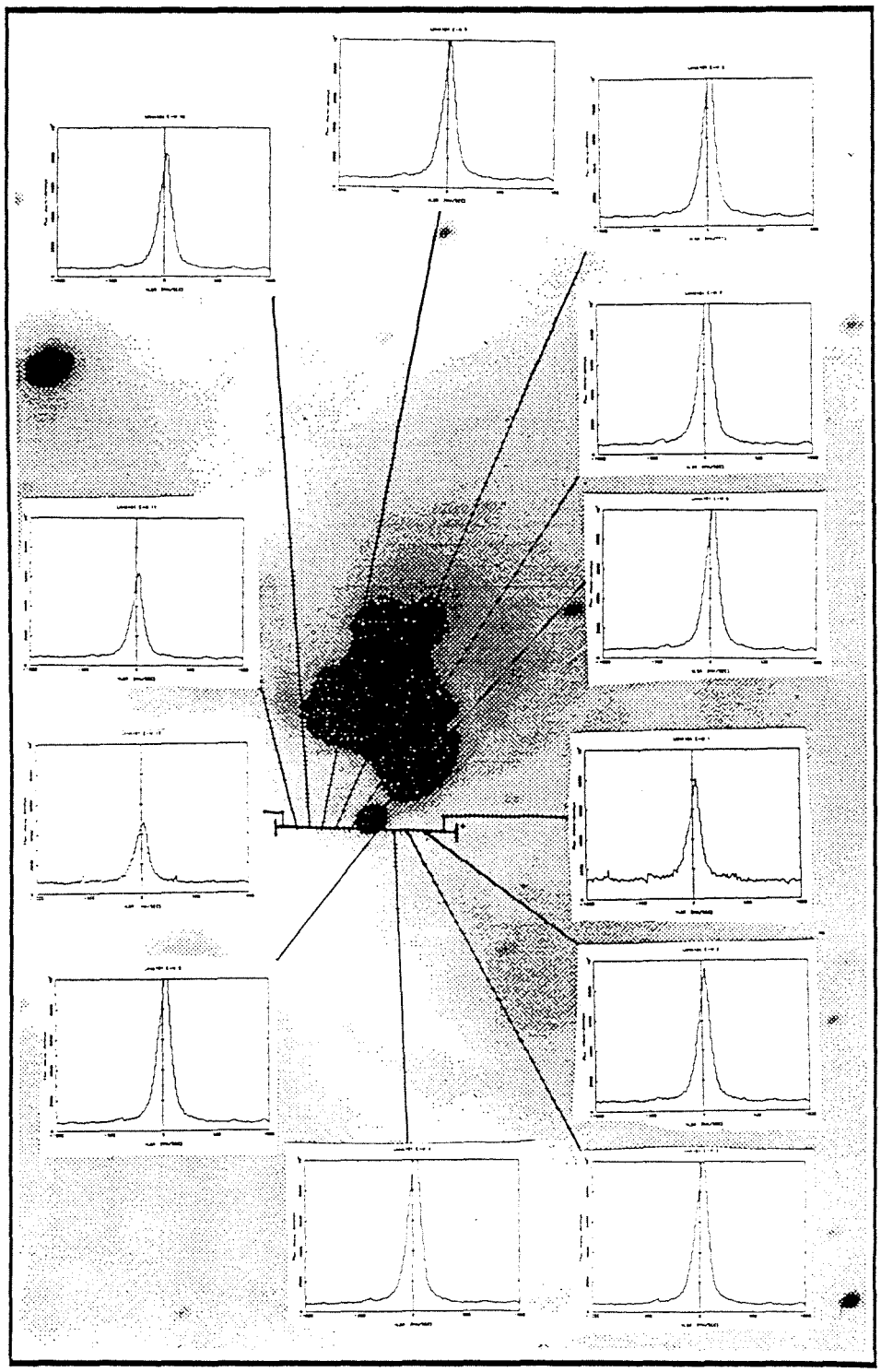

Figure III.8 LkHα101

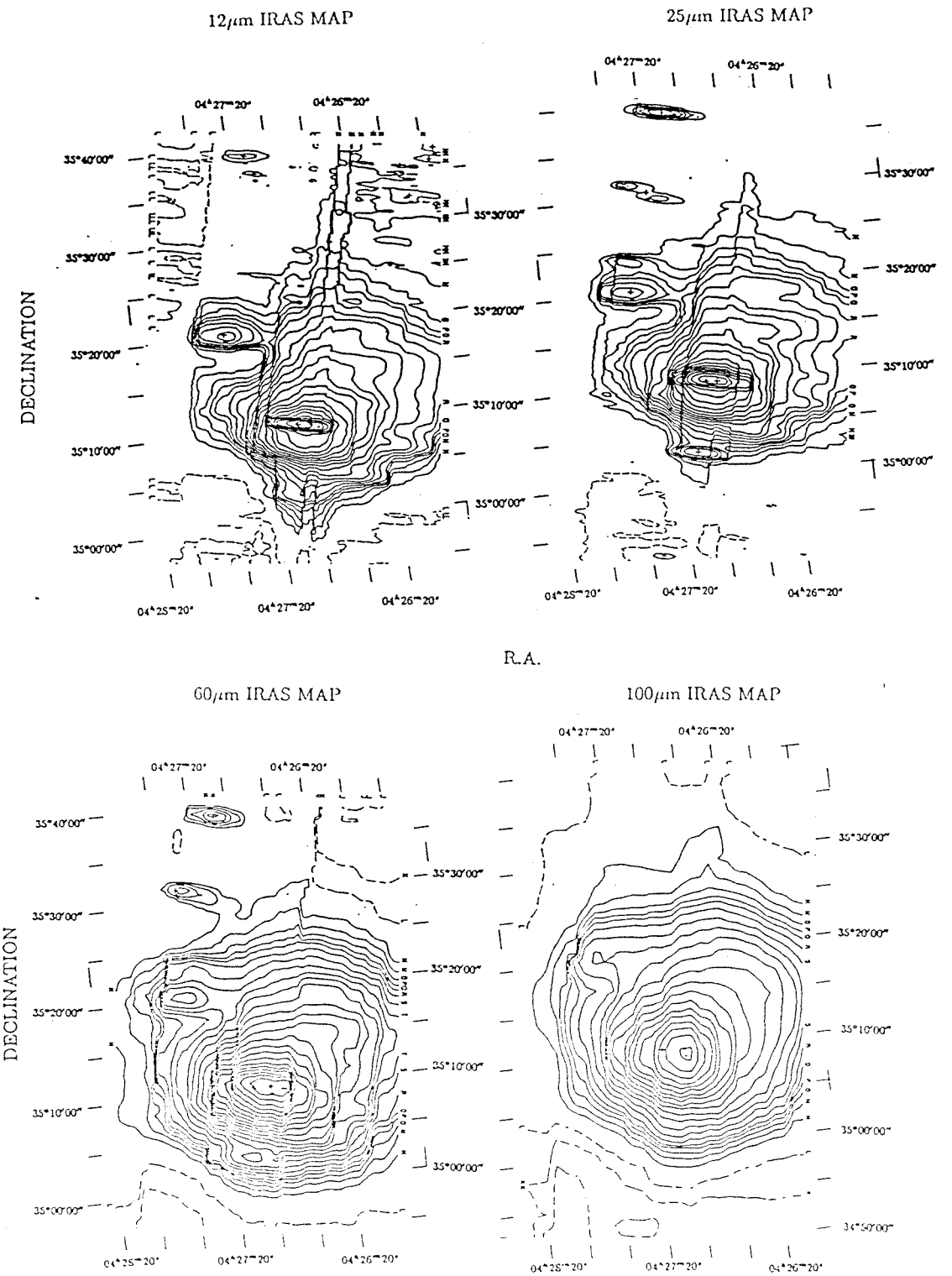

Figure III.9
RADIAL PROFILE OF DUST EMISSION INTENSITY

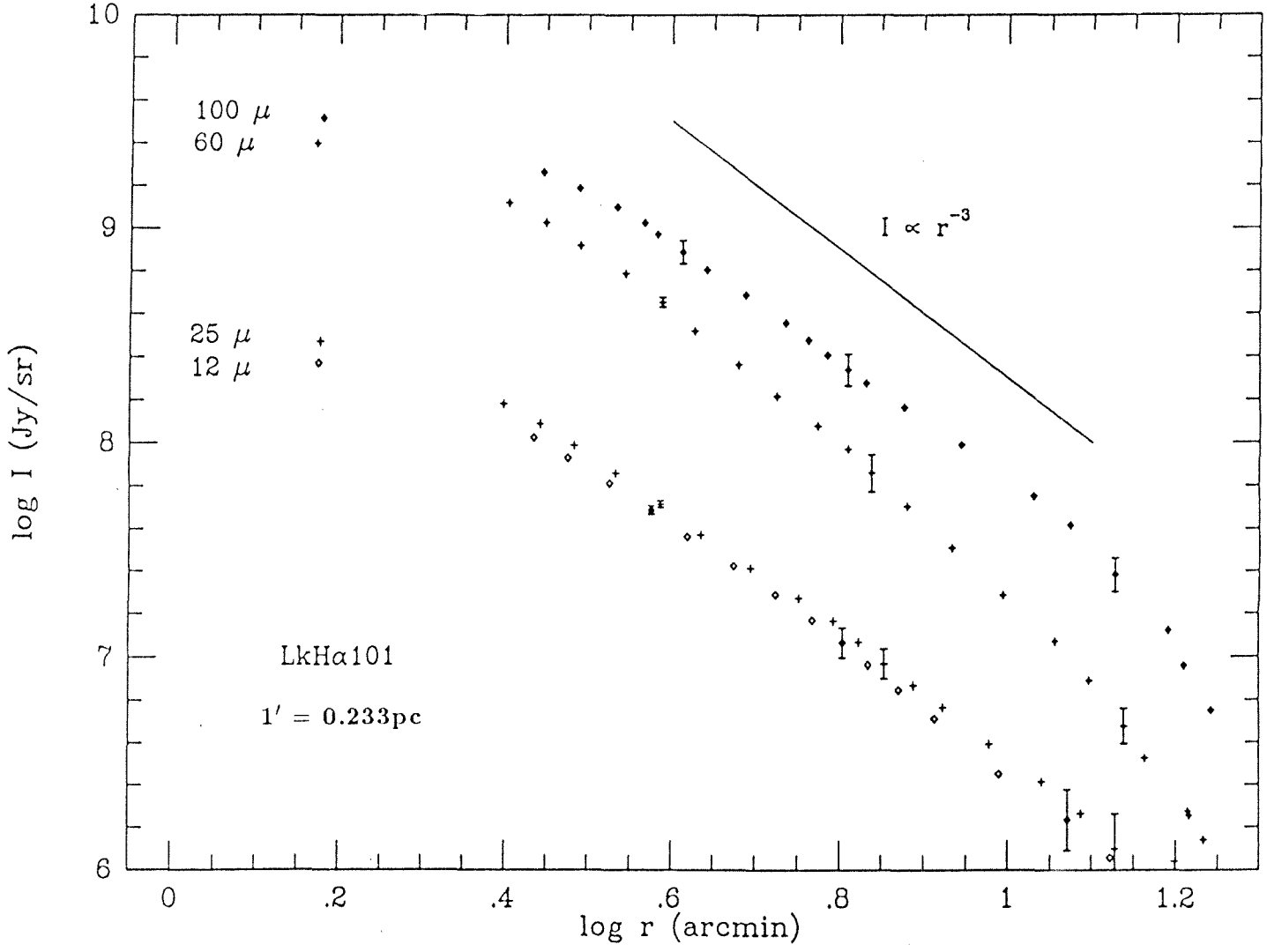

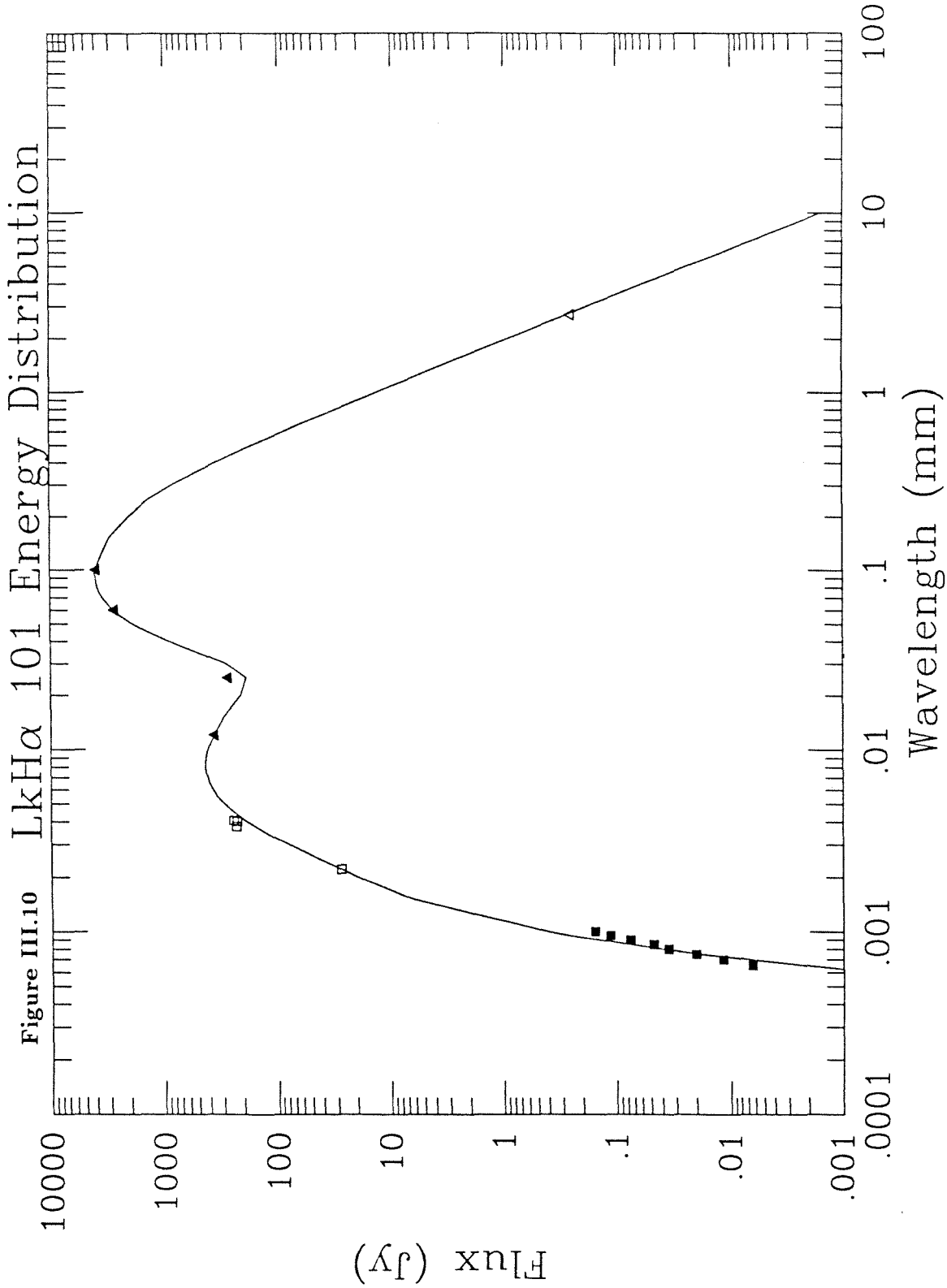

Figure III.10

Figure III.11

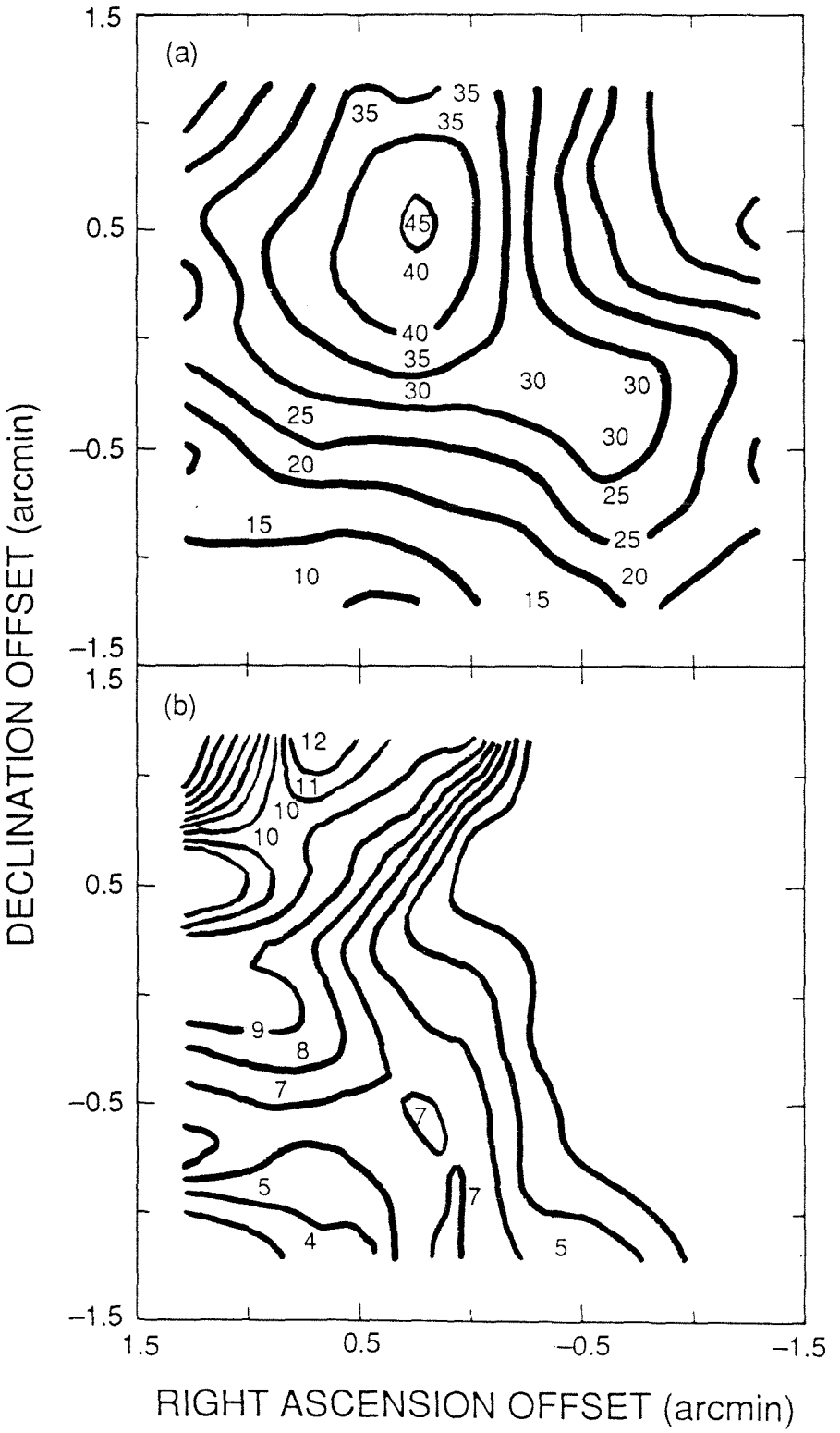

Figure III.12

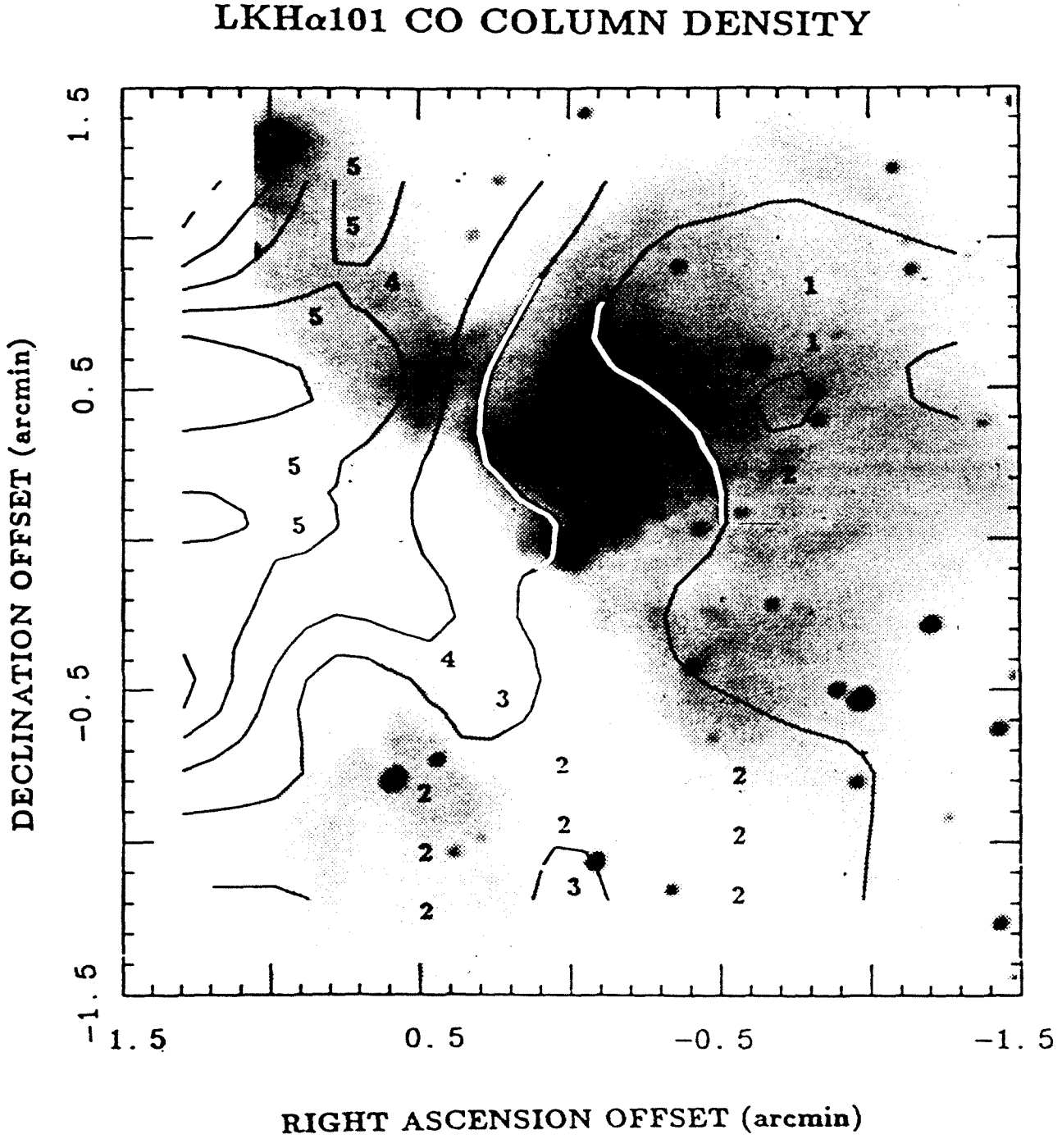

Figure III.13

Figure III.14 Radio Spectrum of LkHα101

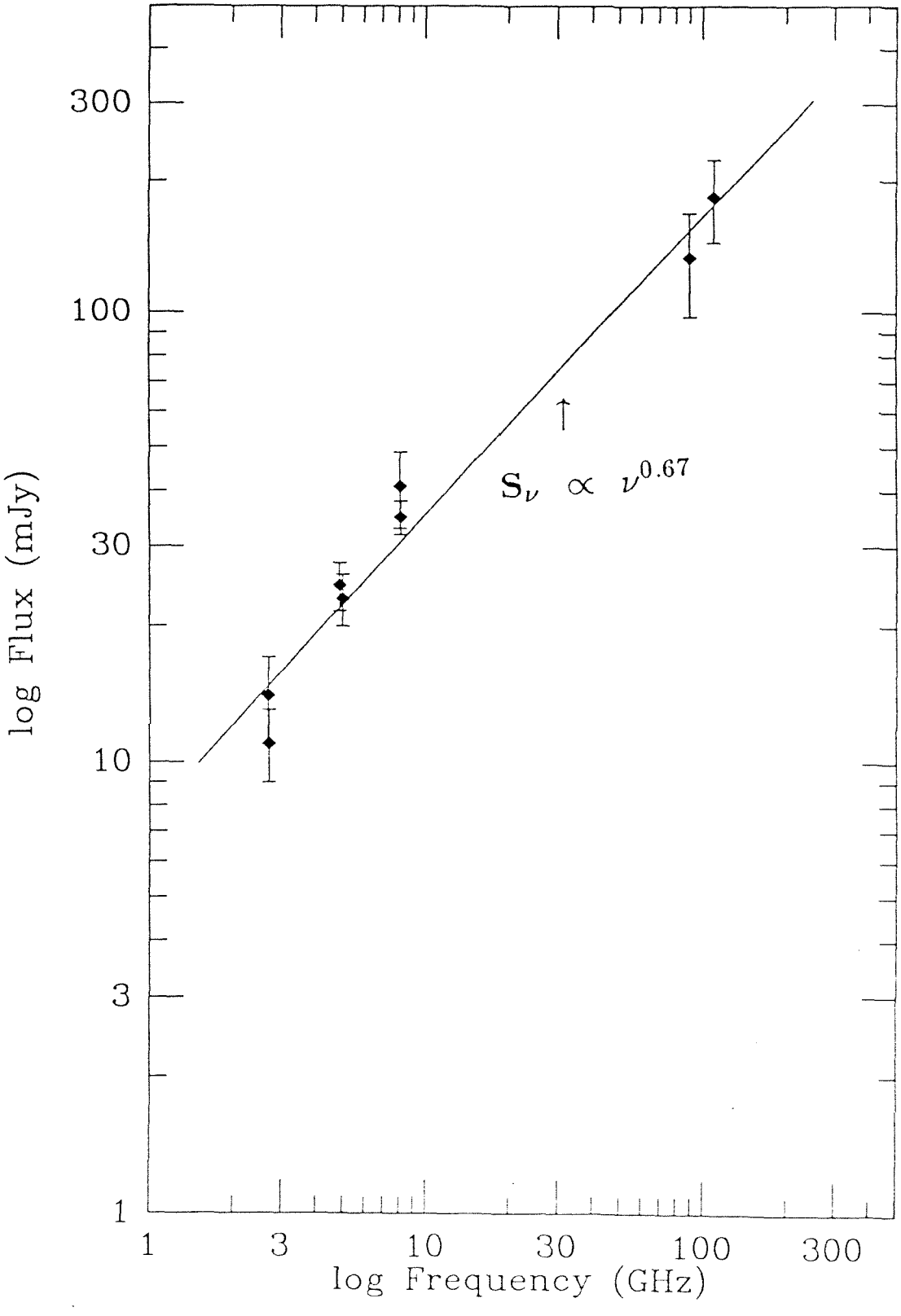

Figure III.15 MAP OF OVRO ^{13}CO EMISSION AND 110GHz CONTINUUM SOURCE OVERLAID ON GUNN i (λ_{eff} = 8000Å) IMAGE OF LKHα101

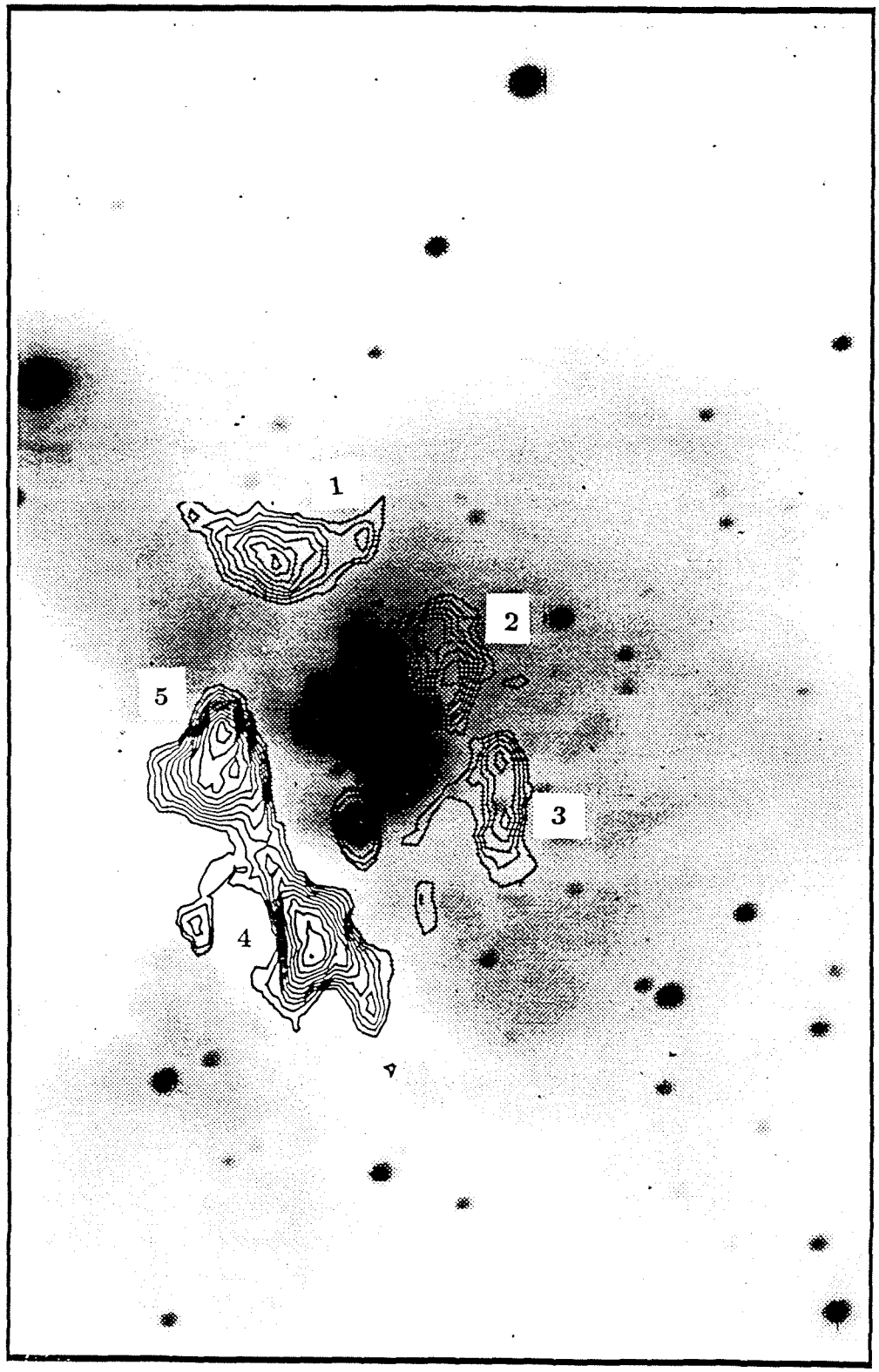

Figure III.16
OVRO AND FCRAO ^{13}CO SPECTRA OF CLOUDLETS SURROUNDING LKHα101

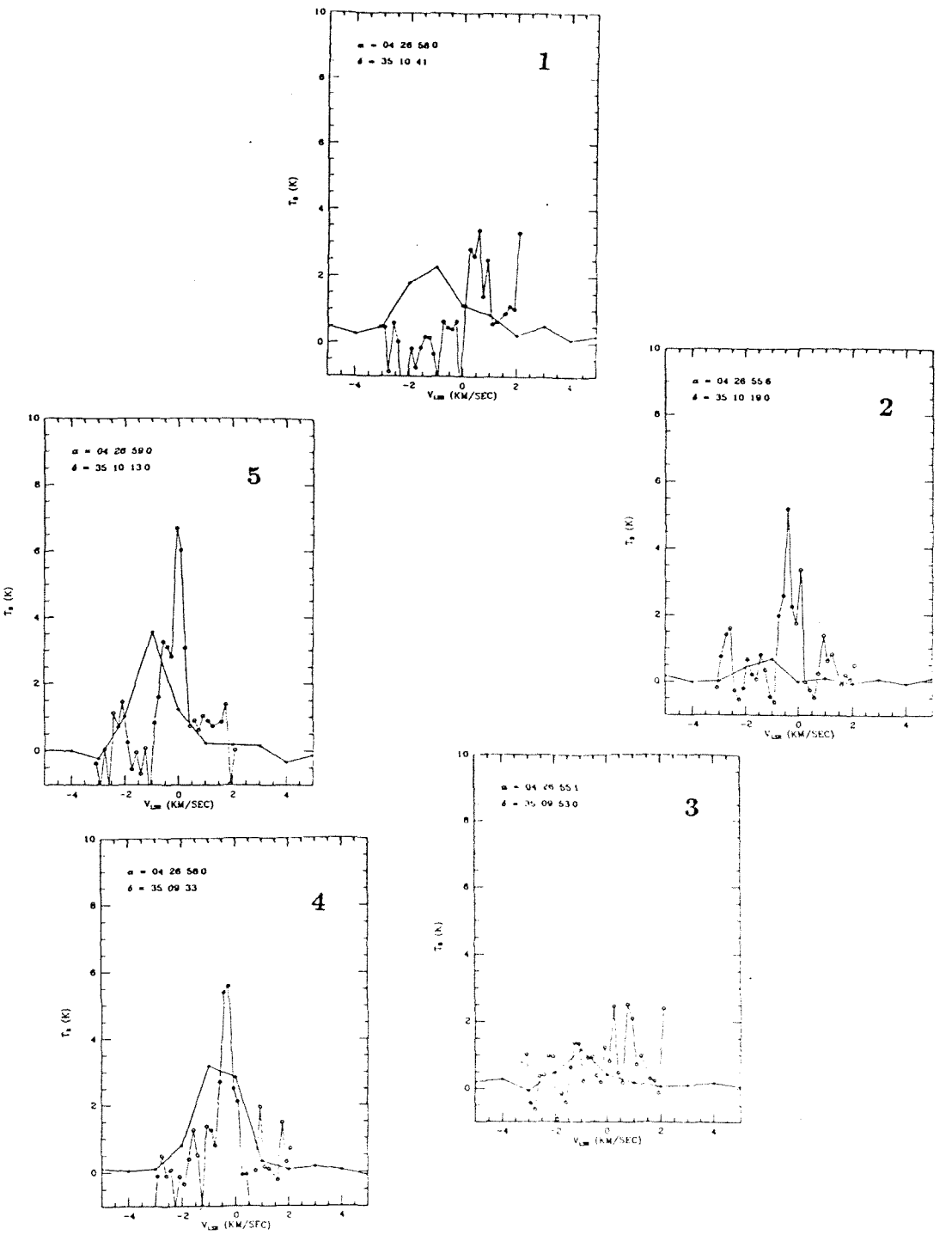

Figure III.17

OVRO AND FCRAO MAPS OF ^{13}CO EMISSION TOWARD LKHα101

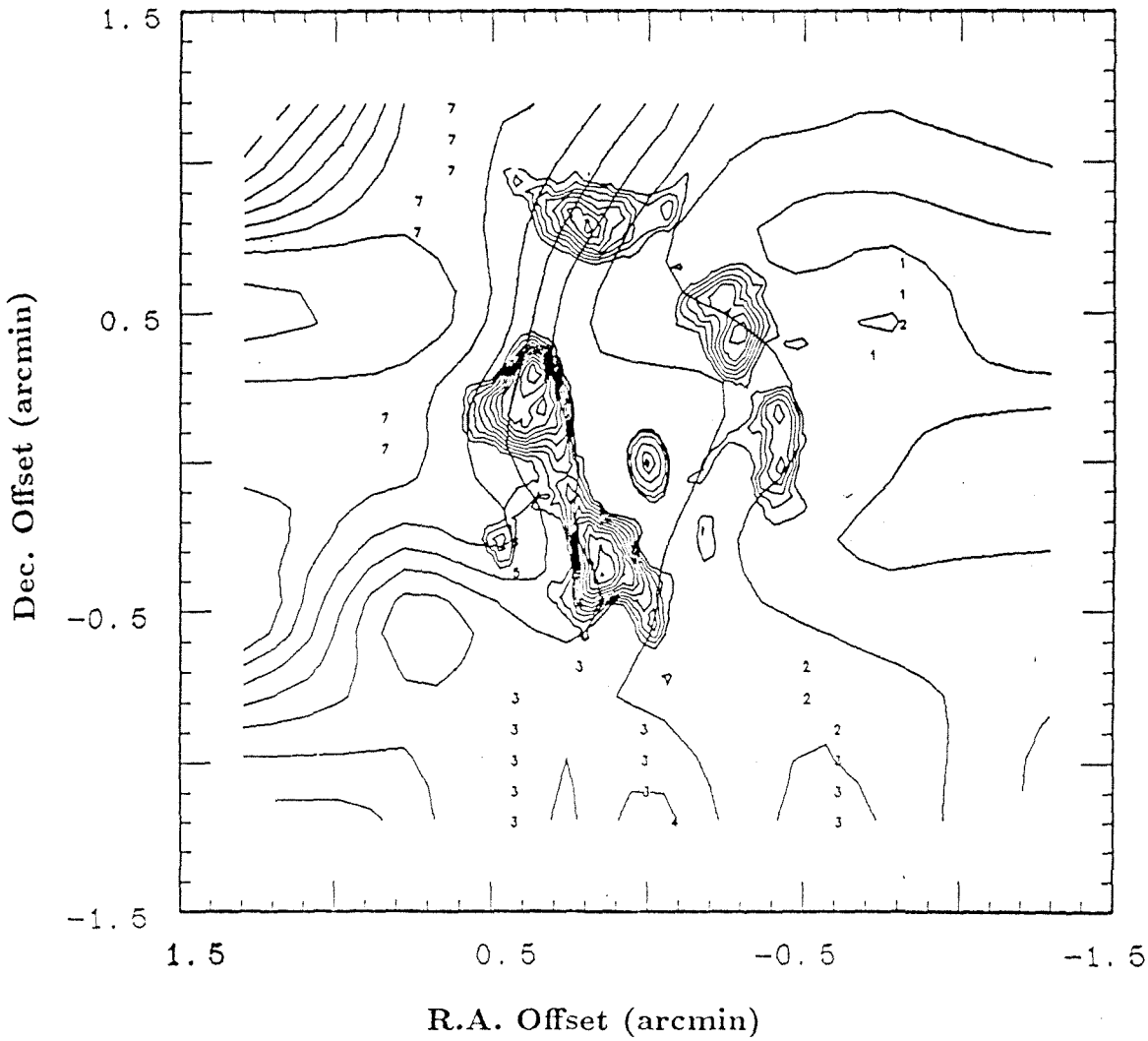

Figure III.18

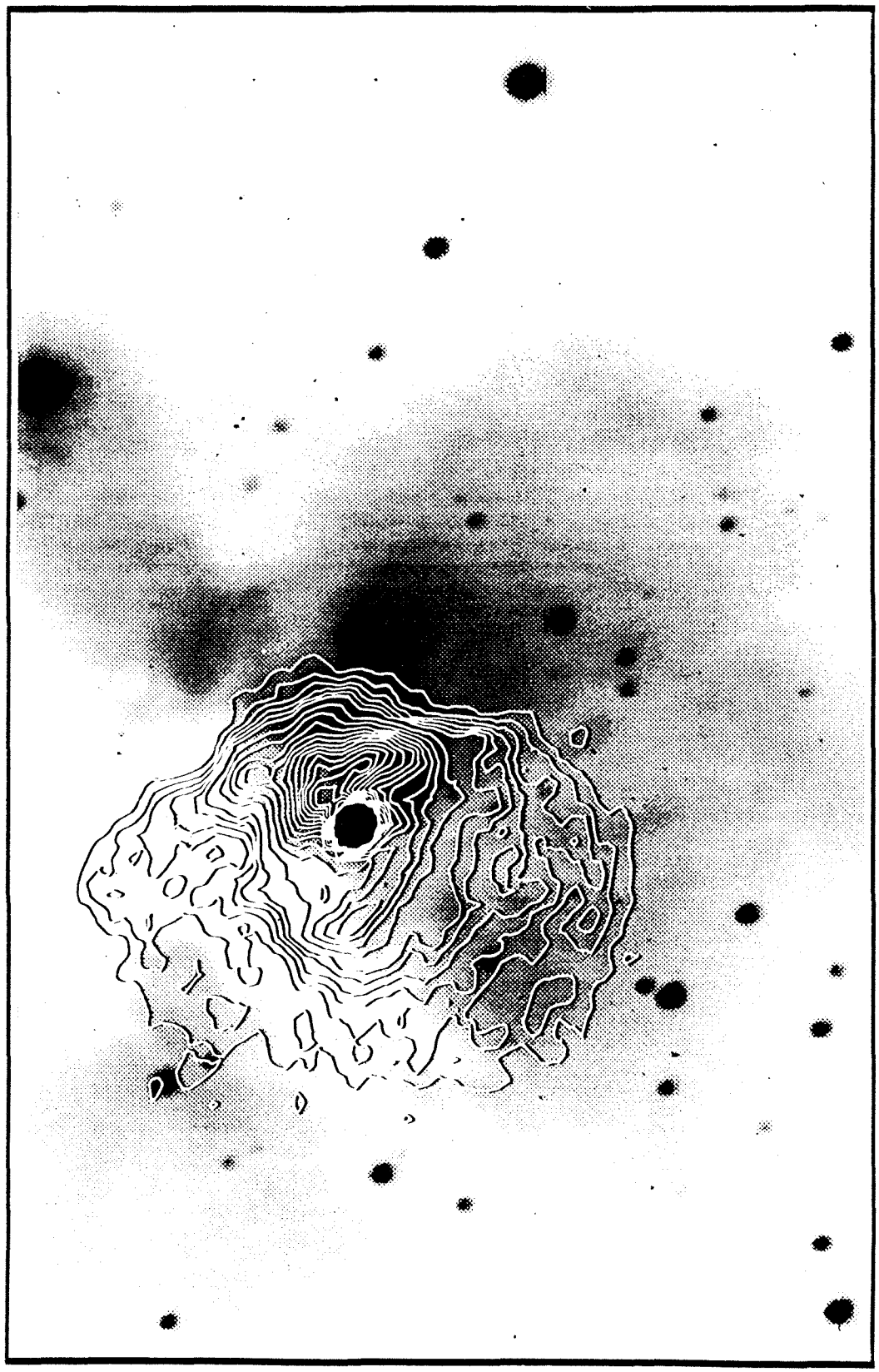

Figure III.19

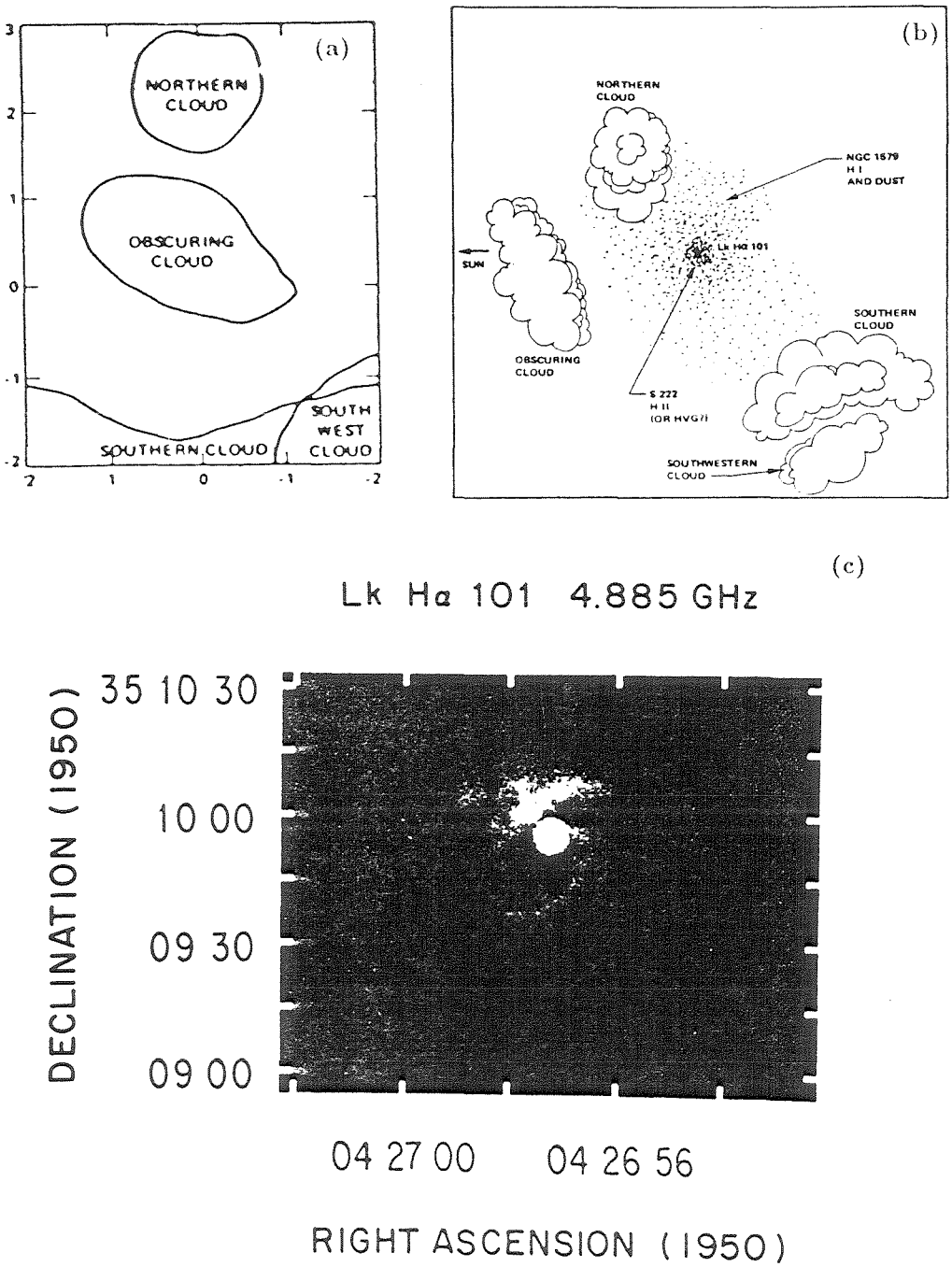

Figure III.20 Schematic of Small Scale Structure in LkHα101

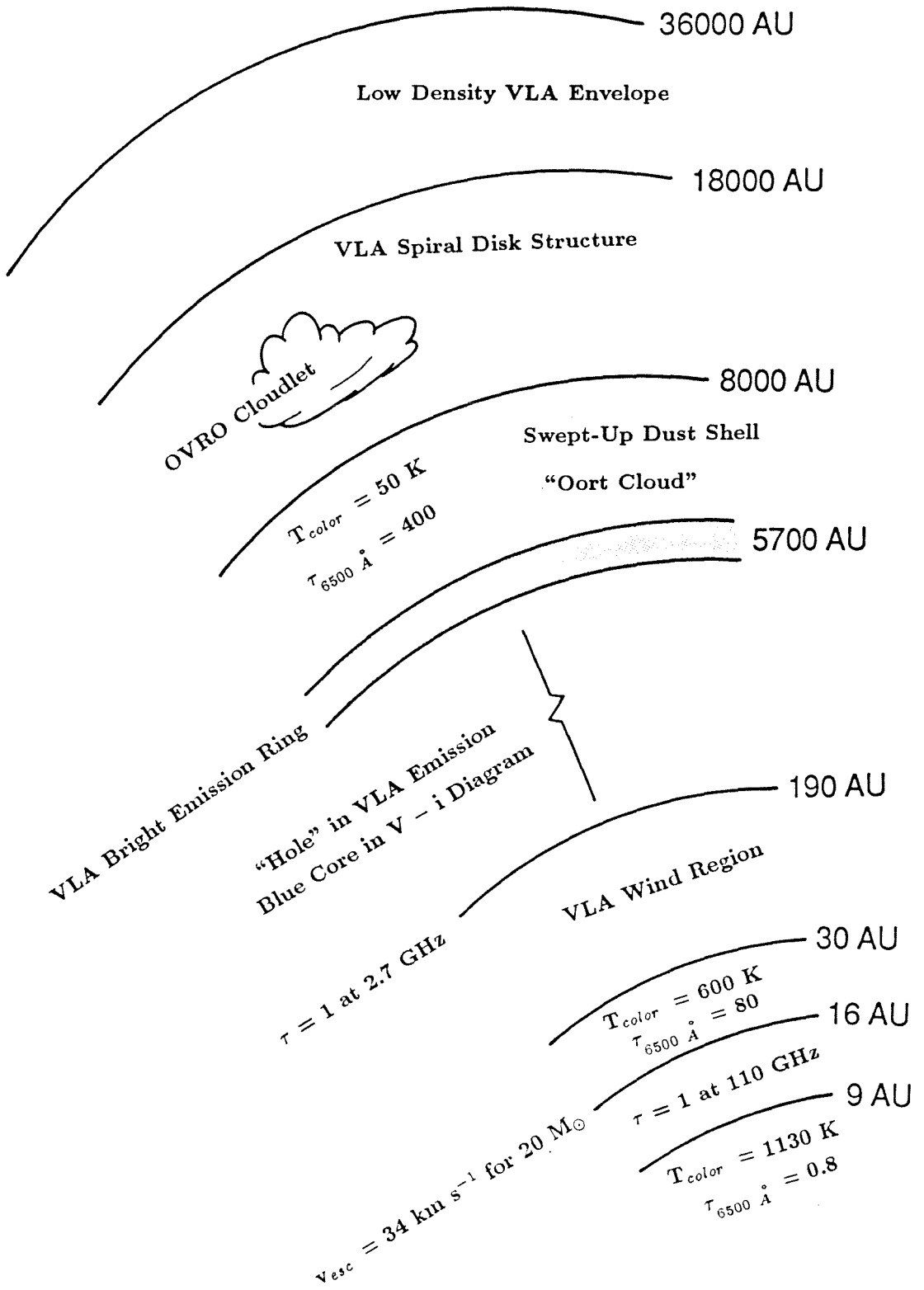

IV. S106

IV. A. INTRODUCTION

The striking bipolar HII region, S106, is bisected by an equatorial gap devoid of much emission. This source has recently been the object of a great deal of interest, both because of its suspected relation to the high velocity bipolar molecular outflows (Bally and Lada 1983) and because its morphology suggests the existence of a disk surrounding its centrally located, highly obscured, exciting source, the young stellar object, IRS 3. Many investigations were launched in order to detect a hypothesized, edge-on disk structure in S106. The detection of such a disk would at once provide a simple explanation for the object's bipolar structure, and the first direct evidence for a *star-forming* accretion disk. New, high-resolution molecular line images of S106, obtained with the Owens Valley Radio Observatory's millimeter array, are presented in this work, with intriguing results. But first, let us review our current state of knowledge of this source.

S106 was discovered over forty years ago (Minkowski 1946). Its name derives from being the 106th entry in a catalog of HII regions gleaned from the first Palomar Sky Survey (Sharpless 1959). Since that time, over a hundred articles on S106 have appeared, encompassing observations from the radio, submillimeter, millimeter, infrared, and optical wavelength ranges.

A spectacular 5 GHz radio map of the two emission lobes of S106 shows that the strongest emission originates from the lobe *edges* and that the HII gas distribution is highly irregular and filamentary (Bally, Snell, and Predmore 1983). The mass of ionized gas from this VLA image is estimated to be in the range $0.06 < M_{ionized} < 0.25\ M_{\odot}$. Although at optical frequencies the southern lobe is significantly brighter than the northern lobe, at 5 GHz each lobe contributes equally to the observed flux, supporting the idea that the nebula is tilted into its parent molecular cloud towards the north and out of the cloud to

the south of the central point source, hereinafter referred to as S106 IR. The kinematic structure derived from optical spectroscopy supports this geometrical model, since the northern lobe has an average red-shift of 20 km sec^{-1}, while the southern lobe has an average blue-shift of -40 km sec^{-1} (Solf and Carsenty 1982).

In addition to the differing average Doppler shifts of the two lobes, the southern lobe of S106 exhibits line splitting between components of up to 100 km s^{-1}, characteristic of a supersonically expanding, optically thin shell. Because an ionization-driven flow cannot account for linewidths as large as 220 km s^{-1}, such as are observed in some lobe locations, a stellar wind model was invoked to explain the observations (Barral and Cantó 1981).

The nebula itself is embedded in a 3300 $M_\odot$ molecular cloud of 20′ E-W and 25′ N-S extent, corresponding to an average radius of 1.8 pc, assuming a terrestrial $CO/^{13}CO$ ratio, and a distance of 600 pc (Lucas *et al.* 1978). Subsequent higher-resolution studies of the molecular cloud revealed a chaotic velocity structure and complex morphology (Bally and Scoville 1982). These authors estimated the mass contained within the central 16′ × 16′ to be 1200 $M_\odot$.

A reliable distance to S106 was determined only a decade ago from photometry. Earlier attempts at a kinematic distance determination were unreliable, since S106 has a V_{LSR} of -1.0 km sec^{-1} (Bally 1981). From a photometric study of S106 IR, the best-fit curve to the observed energy distribution gives a distance of 500 ± 200 pc, for a visual extinction of 21 magnitudes toward an embedded source of spectral type between B0 and O5, for luminosity Class V, or between O9 and B0, for luminosity Class Ia (Eiroa *et al.* 1979). An independent study, based on UBVRI photometry of field stars, revealed an abrupt increase in A_V at a distance of 600 ± 100 pc (Staude *et al.* 1982). This latter method has the advantage that the derived distance is source model-independent.

Therefore, unless otherwise stated, all calculations in this work are carried out with the adopted value of 600 pc as the distance to S106.

Disks of differing sizes and masses have been proposed in order to explain the bipolar morphology of S106 in the optical, infrared, and radio. Inconsistencies among and within these various disk models abound.

The first suggestion of a disk in S106 was made on the basis of the differential extinction between its two lobes, the high extinction towards S106 IR, and the bipolar appearance of the nebula (Sibille *et al.* 1975). A quantitative calculation modelling S106 as a disk-constrained HII region can qualitatively reproduce the observed Hα and radio emission morphologies, but this same model predicts an infrared morphology, which is in direct conflict with observation. The predicted infrared structure is a centrally condensed, flattened object, with its major axis perpendicular to that of the bipolar nebula (Kandel and Sibille 1978). The actual infrared morphology is much like that seen in the optical and radio, such that an emission *minimum* is found between the two lobes (Gehrz *et al.* 1982).

Another proposed disk structure was based on CO observations of the S106 molecular cloud, made at 45″ resolution. This purported disk has an angular extent of 2.5′ × 6′, and a mass of 100 $M_\odot$ (Bally and Scoville 1982). Although subsequent observations of NH_3 at 40″ resolution confirmed the CO spatial structure of the molecular environs of S106, no indications of rotation were found (Stutzki, Ungerechts, and Winnewisser 1982).

A scaled-down disk was suggested next, being inferred from VLA observations of diminished ionized gas column density in the 3′ × 20″ strip bisecting S106. This putative disk was estimated to contain only 0.01 $M_\odot$ of material (Bally, Snell, and Predmore 1983). Aperture synthesis maps of HCN emission at 13″ resolution revealed two emission peaks on either side of S106 IR. This structure was interpreted as a disk of diameter 33″,

thickness $< 7''$, and mass $< 2\ M_{\odot}$. If the velocity gradient across the observed HCN structure is attributed to rotation, the rotation period is 2×10^6 years (Bieging 1984).

The dark lane between the northern and southern lobe as seen in the optical has been attributed to large-scale extinction, such as would be provided by a disk structure, although extinction effects cannot explain the persistence of this gap in the radio. It has been noted, however, that the equatorial gap is much narrower at 10 μm, 20 μm, and 1.3 cm, than in the optical. On this basis, Felli *et al.* 1984 attribute the bipolarity of S106 to the structure of the dense, ionized, mass-loss envelope of the central star, *i.e.*, to conditions in the immediate environs of S106 IR ($r \leq 10$ AU). In fact, recent observations of the CaII triplet toward S106 IR have been interpreted as arising from a 6 AU diameter Keplerian disk or ring of very dense gas ($n_H = 10^{13}$ cm^{-3}) (Persson, McGregor, and Campbell 1988).

The exciting star of the nebula was first detected by photometric measurements in the 1.25–3.4 μm wavelength range (Sibille *et al.* 1975). In a 3.5 μm survey of the region with a $12''$ aperture, the exciting star is designated as IRS 3 (Pipher *et al.* 1976). The other three newly discovered 3.5 μm sources are extended, and identified as compact HII regions, based on their coincidence with 2.7 GHz radio continuum emission. In a subsequent infrared study (Gehrz *et al.* 1982), carried out at 3.6 μm, 10 μm, and 19.5 μm with $5''$ resolution, the same star is named IRS 4. Optical and infrared polarization studies of the brightest emission regions support the hypothesis that this source is responsible for the excitation of the entire nebula (Dyck and Lonsdale 1979; Perkins, King, and Scarrott 1981; Tokunaga, Lebofsky, and Rieke 1981; Staude *et al.* 1982). This 3.5 μm source coincides with the VLA point source lying in the emission gap between the two lobes, and will hereafter be referred to as S106 IR.

Several authors have made independent determinations of the visual extinction and

spectral type of S106 IR. Comparison of the flux in the [OIII] lines at 4959 Å and 5007 Å with model calculations indicates that the effective temperature of the exciting star is in the range 30,000 K $< T_{eff} <$ 35,000 K (Staude *et al.* 1982). This is consistent with S106 IR's being an O9 V star. Integration of the emitted flux of S106 IR in the 3.6–12.6 μm range gives a luminosity consistent with a ZAMS star of spectral type O7–O9 (Gehrz *et al.* 1982). From the Hβ to 4861 Å continuum flux ratio, an effective temperature of 35000 K, corresponding to a spectral type of O9 V, is derived (Calvet and Cohen 1978). The extinction toward S106 IR derived from the Brα/Brγ ratio is 11 mag $< A_V <$ 33 mag (Tokunaga and Thompson 1979). Extinction values in the range A_V = 6–14 have been derived from the Hα/1.3 cm continuum flux ratio from 13 different positions in the emission nebula (Felli *et al.* 1984). In this same study, the extinction towards S106 IR in a 7″ aperture is A_V = 10.4 mag. These authors claim that their value could be consistent with the previous determination of A_V = 21 mag (Eiroa *et al.* 1979), if the extinction in their aperture is highly variable, *i.e.*, if the extended stellar mass loss envelope suffers less extinction than the stellar photosphere. Therefore, if half the extinction to S106 IR is located within a few thousand AU of the central star, both determinations of the visual extinction are correct. Such variable extinction at small scales could also explain the HII region morphology.

It has been mentioned previously that because an ionization driven flow cannot attain the high velocities encountered in the optical emission lobes of S106, a stellar wind was invoked to accelerate the lobe gas. The idea that S106 IR is the source of this powerful stellar wind, which, in turn, has shaped the observed optical and radio emission structure, was first put on a firm observational footing by optical, long-slit spectroscopy (Hippelein and Münch 1981; Solf and Carsenty 1982). Furthermore, between 5 GHz and 22 GHz, the radio spectral index of S106 IR is 0.73 (Bally, Snell, and Predmore 1983), as predicted for

emission from an ionized, isotropic, steady stellar wind (Panagia and Felli 1975; Wright and Barlow 1975). By equating the mass flow through an annulus of radius 2×10^{17} cm, thickness 5×10^{15} cm, gas density 10^4 cm^{-3}, and velocity, v = 50 km s^{-1} in the southern lobe, the mass-loss rate from S106 IR is estimated at 2×10^{-5} $M_\odot$ yr^{-1}, and the wind velocity at 220 km s^{-1} (Hippelein and Münch 1981). These authors note that their derived mass loss rate is a factor of 10 higher, and wind velocity a factor of 5 lower, than what is typical for main sequence stars of S106 IR's spectral type.

The aim of the present study is to gain a new understanding of the gas dynamics and morphology of S106. To this end, single-dish and interferometer observations were undertaken, resulting in the highest-resolution, millimeter maps of S106 currently available. These data are supplemented by images of S106 from IRAS, and by new broad-band, optical CCD imaging and photometry. Observations and data reduction are described in § IV. B. The observational results are presented in § IV. C., followed by the discussion in § IV. D., and the conclusions in § IV. E.

IV. B. OBSERVATIONS

1) Optical

Broadband images of S106 and the surrounding region were taken on the Palomar 1.5 m telescope on the night of 25 June 1987. The transparency was good and the seeing was better than 1.2″. The sky brightness was 21.1 mag arcsec^{-2} at 6500 Å. The detector was an RCA CCD with 320 × 512 pixels. Reimaging optics were used to provide sufficient field coverage of the nebulosity surrounding S106. The scale was 1.23″/pixel, resulting in a 6.6′ × 10.5′ field.

As discussed in the previous chapter, the filter system at the 1.5 meter telescope consists of pseudo-Johnson B, Johnson V, Gunn r, and Gunn i. This filter set has effective wavelengths of 4200 Å, 5400 Å, 6700 Å, and 8000 Å. Exposure times were 1200 seconds

for B, and 600 seconds each for the V, r, and i filters. Standards were taken from Landolt (1983) and transformed onto the Gunn system.

The software package ARCHANGEL was used for reduction of the raw CCD data. The first step was erase-level subtraction, the erase level being determined from 50 lines of overscan taken after each frame was read out. For exposures longer than 5 minutes, it was also necessary to subtract a dark frame of equal duration to remove noise from a hot amplifier in the upper (south) half of the CCD. These dark frames were collected during the daylight hours, and consist of averages of 10 for each exposure time. Flat fields were obtained from dome-illuminated, short exposures taken at least five times during the night, and flattening was good to the 0.5% level. Masks were applied to flattened data to flag one bad column and two regions of depressed chip sensitivity. Regions for sky determination were located interactively on a color graphics display. These regions consisted of several boxes of 20 × 20 pixels distributed symmetrically around the object of interest. Finally, the frames were cleaned of cosmic rays, and data from the single bad column in the chip were interpolated between data values in neighboring columns.

The photometry presented here will be for the filter system in which the data were acquired. Exposure times were between 600 to 1200 seconds; however, several short exposures in V and r were obtained since the central nebula was saturated in the longer exposures. All exposures were taken with airmass values less than 1.04. The photometry for the central object in S106 was done using 5″ circular apertures. However, there is a large amount of nebulosity surrounding this central region. The choice of a 5″ diameter is a compromise between minimizing the amount of light from extended emission and maximizing the light of the stellar image. This constraint is the primary source of error in the optical brightness determination of the central source.

2) IRAS

IRAS Survey Data were coadded for 43 passes of the satellite over the S106 region. The fluxes for S106 determined from the point source filtered FLUX grids were corrected for detector non-linearities, errors that were due to coadd processing, and sampling and position uncertainties. Color corrections were not applied. (See *IPAC User's Guide 1986*). Fluxes of the extended emission region, surrounding S106 over a $30' \times 30'$ area, were obtained from the Coadd Intensity Grids after background level subtraction. An average radial profile of the emission intensity was constructed in each of the four IRAS bands by fitting ellipses to the data. Each ellipse has four free parameters; x and y center, eccentricity, and position angle. The profile fitting program, PROF (a GASP subroutine), expands the parameters of the initial ellipse into a Fourier series and then iterates the coefficients for a best fit by least-squares error minimization. Within the errors, there was no significant change in position angle, eccentricity or centroid across S106. Intensity values were sampled in equal logarithmic steps of the radial coordinate.

3) Molecular Lines

a) FCRAO

S106 was observed in the J=1→0 transition of both ^{13}CO and CO on the 9th and 10th of June, 1986, respectively, with the Five College Radio Astronomy Observatory (FCRAO) 14 m radio telescope. The HPBW at these frequencies is 45″. The map center coordinates for these observations were those of the VLA central point source: $\alpha_{1950} = 20^h25^m33.8^s, \delta_{1950} = 37°12'48.0''$. Spectra were obtained by position-switching to $\alpha_{1950} = 20^h26^m02^s, \delta_{1950} = 36°45'44''$, a region devoid of molecular emission. Typical system temperatures during the observations were 674 K at CO and 575 K at ^{13}CO. Maps of the molecular emission centered on S106 were obtained over a 9 × 9 element grid, sampled every 15″. Total on-source integration times at each position were 15 seconds at CO and 75 seconds at ^{13}CO. An ambient temperature load was inserted in the

beam every 6 minutes for data calibration. The velocity resolution of these observations is 0.27 km/sec (100 kHz) over a ± 35 km s^{-1} range, centered at $V_{LSR} = -1.0$ km s^{-1}.

The data reduction program SPA (Spectral Analysis) was used to produce maps of the molecular emission, excitation temperature, and gas column density in the $2' \times 2'$ region centered on S106 IR. Raw data were corrected for atmospheric and forward scattering losses ($\eta_{fss} = 0.72$), but not for the source beam coupling efficiency.

b) OVRO

S106 was observed with the Owens Valley Radio Observatory 3-element interferometer. Observations in the 97.981 GHz (J=2→1) transition of CS, and its adjacent continuum, were obtained in the Spring of 1985. Continuum and line observations at ^{13}CO (J=1→0), 110.271 GHz, were made during both the 1985-86 and 1986-87 observing seasons. W3(OH) was the primary flux calibrator for both sets of observations, with an adopted flux density of 4.0 Jy. The phase calibrator, 2021+317, was observed every 20 minutes. Resulting synthesized beams (HPBW) were $7.9'' \times 4.6''$, p.a. 8.7° and $7.0'' \times 5.8''$, p.a. 0.3°, for the CS and ^{13}CO observations, respectively. The spectral resolution of the CS observations is 3.06 km s^{-1}, over a 98 km s^{-1} bandpass, while that of the ^{13}CO observations is 0.136 km s^{-1}, over the central 4.35 km s^{-1}. The central velocity, in both instances, is -1.0 km s^{-1}, V_{LSR}. Further observational data are listed in Table IV.1. The data were calibrated with the MINT (Millimeter Interferometer) Software Package, and final maps were produced by the "MX" routine of the Astronomical Image Processing System (AIPS).

IV. C. RESULTS

1) Optical

For reference, an optical Gunn r CCD frame of S106 is presented in Figure IV.1. The central nebulosity has a bipolar appearance, with the southern lobe's surface brightness

surpassing that of the northern lobe by up to a factor of 40. There is a great deal of jumbled, filamentary structure apparent in the lower surface brightness regions of the nebula, which is hard to see in reproduction. The central source, midway between the lobes and appearing as the point source in the VLA 1.3 cm image, has $m_V = 17.75$, $m_r = 15.92$, and $m_i = 14.75$, inside a 5″ diameter aperture. It must be borne in mind, however, that these figures include contributions from both scattered light and nebular emission. The central object is reputed to be a star of spectral type O9, suffering 21 magnitudes of visual extinction.

Cross sections of the nebular surface brightness and V−i color, taken along the symmetry axis of the bipolar nebula (at p.a. = 150°) and passing through S106 IR, are shown in Figures IV.2a and IV.2b, respectively. The cross section depicted in Figure IV.2a shows a broad range in surface brightness (peaks of 18.5 r mag arcsec^{-2} and troughs of 22, 23, and 24 r mag arcsec^{-2}). The irregularity of the surface brightness curve is a reflection of the inherent filamentary structure of the nebula. The central object, S106 IR, shows up as a slight "bump" superimposed on the general, downward, surface-brightness plunge of the southern lobe. Any thin, obscuring dust lane in the environs of S106 IR ought to show up as a dramatic depression in surface brightness surrounding the central object. However, if such a disk structure exists, it must be thinner than 1.2″, the resolution element of these observations. Turning our attention to Figure IV.2b, which has 2.5″ resolution along its spatial coordinate, note the "notch" in V−i color at the position of S106 IR, indicating its blueness relative to its surroundings. S106 IR lies on a red plateau in V−i color, indicating somewhat higher reddening within a 40″ band in its immediate vicinity, than on a scale twice this size.

2) IRAS

Coadd images of the S106 field in the four IRAS bands are shown in Figure IV.3.

Although the optical bipolar nebulosity lies within a $5' \times 7'$ field, the far-infrared emission encompasses a 465 square arcminute area. The total fluxes from this region are 944 Jy at 12 μm, 3870 Jy at 25 μm, 19100 Jy at 60 μm, and 33900 Jy at 100 μm. The point source filtered Coadd FLUX grids give fluxes of 194 Jy at 12 μm, 2110 Jy at 25 μm, 10340 Jy at 60 μm, and 11800 Jy at 100 μm at the position of S106 IR.

Figure IV.4 shows the azimuthally averaged radial profiles of the intensity maps of the previous figure. Departures from a straight line among the plotted data points can be attributed to the presence of far-infrared sources in the area, other than S106 IR. Within the errors, the best-fit slope to the data in all four IRAS bands is consistent with an r^{-3} falloff of the dust emission strength from its peak at S106. In each IRAS band, the location of peak emission is positionally coincident with S106, showing it to be the chief heating source of the surrounding molecular cloud. The color temperature of the dust as a function of radius is remarkably constant in this source. The radial dependence of both the color temperature and the dust emission strength of the S106 cloud is similar to what was found for the clouds containing S87 and LkHα101.

Figure IV.5 shows the spectral energy distribution of S106. The model curve is a sum of two components. The first of these has T_d = 920 K, $\tau_{250\mu m} = 10^{-4}$, and $\theta = 0.65''$ ($d\Omega = \frac{\pi\theta^2}{2}$), with wavelength-independent opacity. The second component has T_d = 60 K, $\tau_{250\mu m} = 0.01$, and a $60''$ radius, with opacity scaling as λ^{-1} for $\lambda < 250$ μm, and as λ^{-2} for $\lambda > 250$ μm. Assuming a distance of 600 pc to S106, integration under this curve gives a total luminosity of 1.3×10^4 $L_\odot$, compared with the previous determination of 1.1×10^4 $L_\odot$ using the IRAS Point Source Catalog fluxes (Mozurkewich *et al.* 1986). Other luminosity determinations for S106 have been in the range 1.2–2.0 $\times$ 10^4 $L_\odot$ (Campbell *et al.* 1982; Harvey *et al.* 1982; Chini *et al.* 1984).

3) FCRAO

Single-dish maps of the CO and ^{13}CO emission, integrated over all velocities, are presented in Figures IV.6a and IV.6b, respectively. Figure IV.6c represents a map of the peak CO excitation temperature over the same area. The range in excitation temperatures is 20→25 K. Note how well the contours of depressed excitation temperature correspond with the overall optical appearance of the nebula. There is a clear, spatial anticorrelation between the regions of highest CO excitation temperature and the hot, ionized gas of the optical nebula. This is to be expected, if the ionization is eating into the molecular cloud and the neutral gas on the surface is heated either mechanically or by photons from the HII region.

The column density map of Figure IV.6d presents a completely different picture. The peak in column density is clearly offset from the central source by 1′ (36000 AU at 600 pc). The column densities in this region of the cloud vary by a factor of three on the scale of an FCRAO beam (45″) from 2.2 × 10^{22} to 6.7 × 10^{22} H_2/cm^{-2}. At the position of S106 IR, the molecular column density of 3.6 × 10^{22} H_2/cm^{-2} corresponds to an A_V = 24 mag, assuming N_{H_2}/A_V = 1.5 × 10^{21} cm^{-2}. This is to be compared with the previous determination of A_V = 21 mag (Eiroa *et al.* 1979). The total mass of molecular gas in the area, derived from this column density map, is 135 $M_\odot$. The "virial mass," for a density distribution $\rho(r) \propto r^{-2}$,

$$M_{virial} = \sigma^2 R/G$$

is 1400 $M_\odot$ in the FCRAO field, for σ_v = 5 km s^{-1}, and R = 1.4′ at 600 pc.

CO line emission in the S106 field was detected only over a 10 km s^{-1} FWZI velocity range about the cloud rest velocity at 1 km s^{-1} V_{LSR}. Note the lack of clear spatial separation between the red and blue "wing" emission peaks in Figure IV.7. The emission from each wing exhibits several peaks over the mapped area. Thus, there is no evidence for any "bipolar molecular outflow" in this source.

4) OVRO

High-resolution, interferometric maps of the integrated molecular line emission in S106 are presented in Figure IV.8. The angular resolution of the ^{13}CO and 110 GHz continuum maps is $7'' \times 5.8''$. The ^{13}CO map covers the central 4.4 km s^{-1} in velocity. The beam shape for these observations is depicted at the top left of the 110 GHz continuum map. The angular resolution of the CS map is $8'' \times 4.5''$, and covers the central 98 km s^{-1} in velocity. The HCN map has a resolution of $11'' \times 13''$ and covers 256 km s^{-1} in velocity. Note that the ^{13}CO and CS observations from this work clearly resolve the two maxima apparent in the HCN emission.

The OVRO 110 GHz continuum map of S106 is presented in Figure IV.8. The strongest continuum source is located at $\alpha_{1950} = 20^h25^m32.794^s$, $\delta_{1950} = 37°12'45.0''$, and has a flux of 0.56 Jy at 110 GHz. This strong continuum source coincides spatially with the far infrared source S106/IRS3 (Gehrz *et al.* 1982). The integrated flux of the entire emitting region is 2.2 Jy at 110 GHz. This is to be compared with a value of 11 Jy at 1.3 cm (Felli *et al.* 1984).

Figure IV.9 shows the small-scale structure of the ^{13}CO line emission at high velocity resolution near the cloud rest velocity of -1.0 km s^{-1}. Most of the observed emission originates from molecular gas bordering the bipolar HII region (see Figure IV.11). Note the distinct lack of emission across the region containing the VLA point source. A 3σ upper limit on the column density of any small-scale ($\approx 5''$) molecular structure at the radio point source position at the cloud rest velocity is $N_{H_2} = 1.2 \times 10^{21}$ cm^{-2} for $T_{ex} =$ 20 K. We have shown above, using the cross-sectional cut of the Gunn r surface brightness distribution, that any disk structure must be thinner than $1.2''$. The width of the gap between the two radio lobes is $30''$. Thus, if we take a projected area for the putative disk to be $30'' \times 1''$, the observed upper limit in column density is equivalent to a mass upper

limit of 7×10^{-3} $M_\odot$ at 600 pc. The total observed mass in the ^{13}CO interferometer maps is 2.7 $M_\odot$. The gas to the east of the central object comprises 1.7 $M_\odot$, and the remaining 1 $M_\odot$ is to the west of the central source. The single-dish observations detected 16 $M_\odot$ over the same area, indicating the interferometric observations recover only 17% of the available flux, most of which resides in large scale structures ($\geq 30''$).

The CS interferometer maps of Figure IV.10 cover a greater range in velocity than the ^{13}CO maps of Figure IV.9. In Figure IV.10, the signature of a rotating structure would be to have the highest-velocity blue- and red-shifted peaks closest in to the VLA point source, on opposite sides of it, with progressively lower magnitude blue- and red-shifted peaks farther out from the central object, for a Keplerian disk. Furthermore, at the cloud rest velocity, we should see emission overlapping the central source, since this would signal the presence of tangentially moving gas. As in the ^{13}CO maps of the previous figure, such tangentially moving gas remains undetected in the CS observations as well.

IV. D. DISCUSSION

1) Large-Scale Structure

Figure IV.4 shows the large-scale, radial intensity distribution of emission from the S106 molecular cloud in each of the four IRAS bands. The solid line in the upper right-hand corner of this figure shows the fit for an r^{-3} dependence, and agrees with the observations quite well. Note that geometric dilution of the central source's radiation field would produce an r^{-2} radial intensity falloff. The observed r^{-3} dependence suggests an additional effect that is due to an r^{-1} dust *surface* density variation, and, therefore, an r^{-2} dependence of dust density with radius. The IRAS maps of Figure IV.3 all show a *centrally peaked* dust cloud. An increase in gas density, going into the cloud radially towards S106, can be deduced from the molecular-line-map mass estimates made at varying spatial scales. The results are in Table IV.2, and show a general increase in the *average* cloud

gas density from 10^3 cm^{-3} at the cloud periphery to 10^5 cm^{-3} in the immediate vicinity of the bipolar nebula.

An ordered, large-scale *molecular* outflow, powered by S106 IR, is ruled out by the present observations. As previously mentioned, there is no clear spatial separation of blue- and red-shifted line emission about the central source (see Figure IV.7). The spatial distribution and kinematics of the molecular gas are, however, indicative of a chaotic, supersonically turbulent medium.

2) No Molecular Gas Disk

If the molecular emission from S106 were to originate from a nearly edge-on disk structure, then the OVRO observations should show an emission maximum centered at the position of the radio emission gap. The fact that just the opposite is observed, *i.e.*, that a molecular emission *minimum* is found at this position, is the strongest argument against the existence of the previously posited molecular gas disk. Figure IV.11 shows an overlay of the integrated CS emission, generated from OVRO data, superposed on the VLA 23 GHz continuum map. The central point source is S106 IR. Note the pronounced lack of molecular emission over most of the radio gap. From the integrated ^{13}CO emission of Figure IV.8b, a firm upper limit of 0.01 $M_\odot$ has been set for any undetected, molecular gas structure (see § III).

What we *do* observe are molecular gas clumps on either side of the ionized gas lobes. Comparison of previous observations with the new OVRO data shows that the northeastern CS extension coincides with the densest NH_3 clumps in the field, as well as with an identical structure found in HCN (Bally 1985; Bieging 1984). Maps of the visual extinction in the northern lobe are similar to the interferometer maps and show an increase in extinction from west to east. The location of the eastern CS condensation and the visual

extinction maximum coincide (Felli *et al.* 1984). The other CS condensation of Figure IV.11 is displaced to the northwest of the southern continuum lobe's western peak.

There is evidence that both these condensations are mostly in front of the ionized gas. Figure IV.9 shows that most of the emission from the western CS clump is blue-shifted gas, while the eastern CS clump is seen in absorption in H_2CO (Bally 1985). Furthermore, the agreement between the extinction maps derived from the [SIII] 9532 Å/1.3 cm continuum and the Hα 6563 Å/1.3 cm continuum ratios leads to the conclusion that the dust lies in front of the ionized gas. Otherwise, we would expect an increase in the derived A_V values with wavelength (Felli *et al.* 1984).

The hot, tenuous, ionized gas of the optical and radio lobes seems to be sweeping up the surrounding cold, dense, molecular gas and dust. The eastern edge of the HII region bends 45° to the west from the original flow direction right at the position of the eastern CS clump, giving the appearance that the ambient molecular gas deflected the supersonic, ionized gas flow. In S106, the strongest H_2 (2.122 μm) emission, which indicates shock-excited gas, originates from this region as well (Longmore *et al.* 1986). For a source model consisting of radial flow centered on S106 IR, and tangential flow along the cavity walls defined by the ionized gas lobes, we would expect to see the CS emission peaks at successively smaller blue-shifts at successively greater distances from S106 IR, just as seen in Figure IV.10.

The differences between the gas spatial distributions apparent upon comparison of the OVRO CS and ^{13}CO data and the Hat Creek HCN data are entirely accounted for by resolution effects (see Figure IV.8). The OVRO observations resolve the previously partially resolved, eastern and western condensations. This increased resolution is critical in ascertaining the lack of H_2 gas between the condensations, indicating the absence of a molecular gas disk.

Besides morphology, the previous line of argument favoring the presence of a molecular disk was based upon the HCN velocity data. Assuming that the apparent shift in HCN emission centroid with velocity is real, the deduced gradient of 0.08 km s^{-1} $arcsec^{-1}$ along an E-W line joining the emission peaks with S106 IR corresponds to a 2×10^6 year, disk-rotation period. However, the velocity resolution of the HCN observations was 4 km s^{-1}, such that the main line and hyperfine HCN emission components could be confused, making any kinematic interpretation of the data highly doubtful. The velocity resolution of the OVRO ^{13}CO observations was 0.14 km s^{-1}, and no evidence for the previously reported gradient was found. Rather, the combined CS and ^{13}CO velocity data show *decreasing* radial velocities with increasing distance from S106 IR, consistent with interpreting the data as large condensations of swept-up molecular material, which, in turn, constrain the motion of the expanding ionized gas lobes.

3) Evolutionary Stage

Estimates of the age of S106 IR may be made by choosing plausible assumptions regarding the nature of the material surrounding the central star.

Previous studies strongly imply that S106 IR provides the kinetic energy and ionization for the bipolar nebula. The radio spectral index of S106 IR is 0.73, in agreement with that predicted for a fully ionized stellar wind. Given the radio flux, S_ν, at a frequency, ν, we may determine the mass-loss rate in the wind from (Panagia and Felli 1975):

$$\frac{S_\nu}{mJy} = 2.0 \times 10^{10} \left(\frac{\nu}{GHz}\right)^{0.6} \left(\frac{T_e}{^oK}\right)^{0.1} \left(\frac{\dot{M}}{M_\odot\ yr^{-1}}\right)^{4/3} \left(\frac{v}{kms^{-1}}\right)^{-4/3} \frac{1}{D_{kpc}^2}.$$

Observed values for the flux at 5, 15, and 23 GHz are 5.4±0.2 mJy, 12.3±0.9 mJy, and 17±2 mJy, respectively (Bally, Snell, and Predmore 1983; Felli *et al.* 1984). For T_e = 10^4 K, D = 0.6 kpc, and v = 220 km s^{-1}, the mass loss rate is 1.7×10^{-6} $M_\odot$ yr^{-1}. This value is to be compared with the determination of 2.4×10^{-5} $M_\odot$ yr^{-1} from optical data

(Hippelein and Münch 1981). Since the radio determination requires fewer assumptions and is more consistent with typical OB star mass loss rates, we adopt the lower mass-loss-rate value for subsequent calculations in this work.

If we assume that the entire mass of the present ionized lobes originated from S106 IR, then $M/\dot{M}$ is 3.5×10^4 yrs $< t < 1.5 \times 10^5$ yrs for $0.06\ M_\odot < M_{lobe} < 0.25\ M_\odot$. If only some fraction of the lobe mass originates from the stellar wind, then this derived time scale is an upper limit to the length of time for which the central source has been losing mass. The other alternative is to assume that most of the lobe mass is swept-up material. For simplicity, let us assume an isotropic wind flowing into a medium of constant density, n_o. After a time, t, a thin spherical shell of ambient gas is formed at radius $r_s(t)$. We may determine the age of the shell from (Castor, McCray, and Weaver 1975):

$$\frac{r_s(t)}{pc} = 28\left(\frac{\dot{M}_w}{10^{-6} M_\odot\ yr^{-1}}\right)^{1/5}\left(\frac{v_w^2}{2000\ km\ s^{-1}}\right)^{1/5}\left(\frac{n_o}{cm^{-3}}\right)^{-1/5}\left(\frac{t}{10^6\ yr}\right)^{3/5}.$$

Taking the radius of the shell as 0.175 pc (1′ at 600 pc), $\dot{M}_w$ as determined above, assuming the original gas density to be that currently found at the cloud periphery, $n_o = 10^3$ cm^{-3}, and $v_w = 220$ km s^{-1}, gives an age of 7.7×10^3 years. This is a lower limit to the true age, since no allowance has been made for wind deceleration by ambient dense material, as observed.

Another age estimate may be deduced from energy considerations. A fair estimate of the total kinetic energy in the molecular gas surrounding S106 is $1/2\ M_{total} < v_{avg}^2 >$. Using 2.5 km s^{-1} for the average gas velocity, and the 135 $M_\odot$ observed in the FCRAO field, yields a value for the kinetic energy of 1.7×10^{46} ergs. The kinetic power of the S106 wind is $1/2\ \dot{M} v_w^2$, or 2.6×10^{34} ergs s^{-1}. If the wind power is assumed constant, the estimated wind lifetime is 20,000 years. The time scale for turbulent energy dissipation is of the order l/v, where l is the linear dimension of a turbulent eddy, and v is the typical

gas velocity, taken to be 2.5 km s^{-1}. The choice of length scale is problematic, since observations show turbulent gas motions on many different scales. For structures the size of the CS and ^{13}CO condensations ($\approx 10''$), this dissipation time scale is 10^4 years.

With regard to the foregoing discussion, the best estimate for the age of S106 IR is in the range $1.0 \times 10^4 < t < 5.0 \times 10^4$ years, in agreement with the other age determinations.

With regard to the foregoing discussion, the best estimate for the age of S106 IR is in the range $7.7 \times 10^3 < t < 1.5 \times 10^5$ years.

IV. E. SUMMARY

Combined IRAS and millimeter-line observations of the massive molecular cloud containing S106 offer convincing evidence for a *large-scale* (0.2 pc < r < 7 pc), centrally peaked density enhancement in the cloud, centered on S106 IR. The central cloud gas density is on the average a factor of 100 higher than that found at the cloud periphery. The dust density distribution varies as r^{-2} with radius.

Although no coherent *molecular* outflow is observed in this source, the powerful stellar wind of the young, pre-main-sequence star, S106 IR, may be responsible for the observed supersonic turbulence. The current best estimate for the age of the S106 HII region is 10,000–50,000 years.

The present, high-resolution millimeter interferometer line observations reveal that the molecular gas in the immediate vicinity (< 0.2 pc) of the bipolar nebula consists of swept-up, ambient cloud material. There is no evidence for the presence of a dense, molecular gas disk, which had been reported previously. Rather, the present observations are consistent with the model of Felli *et al.* 1984, in which the bipolar structure is due to anisotropic conditions in the immediate vicinity (<< 90 AU) of S106 IR. Recent spectroscopy of the CaII triplet lines points to the same conclusion (Persson *et al.* 1988).

TABLE IV.1

OVRO Observational Parameters

Molecule	Filterbank	Configuration			Date	LST Range
CS	32×1MHz	10E	10W	20N	1985 APR 28	14:45–15:139
		30E	50W	00N	1985 MAY 09	14:00–02:00
		50E	50W	10W	1985 MAY 25	16:15–01:18
		50E	50W	10W	1985 MAY 31	15:17–16:07
		50E	50W	10W	1985 JUN 02	14:07–22:58
^{13}CO	32 × 50kHz	10E	10W	20N	1985 DEC 10	14:24-02:52
		10E	10W	20N	1985 DEC 14	21:18–02:13
		30E	20W	00W	1986 JAN 06	23:58–02:48
		10W	65W	50W	1986 FEB 27	16:12–03:42
		30E	40N	30W	1986 MAR 24	14:10–22:05
		30E	60N	30W	1987 FEB 03	17:00–01:00

TABLE IV.2

S106 MASS ESTIMATES

MASS ($M_\odot$)	RADIUS (ARCMIN)	ρ (N_{H_2} CM^{-3})	REFERENCE
3300	22.4	1.1×10^3	Lucas *et al.* 1978
1600	16	1.5×10^3	Bally and Scoville 1982
135	2.25	4.5×10^4	this work
16	0.75	1.4×10^5	this work

REFERENCES

Bally, J. 1981, Ph.D. thesis, University of Massachusetts at Amherst.

Bally, J. 1985, private communication.

Bally, J. and Lada, C. 1983, *Ap. J.*, **265**, 824.

Bally, J., and Scoville, N. Z. 1982, *Ap. J.*, **255**, 497.

Bally, J.; Snell, R. L.; Predmore, R. 1983, *Ap. J.*, **272**, 154.

Barral, J. F. and Cantó, J. 1981, *Rev. Mexicana Astron. Astrof.*, **5**, 101.

Bieging, J. H. 1984, *Ap. J.*, **286**, 591.

Calvet, N. and Cohen, M. 1978, *M.N.R.A.S.*, **182**, 687.

Campbell, M. F.; Hoffmann, W. F.; Thronson, Jr., H. A.; Niles, D.; Nawfel, R.; Hawrylcz, M. 1982, *Ap. J.*, **261**, 550.

Castor, J.; McCray, R., Weaver, R. 1975, *Ap. J. Letts.*, **200**, L107.

Chini, R.; Kreysa, E.; Mezger, P. G.; Gemünd, H.-P. 1984, *Astron. Astrophys.*, **137**, 117.

Dyck, H. M. and Lonsdale, C. J. 1979, *A.J.*, **84**, 1339.

Eiroa, C.; Elsässer, H.; Lahulla, J. F. 1979, *Astron. Astrophys.*, **74**, 89.

Felli, M.; Staude, H. J.; Redmann, T.; Massi, M.; Eiroa, C.; Hefele, H.; Neckel, T.; Panagia, N. 1984, *Astron. Astrophys.*, **135**, 261.

Gehrz, R. D.; Grasdalen, G. L.; Castelaz, M.; Gullixson, C.; Mozurkewich, D.; Hackwell, J. 1982, *Ap. J.*, **254**, 550.

Harvey P. M.; Gatley, I.; Thronson, Jr., H. A.; Werner, M. W. 1982, *Ap. J.*, **258**, 568.

Hippelein, H. and Münch, G. 1981, *Astron. Astrophys.*, **99**, 248.

Kandel, R. S. and Sibille, F. 1978, *Astron. Astrophys.*, **68**, 217.

Landolt, A. U. 1983, *A.J.*, **88**, 439.

Longmore, A. J.; Robson, E. I.; Jameson, R. F. 1986, *M.N.R.A.S.*, **221**, 589.

Lucas, R.; Le Squéren, A. M.; Kazès, I.; Encrenaz, P. J. 1978, *Astron. Astrophys.*, **66**, 165.

Minkowski, R. 1946, *P.A.S.P.*, **58**, 305.

Mozurkewich, D.; Schwartz, P. R.; Smith, H. A. 1986, *Ap. J.*, **311**, 371.

Panagia, N. and Felli, M. 1975, *Astron. Astrophys.*, **39**, 1.

Perkins, H. G.; King, D. J.; Scarrott, S. M. 1981, *M.N.R.A.S.*, **196**, 7P.

Persson, S. E.; MacGregor, P. J.; Campbell, B. 1988 preprint.

Pipher, J. L.; Sharpless, S.; Savedoff, M. P.; Kerridge, S. J.; Krassner, J.; Schurmann, S.; Soifer, B. T.; Merrill, K. M., *Astron. Astrophys.*, **51**, 225.

Sharpless, S. 1959, *Ap. J. Suppl.*, **4**, 257.

Sibille, F.; Bergeat, J.; Lunel, M.; Kandel, R. 1975, *Astron. Astrophys.*, **40**, 441.

Solf, J. and Carsenty, U. 1982, *Astron. Astrophys.*, **113**, 142.

Staude, H. J.; Lenzen, R.; Dyck, H. M.; Schmidt, G. D. 1982, *Ap. J.*, **255**, 95.

Stutzki, J.; Ungerechts, H.; Winnewisser, G. 1982, *Astron. Astrophys.*, **111**, 201.

Tokunaga, A. T.; Lebofsky, M. J.; Rieke, G. H. 1981, *Astron. Astrophys.*, **99**, 108.

Tokunaga, A. T. and Thompson, R. I. 1979, *Ap. J.*, **233**, 127.

Wright, A. E. and Barlow, M. J. 1975, *M.N.R.A.S.*, **170**, 41.

FIGURE CAPTIONS

Figure IV.1 Gunn r band (λ = 6700 Å, $\Delta\lambda$ = 1000 Å) CCD frame of the S106 HII region (courtesy of Dr. James Schombert). North is up and east is to the left. The white vertical line is an artifact that is due to an insensitive column in the detector. The black vertical streaks, emanating from two bright, foreground stars, are effects of chip saturation. The northern lobe of the optical HII region is, on the average, 40 times fainter than the southern lobe, because the northern lobe is tilted into the S106 molecular cloud while receding from us along the line of sight, while the southern lobe is tilted out of the cloud, and approaching. Note the presence of an envelope of low-level emission, which surrounds the entire bipolar nebula.

Figure IV.2a Gunn r (λ = 6700 Å, $\Delta\lambda$ = 1000 Å) surface brightness profile of the bipolar nebula along its symmetry axis at p.a. 150°, passing through the position of S106 IR. The location of S106 IR is indicated by the arrow.

Figure IV.2b V−i profile of the S106 bipolar nebula along the same axis as in Figure IV.2a. Note the notch in the value of V−i right at the position of S106 IR, indicating its blue color relative to its surroundings. This same phenomenon was found in LkHα101 (see Figure III.2b).

Figure IV.3 IRAS Survey Coadd Intensity maps of the S106 molecular cloud at 12 μm, 25 μm, 60 μm, and 100 μm. Contour level units are W m^{-2} sr^{-1}. Negative contours are indicated by dashed lines and are due to overcorrection by the background level subtraction software. Positive contour levels are at 3.0, 6.0, 9.0, 12.0, 15.0, 20.0, 28.3, 40.0, 56.6, 80.0, 113.1, 160.0, 226.3, 320.0, 452.5, 639.9, 905.0, 1279.8, 1810.0, 2559.6, 3619.9, 5119.2, 7239.6, 10238.2, 14478.8, 20476.0, 28957.1, and 40951.1. Peak contour levels in each of the 12 μm, 25 μm, 60 μm, and 100 μm bands are at 1810.0, 10238.2, 3619.9, and 905.0 W m^{-2} sr^{-1}, respectively.

Figure IV.4 Radial profiles of the mid- and far-infrared emission in S106, derived from the IRAS data presented in Figure IV.3. The contours of Figure IV.3 were fit by ellipses in logarithmic steps of the radial coordinate (arcminutes) in each of the four IRAS bands. Error bars indicated at a few data points are representative of the magnitude of the uncertainties at all points. Note that the maxima of the emission in all four bands coincide in position with the S106 bipolar nebula, which is, therefore, the major source of heating in the cloud. The bump in the emission intensity at r = 8′ is due to another source in the same cloud. The slope of the emission intensity is consistent with an r^{-3} falloff, indicated by the line at the top right of the figure. This radial dependence of the dust emission translates into an r^{-2} dust volume density distribution, assuming the dust emission to be optically thin (see text).

Figure IV.5 The spectral energy distribution of S106 in the range 2.3 μm $\leq \lambda \leq$ 100 μm. Integration under this curve yields a luminosity of 1.3×10^4 $L_\odot$ for a distance of 600 pc to S106. The curve can be decomposed into two components: a 390 AU radius 920 K blackbody and a 36000 AU radius 60 K component.

Figure IV.6a FCRAO map of the CO emission in S106, integrated over the velocity interval -10 km s^{-1} $\leq +$ 10 km s^{-1}. Contour level units are K km s^{-1}. The (0,0) coordinates correspond to $\alpha_{1950} = 20^h25^m33.8^s$, $\delta_{1950} = 37°12'50.15''$. All offsets are in minutes of arc from this position.

Figure IV.6b FCRAO map of the ^{13}CO emission in S106, integrated over the velocity interval $-$ 10 km s^{-1} $\leq +$ 10 km s^{-1}. Contour levels are in K km s^{-1}.

Figure IV.6c FCRAO map of the CO excitation temperature in S106. Contour level units are marked in degrees Kelvin. Note how the morphology of the decreasing contour levels follows the shape of the bipolar nebula. This is a clear indication of the disruption

of the cloud by the expanding HII region, which sweeps up the surrounding molecular gas.

Figure IV.6d FCRAO map of the molecular gas column density in S106. Contour levels are N_{CO} in units of 10^{18} cm^{-2}. Note that the peak in molecular gas column density is offset from the position of S106.

Figure IV.7a CO blue-wing emission from S106, mapped with the FCRAO 14 m telescope. Contour levels are marked in K km s^{-1}. Map-center coordinates are at $\alpha_{1950} = 20^h25^m33.8^s$, $\delta_{1950} = 37°12'50.15''$. All offsets are in minutes of arc from this position.

Figure IV.7b CO red-wing emission from S106, mapped with the FCRAO 14 m telescope. Contour levels are marked in K km s^{-1}. Note the lack of any organized, molecular outflow in this source.

Figure IV.8a OVRO interferometer map of the integrated ^{13}CO emission from S106. Contour levels are at 5%, 10%, 20%, 30%, 40%, 50%, 60%, 70%, 80%, 90%, and 100% of the peak value of 20.45 Jy/beam/km s^{-1}. The beam FWHM is 7.01″ × 5.84 ″ at position angle 0.3°.

Figure IV.8b OVRO interferometer map of the integrated CS emission from S106. Contour levels are at 5%, 10%, 20%, 30%, 40%, 50%, 60%, 70%, 80%, 90%, and 100% of the peak at 1.11 Jy/beam/km s^{-1}. The beam FWHM is 7.92″ × 4.58″ at position angle 8.7°.

Figure IV.8c Hat Creek interferometer map of the integrated HCN emission from S106. Contour levels are spaced at 0.3 K intervals and represent the average brightness temperature of channels with velocities in the range $-10.1 \leq V_{LSR} \leq +10.2$ km s^{-1}. The beam FWHM is 11″ × 15″ at position angle 99°.

Figure IV.8d OVRO interferometer map of the 110 GHz continuum emission from S106. Contour levels are at 10%, 20%, 30%, 40%, 50%, 60%, 70%, 80%, 90%, and 100% of the peak value of 0.386 Jy/beam.

Figure IV.9 OVRO ^{13}CO channel maps of S106. The cloud rest velocity is at -1.0 km s^{-1}. Note the lack of any molecular gas at $\alpha_{1950} = 20^h25^m33.8^s$, $\delta_{1950} = 37°12'50.15''$, the position of S106 IR.

Figure IV.10 OVRO CS channel maps of S106. Again, note the lack of significant emission in the equatorial gap region, centered on the position of S106 IR at $\alpha_{1950} = 20^h25^m33.8^s$, $\delta_{1950} = 37°12'50.15''$.

Figure IV.11 OVRO CS integrated emission superposed on the 1.3 cm VLA radiograph of S106. The tiny white speck in the center is S106 IR, which is a weak radio emitter compared with its lobes. Note the equatorial "gap" in the radio emission, also present at optical (see Figure IV.1) and infrared (Gehrz *et al.* 1982) wavelengths. The gap is not *totally* devoid of emission at any of these wavelengths; rather, the emission exists at very low levels compared with the bipolar nebula. This morphology can be explained easily as the result of a stellar wind with an azimuthally varying velocity law, as explained in the text.

Figure IV.1 **S106–Gunn r IMAGE**

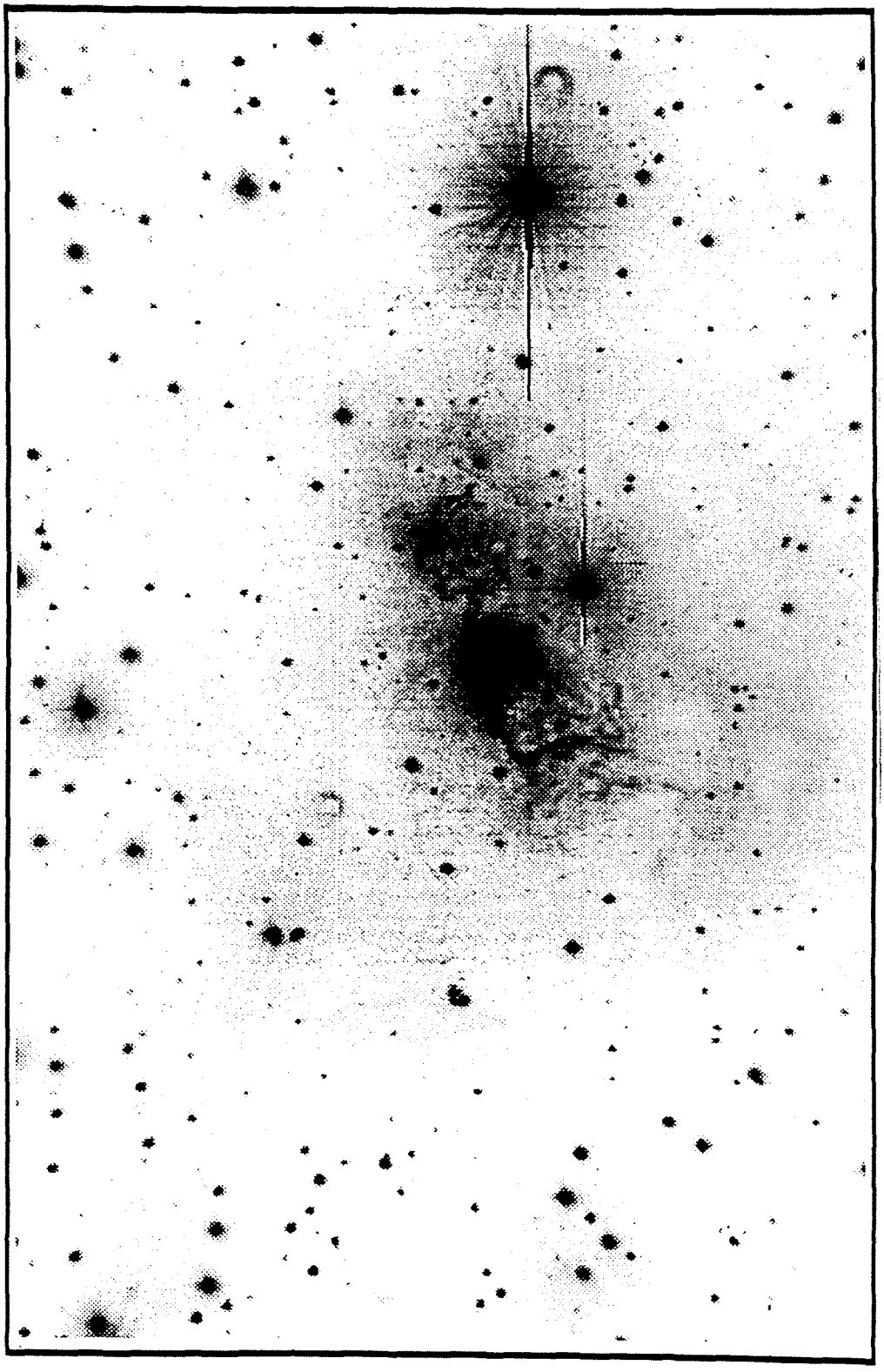

Figure IV.2

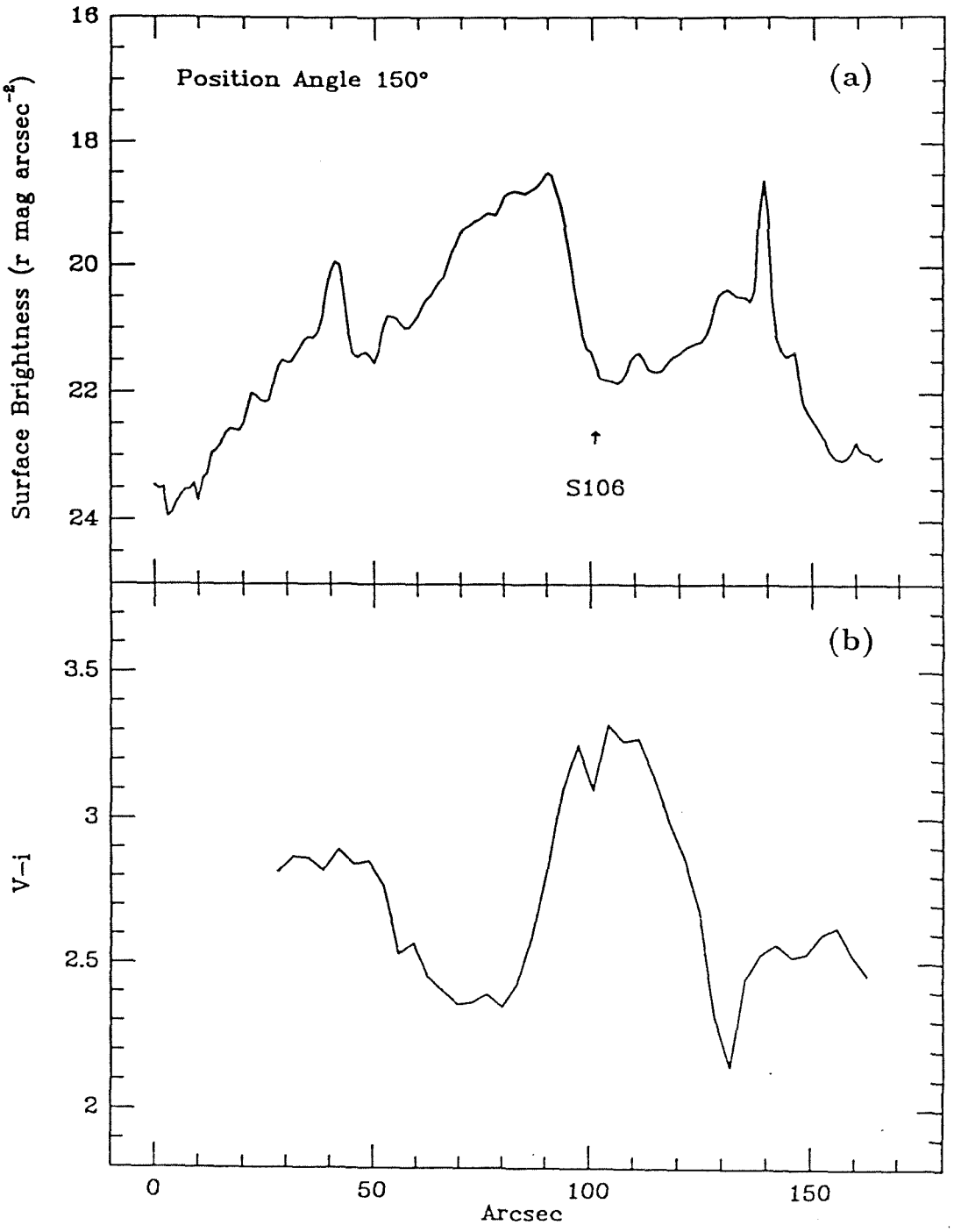
Position Angle 150°
(a)
S106
(b)
Surface Brightness (r mag arcsec^{-2})
V-i
Arcsec
16
18
20
22
24
3.5
3
2.5
2
0
50
100
150

12 μm IRAS MAP Figure IV.3 25 μm IRAS MAP

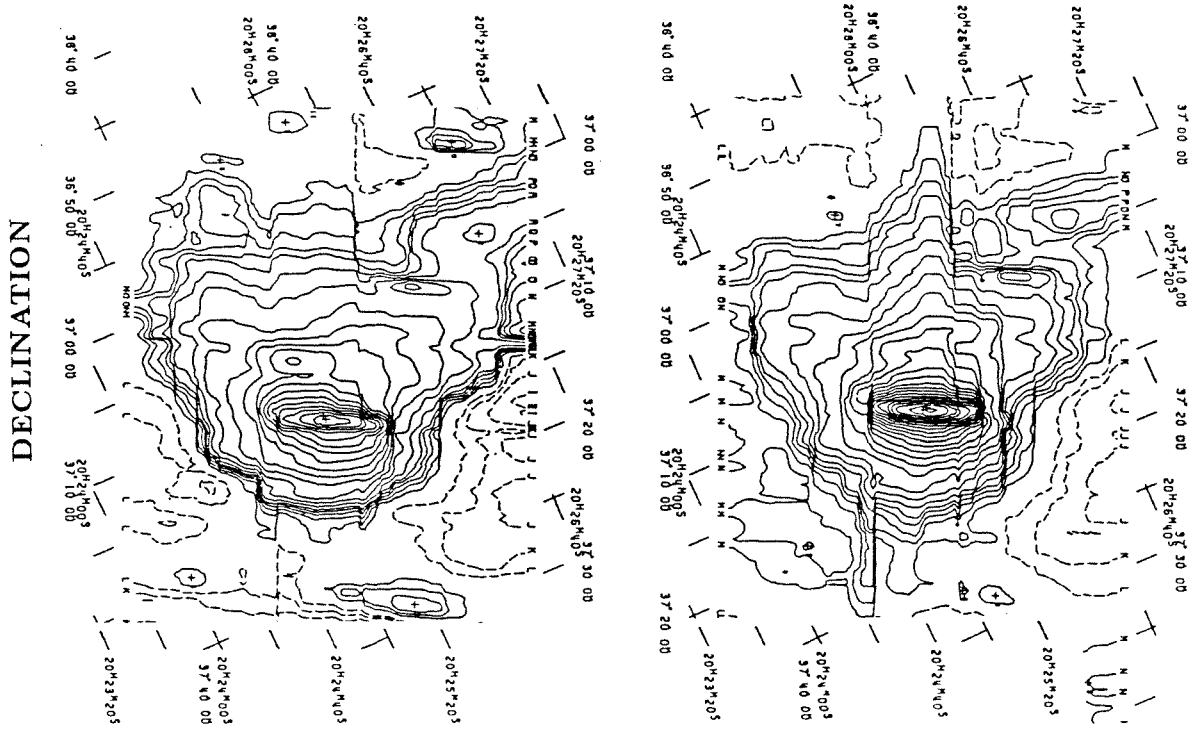

S106

60 μm IRAS MAP 100 μm IRAS MAP

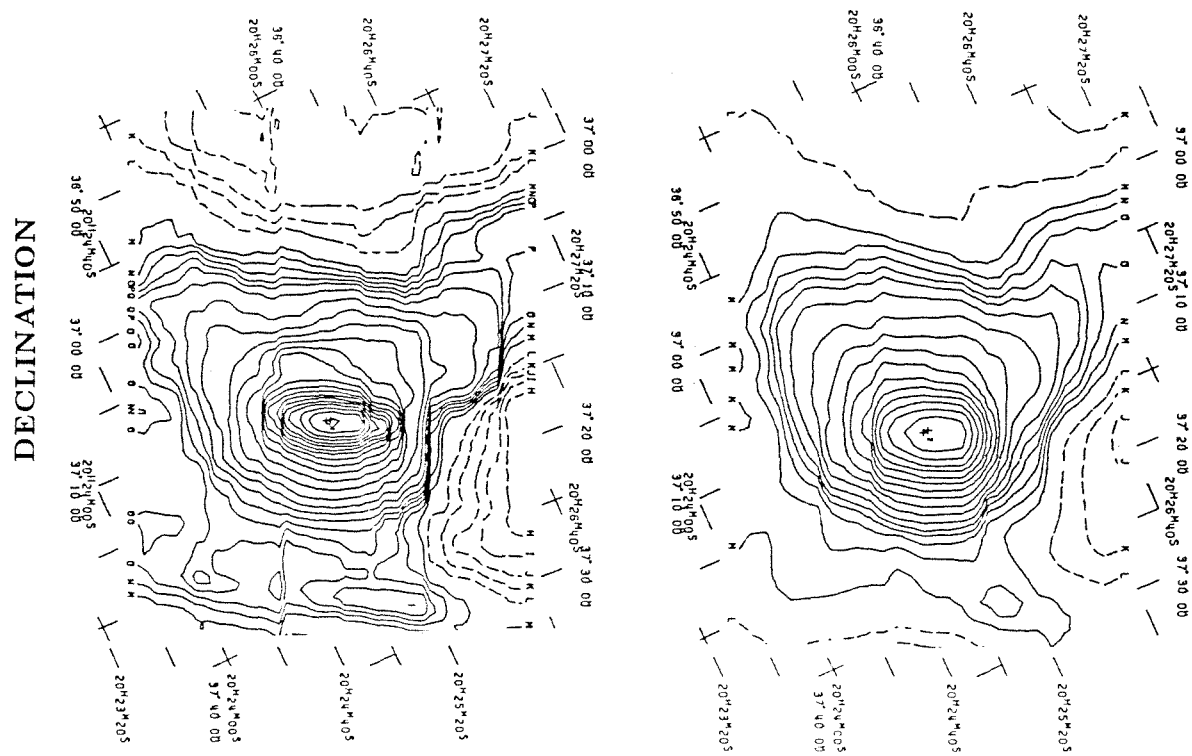

Figure IV.4 RADIAL PROFILE OF DUST EMISSION INTENSITY

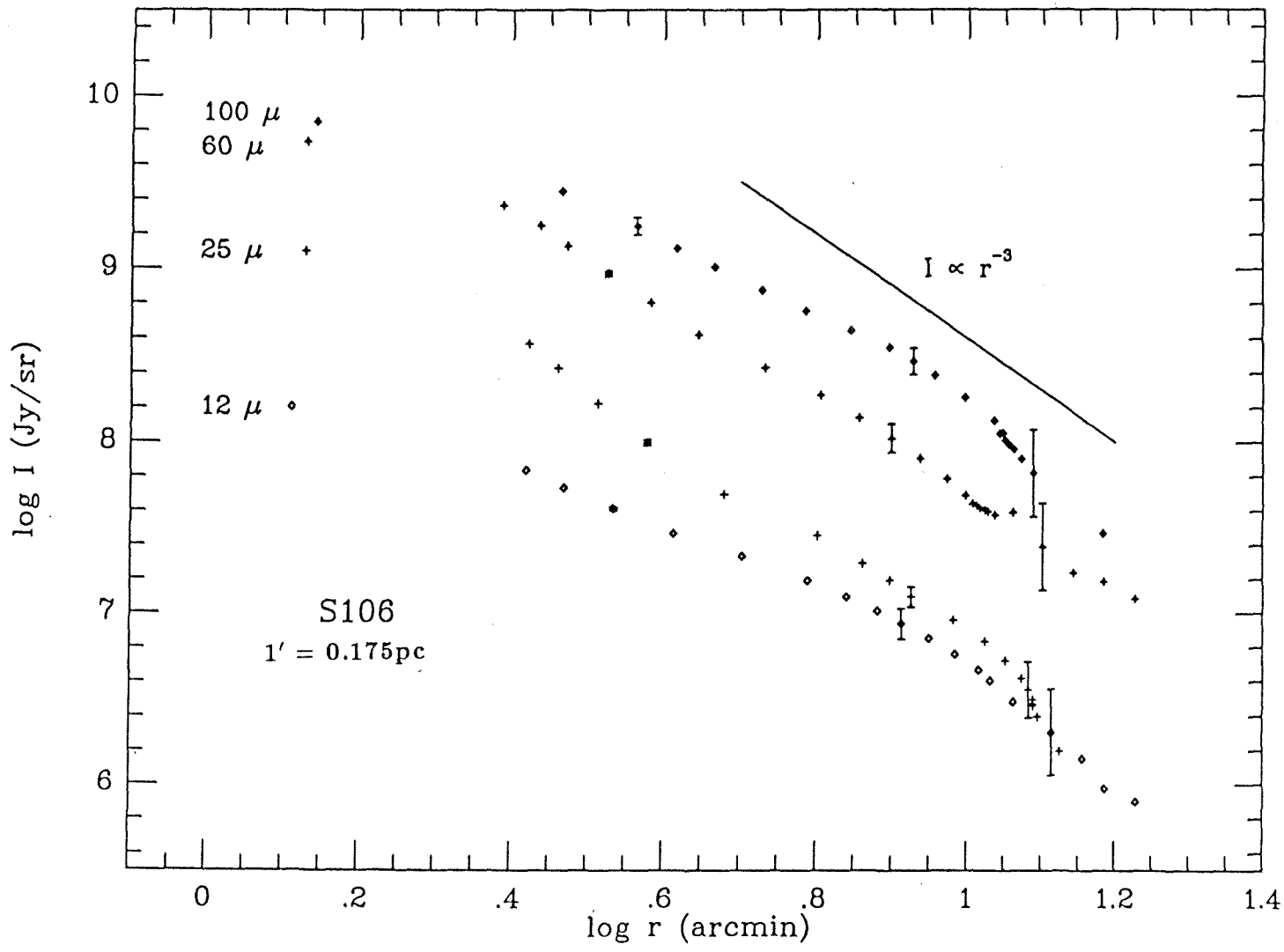

Figure IV.5 S106 CENTRAL POINT SOURCE SPECTRUM

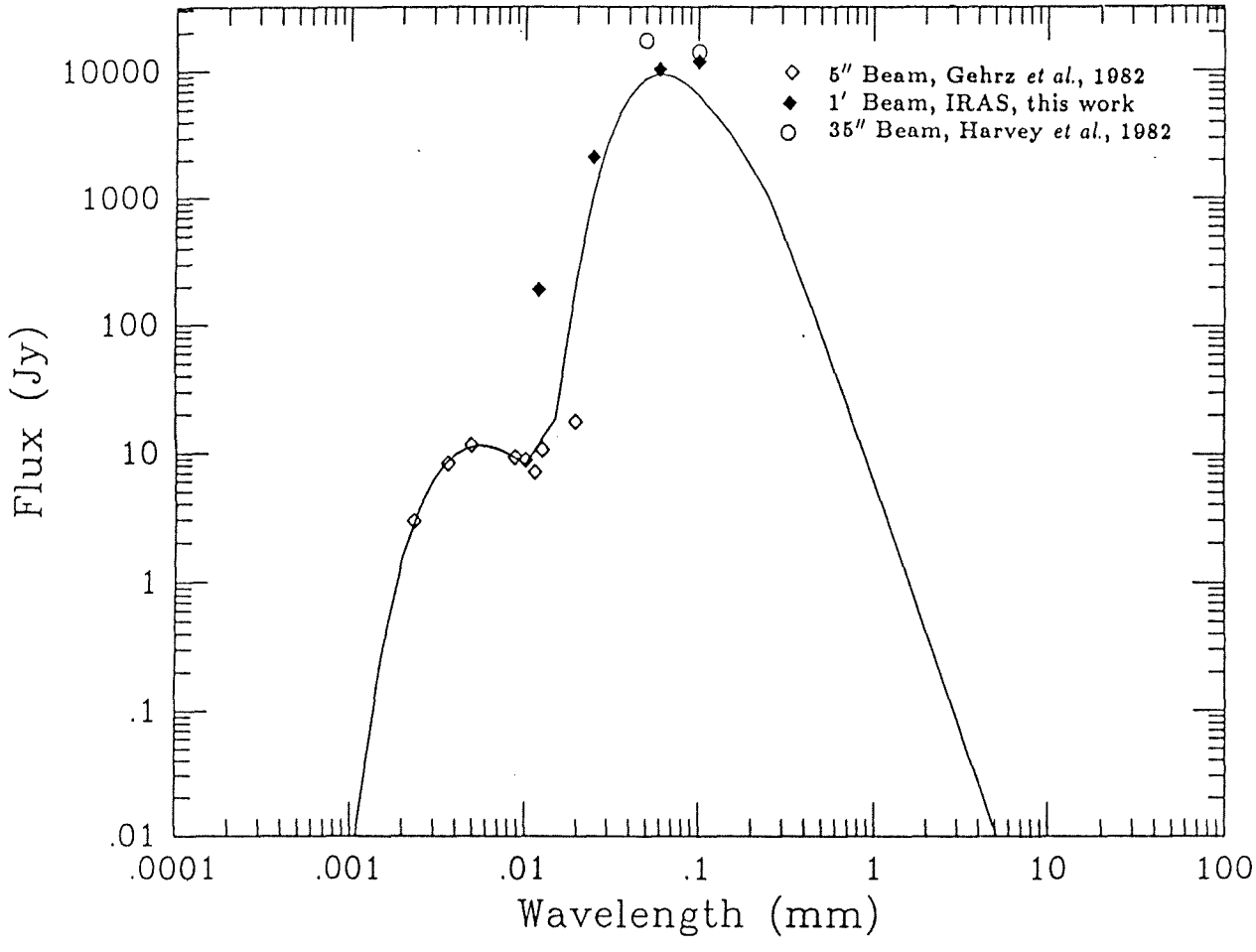

Figure IV.6 S106 FCRAO MAPS

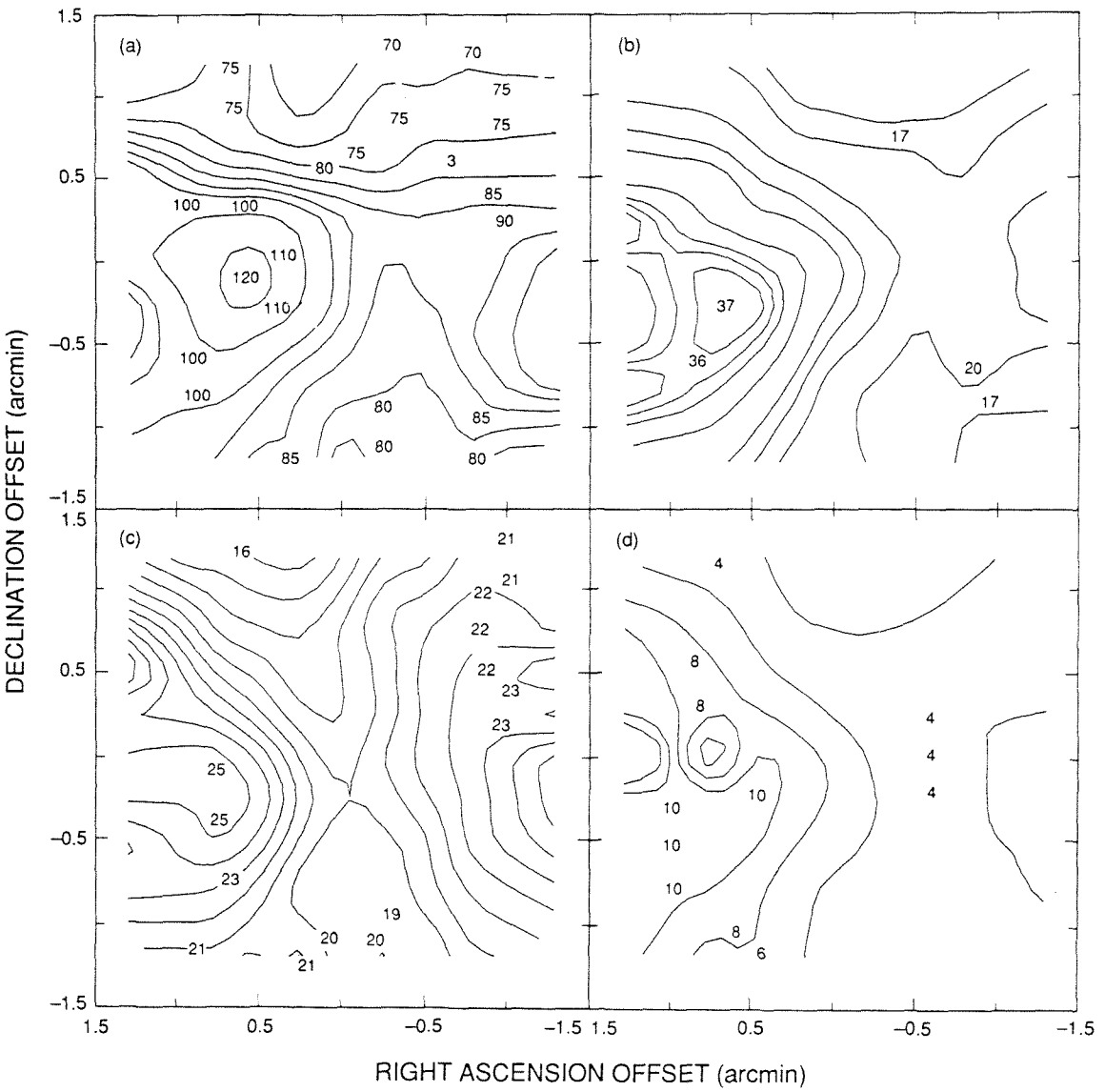

Figure IV.7 S106 LINE WING EMISSION

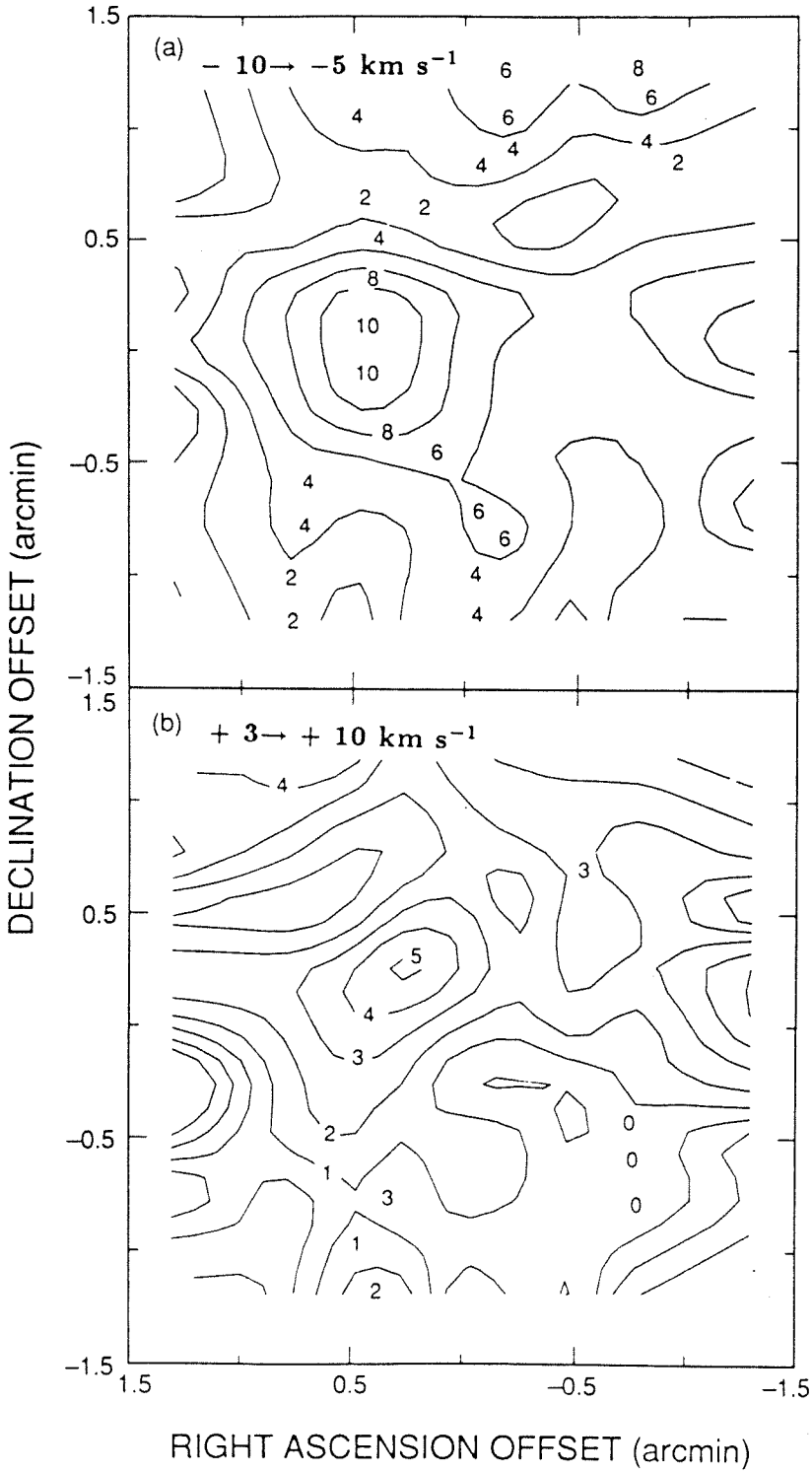

Figure IV.8 S106 INTEGRATED LINE AND CONTINUUM EMISSION

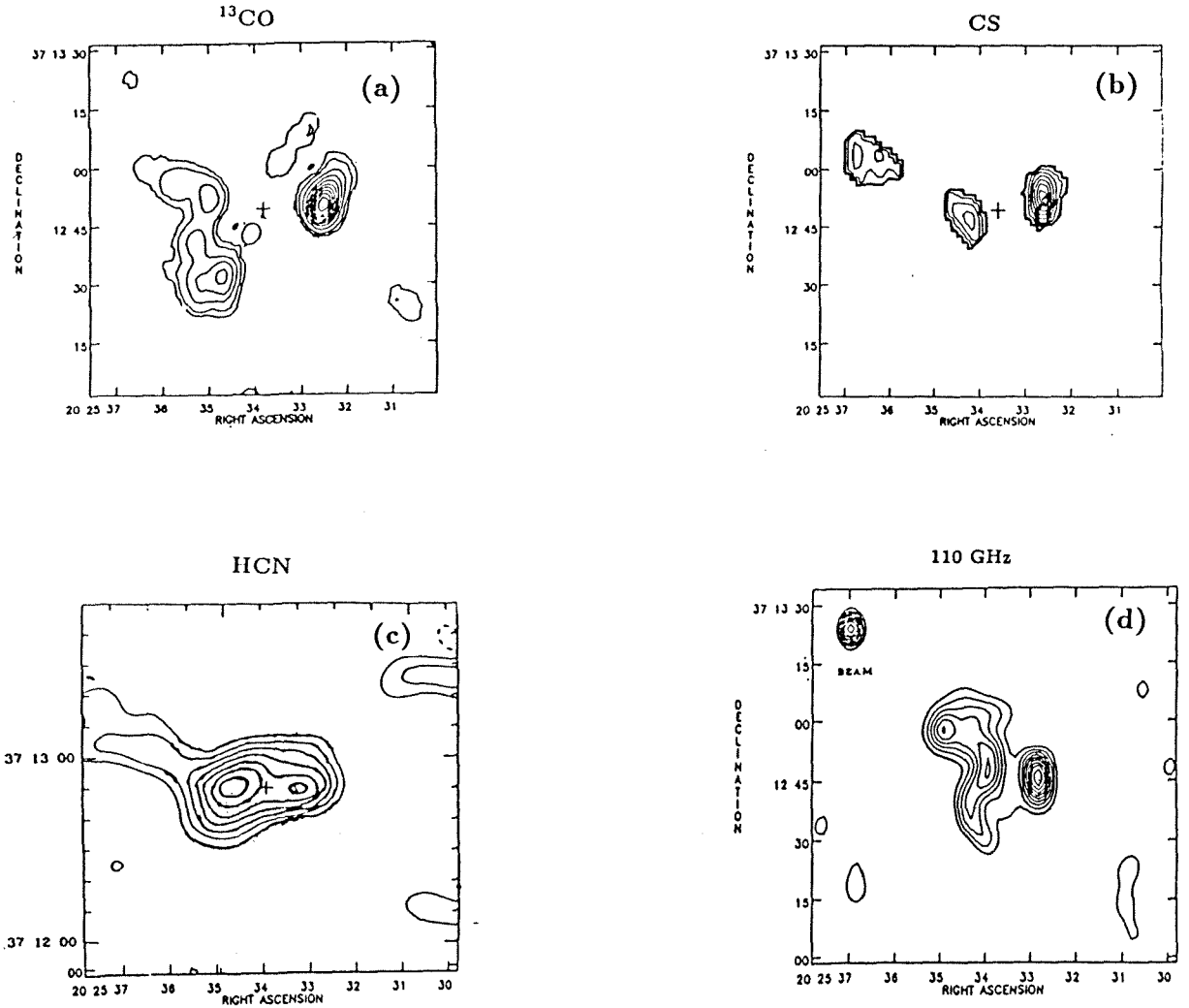

Figure IV.9 OVRO ^{13}CO MAPS OF S106

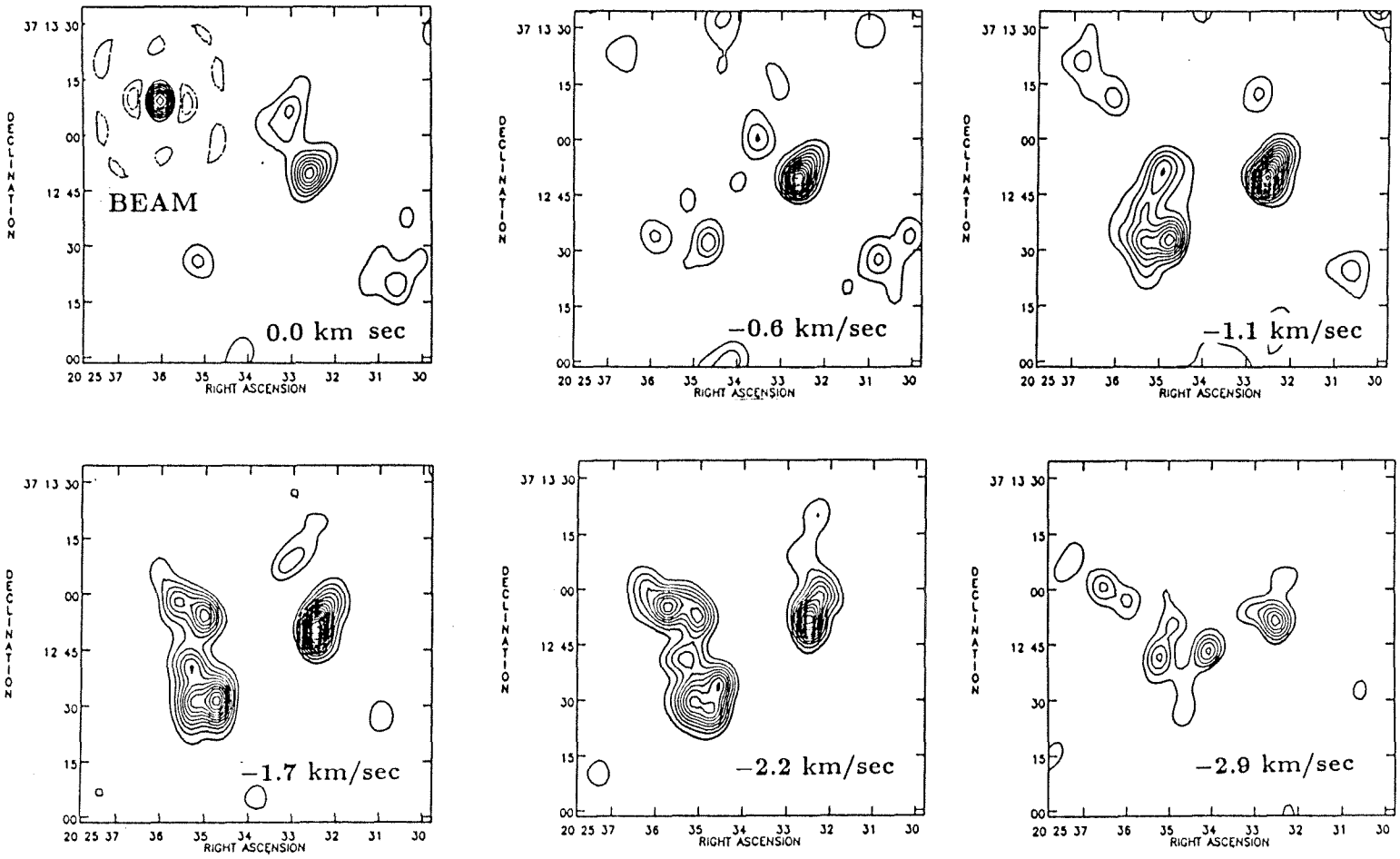

Figure IV.10 OVRO CS MAPS OF S106

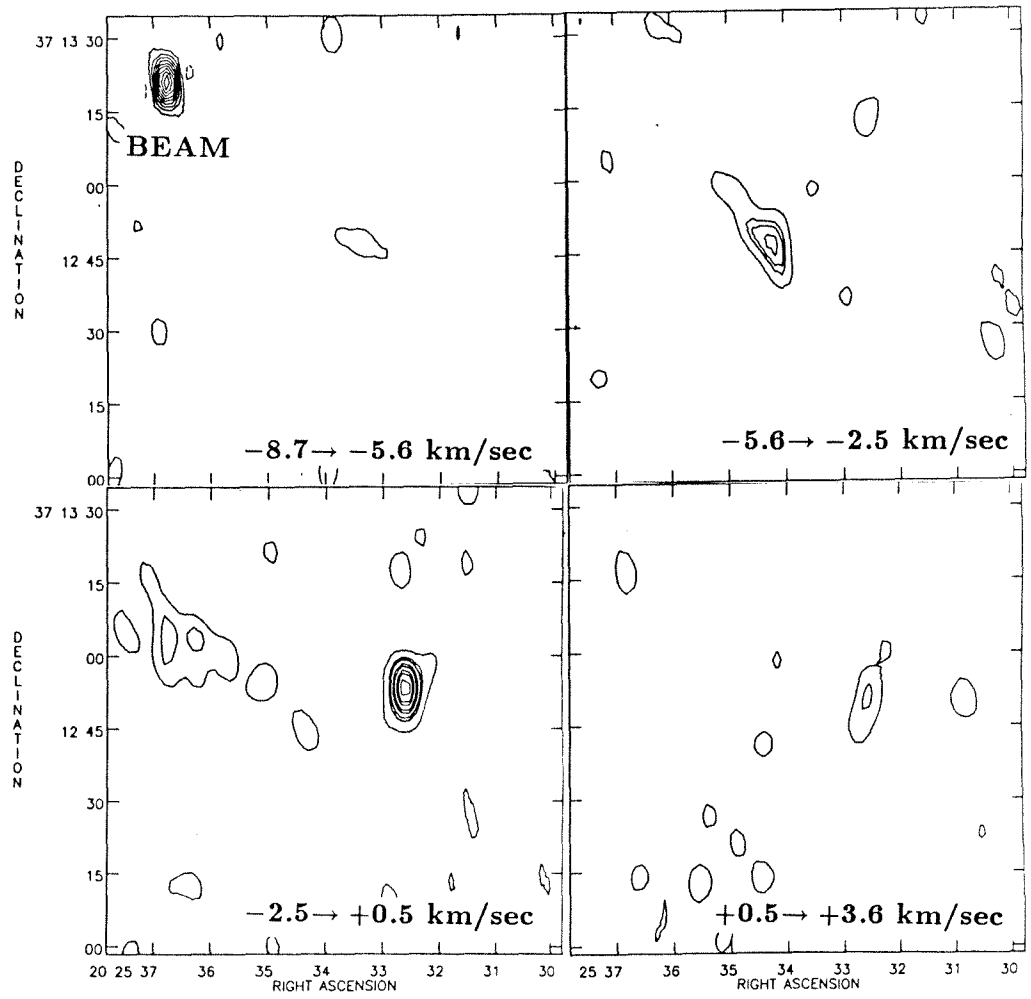

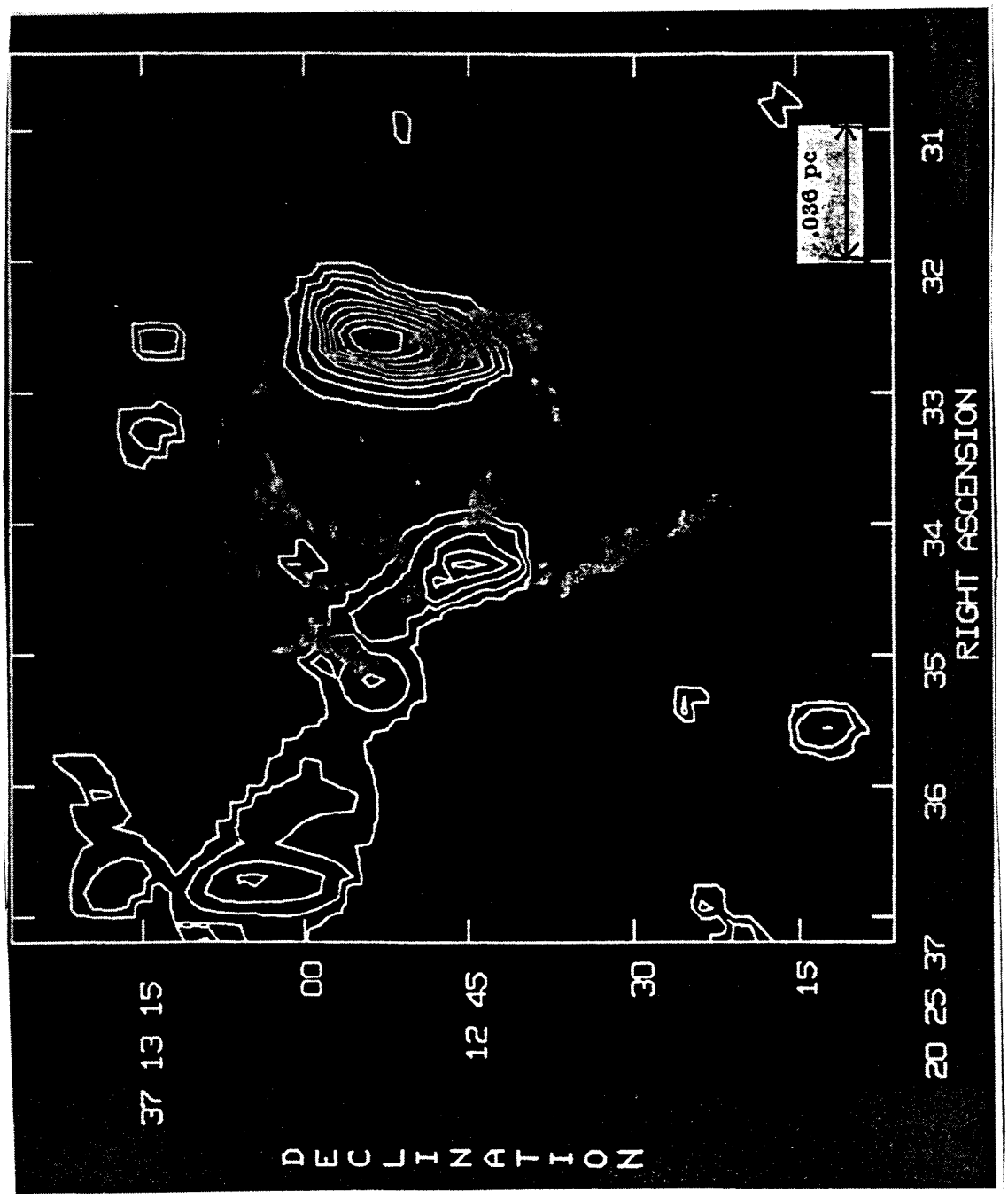
.038 pc
RIGHT ASCENSION
31
32
33
34
35
36
37
20 25
15
30
12 45
00
37 13 15
DECLINATION

Figure IV.11

V. Outflows from High-Mass, Pre-Main Sequence Stars

It is clear from the last three chapters that although not every high-mass, pre-main-sequence (PMS) star exhibits an ordered, large-scale (> 0.1 pc) *molecular* outflow, each *is* the source of a powerful, highly supersonic, ionized wind. This wind, in turn, dramatically alters the embedded source's surrounding molecular cloud environment.

V. A. Comparison of Wind Properties

The radio spectral index, α, is defined by its relation to the observed radio flux, S_ν, at a frequency, ν:

$$S_\nu \propto \nu^\alpha.$$

The predicted spectral index for an *unresolved*, ionized, isotropic, steady stellar wind, extending to infinity, is 0.6–0.7 (Wright and Barlow 1975; Panagia and Felli 1975). This result has been generalized to non-spherical, radial flows as well (Schmid-Burgk 1982).

Both S106 IR and LkHα101 are unresolved, while the core of S87 *is* resolved, at 0.5″ resolution. The observed spectral index of S106 IR is 0.73 between 5 and 23 GHz (Bally, Snell, and Predmore 1983). For LkHα101, the observed radio spectral index is 0.67 between 2.7 and 110 GHz. At 5 GHz, half the emission from the VLA core is produced closer to the star than 195 AU, and the outflowing envelope is optically thick within 75 AU of LkHα101 (Simon and Cassar 1984). The derived mass-loss rates for LkHα101 and S106 IR are 1.1×10^{-5} and 1.7×10^{-6} $M_\odot$ yr^{-1}, respectively (see §§ III.D.2 and IV.D.3).

The spectral index of the S87/IRS1 core is $+0.4 \pm 0.2$ between 1.4 and 5 GHz and -0.2 ± 0.2 between 5 and 15 GHz, typical for bremsstrahlung from an HII region. Note that one cannot distinguish a static from a dynamic HII region from the radio spectral index for a *resolved* source. In the case of S87, it is the Hα linewidth that provides convincing evidence for the presence of a supersonic, ionized wind (see § II.C.3 and Figure II.8). Assuming the observed 1 $M_\odot$ of ionized gas to be a result of mass loss, while adopting a

dynamical time scale of 5.4×10^4 years for the VLA lobe, leads to $\dot{M} = 1.8 \times 10^{-5}$ $M_\odot$ yr^{-1} for S87.

All three sources studied exhibit dense, ionized gas cores, which are best characterized as outflowing, circumstellar envelopes. The outer boundary of the VLA cores covers the range < 90 AU to 1500 AU. The deconvolved source size of the S87/IRS1 VLA core is 1500×1400 AU at 19° position angle at 5 GHz. For purposes of comparison, the optically thick surfaces of the S87/IRS1 core have radii of 150 AU at 15 GHz, 450 AU at 5 GHz, and 1200 AU at 1.4 GHz (using the VLA data of Table II.4). The upper limit on the size of S106 IR at 22 GHz is 90 AU (Felli *et al.* 1984). The upper limit on the size of the LkHα101 core at 5 GHz is 400 AU (Cohen, Bieging, and Schwartz 1982).

A determination of the *inner* radius of these winds is more problematical. Until recently, most authors had presumed that the *ionized* winds in question had their origin at the stellar surfaces, although, to date, no highly luminous, pre-main sequence source has been observed to exhibit linewidths comparable to the ≈ 1000 km s^{-1} required to escape the surface of a typical O or B star. Note that winds originating 10 stellar radii from the embedded sources would be consistent with the observed linewidths and would require 90% less power to accelerate than if they originated at the stellar photospheres.

In the case of S106 IR, it has been suggested that dense (10^{13} cm^{-3}), neutral material lies closer to the core source than the ionized wind that emits the radio flux (Persson, McGregor, and Campbell 1988). This conclusion rests on an analysis of the CaII triplet lines in which an electron temperature favorable to such an interpretation of the data is *assumed.* While it is inarguable that along the line of sight there is a CaII emitting region (*i.e.,* dense, neutral gas) within a 2″ aperture about the VLA core source, the true line of sight distance of this region from S106 IR is by no means clear. For instance, this

observed neutral gas could well be part of the dense, swept-up dust and gas shell, which marks the outer boundary of the outflowing, ionized, circumstellar envelope.

A self-consistent determination of the circumstellar winds' inner and outer radii could be made if one were to combine radio continuum maps at several frequencies with high signal-to-noise, velocity-resolved spectroscopy of the Brα and Brγ hydrogen lines. Expected radio fluxes at 1.3 and 6 cm for spherical outflow models have been calculated to take into account the effect of the observed *finite* outer radius of the outflowing circumstellar envelopes (Simon *et al.* 1983). Figure 1a of Simon *et al.* shows that to be detected at 5 GHz, an ionized wind must have a value of at least 2000 for the ratio of its outer to inner radii. The radio continuum flux as a function of the ratio r_o/r_i (outer to inner core radius) can be calculated for any given mass-loss rate and wind-velocity law. The outer radius (and therefore, the inner radius) may immediately be determined for a resolved source. If the source is unresolved, one can at least set firm upper limits on the outer and inner core radii.

Analysis of the Brackett line shapes and relative fluxes can provide the necessary complementary information for a self-consistent wind model. For a chosen value of the wind inner radius, the ratio of integrated Brα to Brγ flux varies tremendously with mass loss rate, allowing a good estimate of this quantity, independent of that derived from the radio-continuum, flux measurements. Analysis of the Brα and Brγ line shapes allows determination of the velocity law in the wind-acceleration region as well as the optical depths in the lines. Given the wind-velocity law and mass-loss rate, the maximum optical depth in the Brackett lines allows the determination of r_i, the wind's inner radius (Equation 10 of Simon *et al.* 1983):

$$\tau_{Br\alpha}(r_i) = 3.3 \times 10^4 \left(\frac{3 \times 10^{11}\, cm}{r_i}\right)^3 \dot{M}^2 v^{-3} b_4,$$

where $\dot{M}$ is the mass loss rate in 10^{-6} $M_\odot$ yr^{-1}, v is the wind velocity in units of 100 km s^{-1}, and b_4 is the LTE population departure coefficient of the n=4 level of hydrogen. Such a self-consistent model of the radio and near-infrared data on S106 results in r_i = 12 $R_\odot$ and r_o = 640 $R_\odot$ (Felli *et al.* 1984). Since the observations cannot determine whether S106 IR is a B0 III or O 9.5 V star ($r_* = 13R_\odot$ vs. $r_* = 8R_\odot$), it is still an open question whether the wind is accelerated right at the stellar surface, or a few stellar radii out. In the near future, ionized core inner radii for sources like S106 IR may be determined using the technique outlined above.

The next obvious question to ask is what drives these winds. Radiation pressure is capable of driving the ionized outflows only if

$$\dot{M} \leq \frac{L_*}{cv},$$

where $\dot{M}$ is the mass-loss rate, L_* is the stellar luminosity, c is the speed of light, and v is the wind velocity. For S87, radiation pressure could drive a mass loss rate of 4 × 10^{-6} $M_\odot$ yr^{-1}, for a wind speed of 160 km s^{-1} and a stellar luminosity of 35000 $L_\odot$, a factor of 5 smaller than the derived mass-loss rate value. For LkHα101, a mass-loss rate of 6 × 10^{-7} $M_\odot$ yr^{-1} could be radiation pressure driven, assuming v_w = 350 km s^{-1} and $L_\odot$ =1.1 × 10^4 $L_\odot$. The derived mass-loss rate for LkHα101 is a factor of 17 higher than this value. Finally, in S106, for a 200 km s^{-1} wind velocity, radiation pressure could drive a mass loss rate of $\dot{M}$ = 1.3 × 10^{-6} $M_\odot$ yr^{-1}, consistent with the observationally derived rate of 1.7 × 10^{-6} $M_\odot$. Radiation pressure is, therefore, inadequate to drive the observed winds of S87/IRS1 and LkHα101.

The mechanical luminosities ($\dot{M}v^2$) of the ionized winds are 111, 39, and 6.8 $L_\odot$, respectively, for LkHα101, S87/IRS1, and S106 IR, all between 0.1–1% of the stellar luminosities.

The ionized wind's driving mechanism in massive, pre-main-sequence (PMS) stars is an exciting topic for future investigation. There are two major differences between the main sequence and PMS winds of O and B stars, these being higher observed velocities and lower mass-loss rates in main sequence vs. PMS stars. Referring to Figure V.1, we see that for objects that are still evolving towards the ZAMS (*i.e.*, still contracting), radiation pressure alone is incapable of driving the observed mass loss.

V. B. Circumstellar Disks

In all three sources, the distribution of circumstellar neutral gas and dust *must* be anisotropic in order to allow sufficient numbers of ionizing photons to escape to photoionize the surrounding, extended, low-density VLA lobes. The question is: Does an "anisotropic" distribution necessarily translate into "disk structure" ?

Because of its suggestive bipolar morphology, of the three sources examined, the best candidate for the presence of a disk is S106. We have noted in § IV.D.2 that the new OVRO interferometer results show no evidence of a molecular gas disk with a radial extent comparable to that of the bipolar nebula. Thus, if a disk exists in S106, it must be on a scale < 90 AU.

It must be stressed that a disk structure is *not* necessary to explain the morphology of the bipolar HII region in this source. Asymmetric mass loss that is due to a latitudinally varying velocity field can easily account for the observed morphology of the S106 HII region. This explanation follows from noting that the maximum number of ionizing photons that can be absorbed in the wind is:

$$N_{L_{max}} \propto n_e^2 \propto \left(\frac{\dot{M}}{v}\right)^2.$$

A critical value of $\dot{M}/v$ is defined by the minimum number of stellar, ionizing photons per second required to ionize the entire envelope. If $\dot{M}/v$ is greater than this critical value,

then the outflowing envelope becomes neutral at some radius, r_0. If $\dot{M}/v$ is less than the critical value, the entire outflowing envelope becomes fully ionized (Felli and Panagia 1981). Assuming that $\dot{M}/v$ reaches its "critical" value in the equatorial plane of S106 and that the wind velocity towards the polar regions is twice its equatorial value, this slight asymmetry in the velocity field will allow 75% of the ionizing radiation to escape towards the poles, and no ionizing radiation to escape towards the equator.

The first suggestion of the presence of a face-on disk in LkHα101 was made over ten years ago, because of its strong similarity to the source MWC 349 (Thompson *et al.* 1977). The argument for a face-on disk in MWC 349 rests on the interpretation of its optical continuum emission. Thompson *et al.* claim that when the observed optical continuum is corrected for extinction, then $F_\nu \propto \nu^{1/3}$, rather than to ν^2. It is not clear to this author that the derived extinction values are known to sufficient accuracy to be able to distinguish between a blackbody vs. a $\nu^{1/3}$ frequency dependence of the optical continuum. Since the frequency dependence of the optical continuum is predicted to vary as $\nu^{1/3}$ for an accretion disk (Lynden-Bell and Pringle 1974), Thompson *et al.* argue that such a disk must be present in MWC 349. Even if such an accretion disk does exist in MWC 349, its presence remains to be proven in the case of LkHα101.

There is, however, a highly asymmetric distribution of gas and dust in the immediate environs of LkHα101. This deduction follows from the simultaneous presence of its dense, optically thick envelope with an accompanying, greatly extended HII region (see § III.A). An independent line of reasoning, also leading to the conclusion of an asymmetric gas and dust distribution in LkHα101, is based upon the shape of the Brγ line, obtained with 120 km s^{-1} velocity resolution in a 7″ aperture (Thompson *et al.* 1976). At this resolution, the Brγ line toward LkHα101 exhibits an absorption component at -400 km s^{-1} relative to the line rest velocity, with line emission observed at even bluer velocities. This Brγ

profile can be explained by the presence of a dust cloud slightly offset from the line of sight to the star. The dust cloud is responsible for the absorption component at −400 km s^{-1}, while its offset from the star allows emission from the gas at higher, blue-shifted velocities to escape.

There is currently no evidence of any small-scale ($\leq$ 1500 AU) disk structure in S87/IRS1. On the contrary, the VLA core exhibits a fairly isotropic structure (see Figure II.3). However, the density distribution at this and smaller scales *must* be inhomogeneous to allow the escape of ionizing photons into the much larger, low-density lobe. Some evidence of such inhomogeneity is apparent in the irregularity of the contour level shapes of Figure III.3.

V. C. Evolutionary Status

In Figure V.1, all three sources have been placed on an H-R diagram along with the evolutionary tracks predicted for high-mass, pre-main sequence stars (Ezer and Cameron 1967). In this context, one should be aware that the calculations that resulted in the evolutionary tracks of Figure V. 1 ignore the effects of mass loss, which can change the star's final mass by 5–10% at most, assuming the currently observed mass-loss rates are constant over the star's pre-main sequence lifetime. All three sources are very close to being on the ZAMS and are $\approx 10^5$ years old. S87/IRS1 is the youngest, and S106 IR the oldest of the three sources studied.

This ranking by age is consistent with the radio-continuum morphologies of the sources in the following sense: In S87, the core dominates the radio flux, while in S106 nearly all the radio emission originates from the lobes. LkHα101 is intermediate between these two extremes. The molecular gas distribution also shows an evolutionary effect, in that it is the youngest source that exhibits the outflow. Swept-up molecular gas is

seen in the surroundings of S106 and S87, indicating past disruption of the original cloud structure by the embedded object's stellar wind.

Note that radiation pressure can account for the observed mass-loss rate only in the oldest source, S106. In the younger sources, radiation pressure is inadequate to drive the observed ionized winds. It is not yet known exactly when the onset of mass loss occurs during the pre-main sequence evolution of a massive star. However, it is clear from observations discussed in this work, that powerful, ionized stellar winds are coeval with the contraction phase of high mass, pre-main sequence, stellar evolution.

V. D. Large-scale Structure

The one clear instance of a *molecular* outflow in this study is that of S87/IRS 1. The momentum supply rate available in the ionized gas is 2.96×10^{-3} $M_\odot$ km s^{-1} yr^{-1}. This value is to be compared with the momentum supply rate needed to accelerate the high velocity molecular gas, $M_{hvg} v_{hvg}/\tau = 3.0 \times 10^{-3}$ $M_\odot$ km s^{-1} yr^{-1}, for $M_{hvg} = 42$ $M_\odot$, $v_{hvg} = 3$ km s^{-1}, and $\tau = 5.4 \times 10^4$ years. The ionized stellar wind is, in this case, powerful enough to drive the molecular outflow as well.

Why then, is there no molecular outflow in S106 or LkHα101 ? The answer is apparent upon comparison of the OVRO integrated ^{13}CO maps of all three sources (Figures II.12, III.17, and IV.9). Only S87, the outflow source, shows siginificant molecular emission spatially coincident with the embedded, pre-main sequence star. In the two sources without molecular outflows, the high-resolution, molecular-line maps reveal a broken up molecular shell around LkHα101 and swept-up molecular gas fragments bordering the ionized lobes of S106. No molecular gas is detected at the positions of S106 IR or LkHα101 at high resolution, indicating that molecular gas in these regions has already been cleared away.

The necessary conditions for a molecular outflow are seen to be: the presence of a powerful stellar wind to provide momentum to the flow, and a sufficient amount of

molecular gas in the immediate vicinity of the embedded source. The channeling of the molecular flow into a bipolar configuration is a result of the density structure of the ambient cloud, which is determined by the cloud's internal magnetic field.

Even as a massive star is contracting, it is destroying its surroundings through the processes of photoionization, photodissociation, and the stellar wind.

The Strömgren radius of the HII region surrounding a high mass PMS star is a good indicator of the magnitude of the effect of photoionization in the parent cloud core. The Strömgren radius is given by (Osterbrock 1974):

$$r_s = \left[\frac{3}{4\pi N_H^2 \alpha_\beta} \int_{\nu_0}^{\infty} \frac{L_\nu}{h\nu} d\nu\right]^{1/3},$$

where N_H is the volume number density of hydrogen atoms; α_β is the recombination coefficient of hydrogen to all levels except the ground state in $cm^3\ s^{-1}$; L_ν is the stellar luminosity at frequency ν; h is Planck's constant; and ν_0 is the frequency at which hydrogen is ionized. For $N_H = 100\ cm^{-3}$ and $T_e = 7500$ K, the calculated Strömgren radii for S87, LkHα101, and S106 are 1.0, 0.56, and 1.35 pc, respectively. The *observed* radial extents of the HII regions are 0.25 pc in S87, 0.13 pc in LkHα101, and 0.073 pc in S106, as determined from VLA observations.

The radius of a theoretical "dissociation" region, beyond which all the available hydrogen gas would be molecular, is much more difficult to calculate than the Strömgren radius. This is due to the difficulty of assessing both the formation and destruction rates of H_2. Since H_2 is thought to form on grain surfaces, its formation rate is not a simple function of the HI density and is not well known. The destruction of H_2 through photodissociation is also not a straightforward function of the number of available stellar photons with energies above the 4.5 eV dissociation energy of H_2. This is because not all the H_2 is in its ground vibrational/rotational state, and the population levels need to be

known to calculate the photodissociation rate. To calculate the destruction rate of H_2, a self-consistent calculation of the H_2 level populations *and* the radiative transfer through the cloud is required. Furthermore, at densities above 10^5 cm^{-3}, which may be reached in dense molecular cloud cores, the effects of vibrationally inelastic collisions also need to be considered (Black and van Dishoeck 1987).

How much do the outflows contribute to dissipation of their parent molecular clouds? To date, only two unbiased surveys for molecular outflows in molecular clouds have been completed (Margulis and Lada 1986; Heyer *et al.* 1987). Margulis and Lada find a total momentum of about 160 $M_\odot$ km s^{-1} for all of the outflows in the Mon OB1 cloud, combined. Assuming that momentum conservation dominates the dynamics of these outflows, this means that 160 $M_\odot$ of gas can be accelerated to reach pressure equilibrium with this cloud's internal velocity field ($v_{turb} \approx 1$ km s^{-1}). In order to disrupt the entire 3.0×10^4 $M_\odot$ cloud, the available momentum from outflows would have to be increased by a factor of 200. Heyer *et al.* tentatively conclude that the outflows in the Taurus molecular cloud, including the three new ones they found from 30 candidate IRAS sources, cannot account for the total turbulent energy present in the TMC.

In the particular case of the outflows examined in this study, there are no reliable mass estimates available for the entire parent GMC masses, since only the central $2' \times 2'$ of the clouds' $20' \times 30'$ extents were mapped in CO and ^{13}CO. However, the cloud-core masses have been determined. They are: 700 $M_\odot$ within the central 1.2 pc^2 for S87, 112 $M_\odot$ within the central 0.46 pc^2 for LkHα101, and 135 $M_\odot$ within the central 0.34 pc^2 for S106. The internal turbulent velocities are ≈ 1 km s^{-1} in all three sources. The ionized wind momenta are 160, 35, and 30 $M_\odot$ km s^{-1}, for S87, LkHα101, and S106, respectively. Thus, the ionized outflows are definitely not capable of totally disrupting the cloud cores in which they are embedded.

Consequently, the ionized outflows cannot be responsible for the supersonic molecular linewidths observed throughout each molecular cloud. A more likely explanation for the observed linewidths is supersonic turbulence, fed by the gravitational potential energy of a cloud as it tries to collapse (Scalo and Pumphrey 1982). All the massive PMS stars considered in this study are centrally located in molecular clouds. From the embedded PMS star, the greatest radial extent of the IRAS emission is 4.6 pc in the S87 cloud, 4.3 pc in the LkHα101 cloud, and 3.6 pc in the S106 cloud. Assuming $N_{H_2} = 100$ cm^{-3} and $\mu = 1.36$, the free-fall time $(4\pi\rho G)^{-1/2}$ of each cloud is 1.6×10^6 yr. If the entire cloud undergoes free fall, then the average gas velocity, r/t_{ff}, in each cloud would be 2–3 km s^{-1}. These velocities are of the same order as the observed supersonic linewidths. It has been shown recently that the dissipation time scale of turbulent motions in a cloud can be ten times longer than the free fall time, if oblique cloud fragment collisions are the dominant dissipative process (Scalo and Pumphrey 1982).

So far, the IRAS emission from only one outflow source, L1551/IRS5, has been studied in any detail (Edwards *et al.* 1986). L1551/IRS5 is a low-luminosity outflow source and lacks the extended 12μm and 25μm emission found in each of the high-luminosity sources studied here. The 60 μm surface brightness distribution differs between the clouds harboring low- and high-luminosity outflow sources. Whereas the 60 μm surface brightness is nearly constant throughout the L1551 cloud, falling off less steeply than r^{-1}, in the high luminosity sources, it falls off as r^{-3}.

The IRAS color temperatures derived from the 100 μm/60 μm, 60 μm/25 μm, and 25 μM/12 μm fluxes are presented in Table V.1 for the three high luminosity sources, S87, LkHα101, and S106. In all cases, the derived color temperatures increase with decreasing wavelength, indicating that dust grains exist at widely varying temperatures throughout each cloud. The color temperatures determined from the 100 μm/60 μm flux ratios are

higher in the central "point source" than in the surrounding extended region; this is not always the case for the color temperatures derived from the other two sets of flux ratios. Clearly, further study of the dust properties and emission mechanisms at IRAS wavelengths is necessary to explain these observations.

V. E. Prospects for Future Work

For specifying avenues of worthwhile new research, it is as important to define what is not known, as to have a good overview of what *is* known. Therefore, an outline of areas of ignorance follows.

The most immediate problem in the study of outflows from high-mass PMS stars is explaining the wind driving mechanism. Results presented in this work show that radiation pressure is inadequate to drive the ionized winds in S87 and LkHα101, and only marginally adequate to drive the ionized wind in S106. Possible mass-loss mechanisms for consideration are Alfvén wave driven winds, accretion driven winds, rotationally driven winds, and winds driven by photospheric turbulent energy. Each of these mechanisms has its limitations (Hartmann 1986).

There is strong evidence for a latitudinal variation of $\dot{M}/v$ in S106 (see § IV.D.2). Such clear evidence for anistropic mass loss, within tens of AU from the source, does not exist for either LkHα101 or S87/IRS1, although it cannot be ruled out. A latitudinal dependence of the wind speed has been inferred in other PMS stars, however (Edwards *et al.* 1987). It is possible that most, if not all, PMS winds are intrinsically anisotropic. If so, the wind geometry must be incorporated into any viable model of the wind driving mechanism. Two other high-mass PMS wind properties found in this study must be understood: the lower terminal velocities and the higher mass-loss rates of these winds compared with their main sequence counterparts. An observational test to determine the

inner radius of the ionized PMS winds has been suggested in § V. A, to help clarify the origin of the relatively low terminal velocities observed.

The role of accretion disks in high mass star formation is still unknown. Until this study, the best example of such a disk was S106. It can now be said unequivocally that no molecular disks of sizes $\approx 10^{16}$ cm are known to exist. However, no unbiased searches for high mass protostars (without well-developed HII regions) have been made. Massive protostars, rather than pre-main sequence stars, would be better candidates to search for the existence of disks in the future. Presumably, these protostars would not yet have destroyed their parent molecular cloud environments, making the detection of accretion disks more likely.

Calculations of the evolutionary tracks of massive, pre-main sequence stars can be improved upon. In particular, in light of the new data, the effects of rotation and mass loss must be taken into account. Observations made in the near future should be able to provide the necessary initial conditions required for proper calculations. Careful interpretation of infrared observations in the future should shed more light on dust properties, which are crucial in controlling the time scale of evolution of a collapsing mass of gas into a star.

The IRAS color temperature distributions found in the clouds of this study need to be explained. Understanding of the IRAS data will involve detailed modelling of grain size distributions, optical properties, and self-consistent calculations of the temperature structure and radiative transfer in each cloud.

The origin of the intrinsic supersonic linewidths of molecular lines found in cold clouds is still not agreed upon. It is clear, after this study, and those of other authors (Margulis and Lada 1986; Heyer *et al.* 1987), that outflows from pre-main sequence stars do not have sufficient momentum to provide clouds with the observed amount of turbulence.

Other promising energy sources for the observed, supersonic turbulence are fragmentation during cloud collapse, followed by oblique cloud collisions (Scalo and Pumphrey 1982), or dissipation of Alfvén waves, excited by cloud collisions (Falgarone and Pérault 1987). Work on measuring magnetic field strengths in molecular clouds is currently in progress, as are studies of molecular cloud structure over several orders of magnitude in spatial scale.

TABLE V.1

IRAS Color Temperatures in Outflow Sources

T_c derived from this flux ratio	S87		LkHα101		S106	
	"Point" Source	Extended Source	"Point" Source	Extended Source	"Point" Source	Extended Source
	T_c (K)		T_c (K)		T_c (K)	
$f_\nu(100\,\mu m)/f_\nu(60\,\mu m)$	49	42	52	49	61	39
$f_\nu(60\,\mu m)/f_\nu(25\,\mu m)$	72	83	68	72	81	80
$f_\nu(25\,\mu m)/f_\nu(12\,\mu m)$	142	215	360	255	136	208

REFERENCES

Bally, J.; Snell, R. L.; Predmore, R. 1983, *Ap. J.*, **272**, 154.

Black, J. H. and van Dishoeck, E. F. 1987, *Ap. J.*, **322**, 412.

Cohen, M.; Bieging, J. H.; Schwartz, P. R. 1982, *Ap. J.*, **253**, 707.

Edwards, S.; Strom, S. E.; Snell, R. L.; Jarrett, T. H.; Beichman, C. A.; Strom, K. M. 1986, *Ap. J. Letts.*, **307**, L65.

Edwards, S.; Cabrit, S.; Strom, S. E.; Heyer, I.; Strom, K. M.; Anderson, E. 1987, *Ap. J.*, **321**, 473.

Ezer, D. and Cameron, A. G. W. 1967, *Can. J. Phys.*, **45**, 3429.

Falgarone, E. and Pérault, M. 1987 in *Protostars and Molecular Clouds*, ed. T. Montmerle and C. Bertout, Centre d'Etudes Nucléaires de Saclay, p.15.

Felli, M. and Panagia, N. 1981, *Astron. Ap.*, **102**, 424.

Felli, M.; Staude, H. J.; Reddmann, T.; Massi, M.; Eiroa, C.; Hefele, H.; Neckel, T.; Panagia, N. 1984, *Astron. Ap.*, **135**, 261.

Hartmann, L. 1986, *Fundamentals of Cosmic Phys.*, **11**, 279.

Heyer, M. H., Snell, R. L., Goldsmith, P. F., and Myers, P. C. 1987, *Ap. J.*, **321**, 370.

Lynden-Bell, D. and Pringle, J. E. 1974, *M.N.R.A.S.*, **168**, 303.

Margulis, M. and Lada, C. 1986, *Ap. J. Letts.*, **309**, 87.

Osterbrock, D. E. 1974, *Astrophysics of Gaseous Nebulae*, W. H. Freeman and Company, San Francisco, California.

Panagia, N. and Felli, M. 1975, *Astron. Ap.*, **39**, 1.

Persson, S. E.; McGregor, P. J.; Campbell, B. 1988, *submitted to Ap. J.*.

Scalo, J. M. and Pumphrey, W. A. 1982, *Ap. J.*, **258**, L29.

Schmid-Burgk, J. 1982, *Astron. Ap.*, **108**, 169.

Simon, M. and Cassar, L. 1984, *Ap. J.*, **283**, 179.

Simon, M.; Felli, N.; Cassar, L.; Fischer, J.; Massi, M. 1983, *Ap. J.*, **266**, 623.

Thompson, R. I.; Erickson, E. F.; Witteborn, F. C.; Strecker, D. W. 1976, *Ap. J.*, **210**, L31.

Thompson, R. I.; Strittmatter, P. A.; Erickson, E. F.; Witteborn, F. C.; Strecker, D. W. 1977, *Ap. J.*, **218**, 170.

Black, J. H. and van Dishoeck, E. F. 1987, *Ap. J.*, **322**, 412.

Wright, A. E. and Barlow, M. J. 1975, *M.N.R.A.S.*, **170**, 41.

FIGURE CAPTION

Figure V.1 The location of S87/IRS1, LkHα101, and S106 IR on the Hertzsprung-Russell diagram. Each source is represented by a cross. Evolutionary tracks of pre-main sequence stars of different masses are also plotted (Ezer and Cameron 1967). Each track starts at a time when the thermal energy just balances the gravitational potential energy for the indicated mass and the protostar is assumed to be contracting homologously. The dashed horizontal bar on each track indicates the time (in years) when the model ceases to be fully convective. The tracks end when the models reach the ZAMS, defined as the time when the luminosity reaches its final minimum value before the major hydrogen-burning phase starts. The time to evolve to the ZAMS (from the stated initial configurations) is indicated at the end of each track in years.

Figure V.1

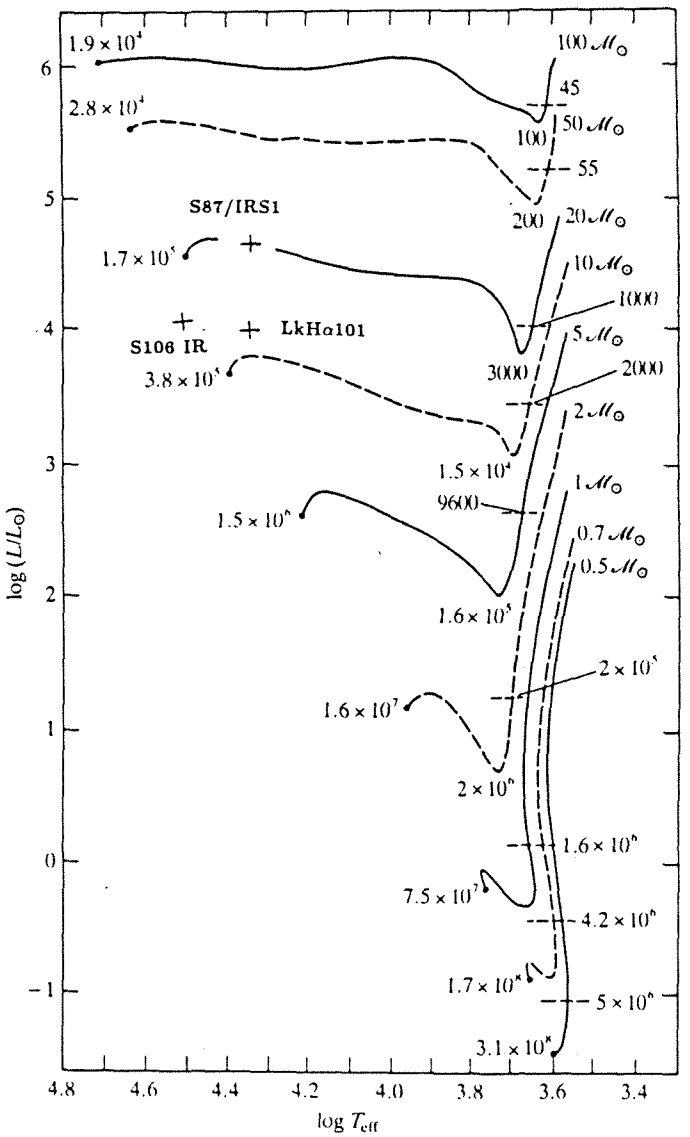
1.9 × 10⁴
2.8 × 10⁴
100 M⊙
45
100
50 M⊙
55
200
S87/IRS1
1.7 × 10⁵
20 M⊙
10 M⊙
1000
S106 IR
LkHα101
5 M⊙
3000
2000
3.8 × 10⁵
2 M⊙
1.5 × 10⁴
1 M⊙
9600
1.5 × 10⁵
0.7 M⊙
0.5 M⊙
1.6 × 10⁵
2 × 10⁵
1.6 × 10⁷
2 × 10⁶
1.6 × 10⁶
7.5 × 10⁵
4.2 × 10⁶
1.7 × 10⁴
5 × 10⁶
3.1 × 10⁴
6
5
4
3
2
1
0
−1
4.8
4.6
4.4
4.2
4.0
3.8
3.6
3.4
log (L/L⊙)
log T_eff